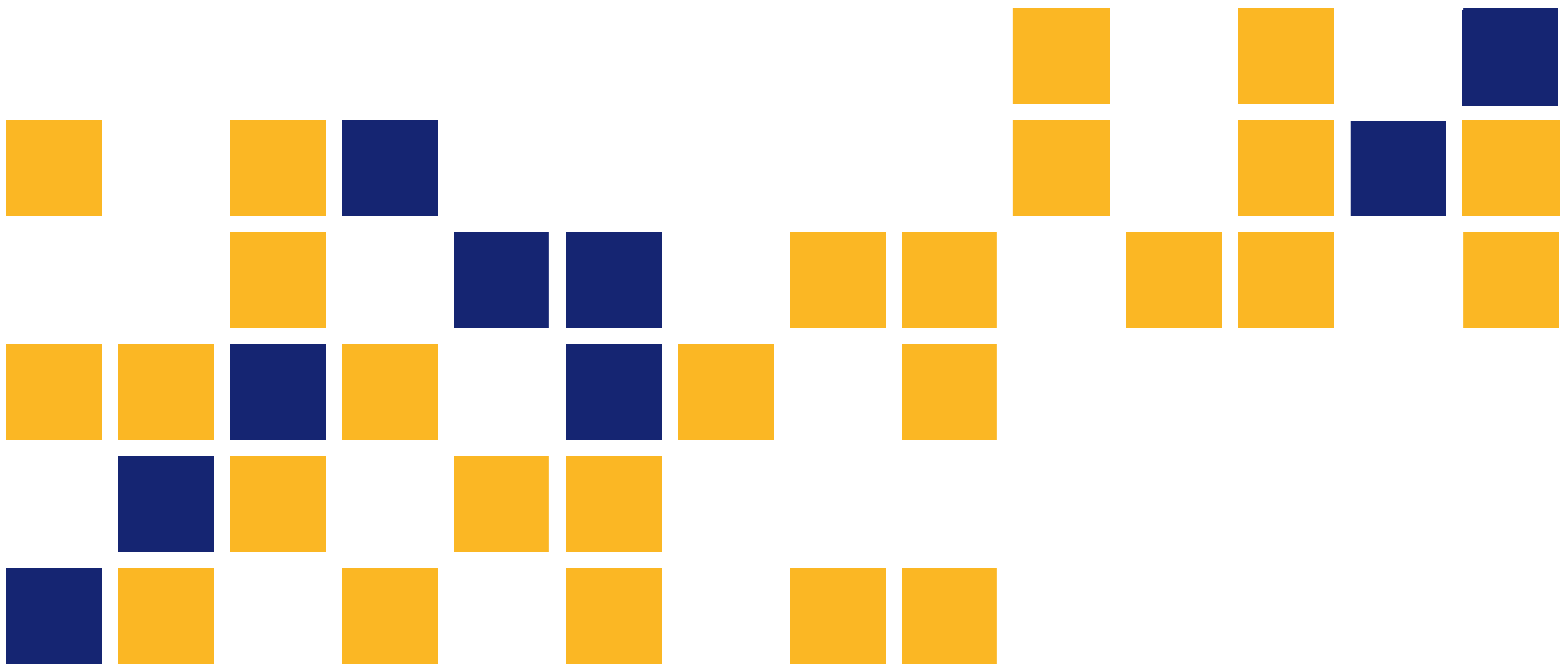


Accelerated Pavement Testing of Low-Volume Paved Roads with Geocell Reinforcement

Brandon Bortz
Mustaque Hossain, Ph.D., P.E.

Kansas State University Transportation Center

A Transportation Pooled Fund Study - TPF-5(048)



1 Report No. FHWA-KS-14-14	2 Government Accession No.	3 Recipient Catalog No.	
4 Title and Subtitle Accelerated Pavement Testing of Low-Volume Paved Roads with Geocell Reinforcement		5 Report Date March 2015	
		6 Performing Organization Code TPF-5(048)	
7 Author(s) Brandon Bortz, Mustaque Hossain, Ph.D., P.E.		7 Performing Organization Report No.	
9 Performing Organization Name and Address Kansas State University Transportation Center Department of Civil Engineering 2124 Fiedler Hall Manhattan, Kansas 66506		10 Work Unit No. (TRAIS)	
		11 Contract or Grant No. C1839	
12 Sponsoring Agency Name and Address Kansas Department of Transportation Bureau of Research 2300 SW Van Buren Topeka, Kansas 66611-1195		13 Type of Report and Period Covered Final Report October 2009–June 2014	
		14 Sponsoring Agency Code TPF-5(048) & RE-0508-01	
15 Supplementary Notes For more information write to address in block 9. Pooled Fund Study TPF-5(048) sponsored by the following DOTs: Kansas, Iowa, Missouri, and New York State.			
<p>The Midwest States Accelerated Pavement Testing Pooled-Fund Program, financed by the highway departments of Kansas, Iowa, Missouri, and New York, has supported an accelerated pavement testing (APT) project to study the rehabilitation of low-volume paved roads with geocells and different infill materials under real-world traffic on a marginal subgrade, and to simulate this type of rehabilitation numerically so that a design method can be developed. To achieve this study objective, four pavement test sections were constructed at the Civil Infrastructure System Laboratory of Kansas State University. Three out of these four lanes had geocell-reinforced bases with three different infill materials: crushed limestone, quarry by-products, and Recycled Asphalt Pavement. The fourth test lane was the control section consisting of crushed stone base. All sections were heavily instrumented. Repeated loads (80-kN single axle) were applied using an accelerated pavement testing machine. The sections with 50-mm hot-mix asphalt (HMA) layer reached the failure criteria of 12.5-mm rut depth after 10,000 passes due to excessive stress in the subgrade. The redesigned sections with 100-mm HMA layer carried 1.2 million passes without reaching 12.5-mm failure rut depth. The geocells with marginal materials as infills appear to be viable in low-volume paved road applications.</p>			
17 Key Words Geocell reinforcement, Accelerated pavement testing, Infill materials		18 Distribution Statement No restrictions. This document is available to the public through the National Technical Information Service www.ntis.gov .	
19 Security Classification (of this report) Unclassified	20 Security Classification (of this page) Unclassified	21 No. of pages 100	22 Price

Form DOT F 1700.7 (8-72)

This page intentionally left blank.

Accelerated Pavement Testing of Low-Volume Paved Roads with Geocell Reinforcement

Final Report

Prepared by

Brandon Bortz
Mustaque Hossain, Ph.D., P.E.

Kansas State University Transportation Center

A Report on Research Sponsored by

THE KANSAS DEPARTMENT OF TRANSPORTATION
TOPEKA, KANSAS

and

KANSAS STATE UNIVERSITY TRANSPORTATION CENTER
MANHATTAN, KANSAS

March 2015

© Copyright 2015, **Kansas Department of Transportation**

NOTICE

The authors and the state of Kansas do not endorse products or manufacturers. Trade and manufacturers names appear herein solely because they are considered essential to the object of this report.

This information is available in alternative accessible formats. To obtain an alternative format, contact the Office of Public Affairs, Kansas Department of Transportation, 700 SW Harrison, 2nd Floor – West Wing, Topeka, Kansas 66603-3745 or phone (785) 296-3585 (Voice) (TDD).

DISCLAIMER

The contents of this report reflect the views of the authors who are responsible for the facts and accuracy of the data presented herein. The contents do not necessarily reflect the views or the policies of the state of Kansas. This report does not constitute a standard, specification or regulation.

Abstract

The Midwest States Accelerated Pavement Testing Pooled-Fund Program, financed by the highway departments of Kansas, Iowa, Missouri, and New York, has supported an accelerated pavement testing (APT) project to study the rehabilitation of low-volume paved roads with geocells and different infill materials under real-world traffic on a marginal subgrade, and to simulate this type of rehabilitation numerically so that a design method can be developed. To achieve this study objective, four pavement test sections were constructed at the Civil Infrastructure System Laboratory of Kansas State University. Three out of these four lanes had geocell-reinforced bases with three different infill materials: crushed limestone, quarry by-products, and Recycled Asphalt Pavement. The fourth test lane was the control section consisting of crushed stone base. All sections were heavily instrumented. Repeated loads (80-kN single axle) were applied using an accelerated pavement testing machine. The sections with 50-mm hot-mix asphalt (HMA) layer reached the failure criteria of 12.5-mm rut depth after 10,000 passes due to excessive stress in the subgrade. The redesigned sections with 100-mm HMA layer carried 1.2 million passes without reaching 12.5-mm failure rut depth. The geocells with marginal materials as infills appear to be viable in low-volume paved road applications.

Acknowledgements

The research project was selected and monitored by members of the Midwest States Accelerated Pavement Testing Pooled-Fund Technical Committee. The committee includes Mr. Andy Gisi, Kansas Department of Transportation (KDOT), chair; Mr. John Donahue, Missouri Department of Transportation (MDOT); Mr. Mark Dunn, Iowa Department of Transportation (IADOT); and Julian Bendana, formerly with New York State DOT. Currently Mr. Greg Schieber is the chair. The authors acknowledge the cooperation and supervision of all committee members in this study. Contributions of Mr. Randy Testa and Mr. Luke McIntosh in various phases of this study are also gratefully acknowledged. The research team is also grateful to Sergeant Joe French, from the Motor Vehicle Inspection Division of the Kansas Highway Patrol, for his help in the measurement and calibration of the CISL axle load.

Table of Contents

Abstract.....	v
Acknowledgements.....	vi
Table of Contents.....	vii
List of Tables.....	ix
List of Figures.....	x
Chapter 1: Introduction.....	1
1.1 Introduction.....	1
1.2 Problem Statement.....	2
1.3 Research Objectives.....	3
1.4 Scope of the Research Program.....	3
1.5 Accelerated Pavement Testing (APT) at the Civil Infrastructure Systems Laboratory (CISL).....	4
1.6 Report Outline.....	6
Chapter 2: Material Characterization.....	9
2.1 Geocells and Geotextile.....	9
2.2 Subgrade.....	9
2.3 Base Material.....	9
2.3.1 AB-3.....	9
2.3.2 Quarry Waste.....	10
2.3.3 Reclaimed Asphalt Pavement (RAP).....	11
2.4 Hot-Mix Asphalt.....	12
2.4.1 Laboratory Testing.....	13
2.4.2 In-place Testing.....	25
Chapter 3: Description of the Experiment.....	29
3.1 CISL 16 Experiment.....	29
3.2 General Test Preparation.....	31
3.2.1 First (Thin) Experiment.....	36
3.2.2 Overlay Experiment.....	38
3.2.3 Second (Thick) Experiment.....	38

Chapter 4: Numerical Simulation of APT Tests	40
4.1 Introduction	40
4.2 Numerical Simulations	40
4.2.1 Material Properties	40
4.2.2 Boundary Conditions	44
4.2.3 Element/Mesh	44
4.2.4 Loading	47
Chapter 5: Results and Discussion	50
5.1 APT Test Results	50
5.1.1 First Experiment	50
5.1.2 Overlay Experiment	54
5.1.3 Second Experiment	57
5.1.4 Comparison of First and Second Experiment	63
5.2 Layered Elastic (KENLAYER) Analysis	65
5.3 Numerical Analysis Results	68
5.3.1 Numerical Response Analysis Comparison	68
5.3.2 Parametric Studies of Numerical Simulation	72
Chapter 6: Conclusions and Recommendations	76
References	77
Appendix: Numerical Analysis Profiles	80

List of Tables

Table 1.1: Number of Passes for Each Lateral Position of the APT Wheel	7
Table 2.1: Dynamic Modulus Test Results (6.89 MPa = 1 ksi).....	15
Table 2.2: Flow Time Test Results	23
Table 2.3: Flow Number Test Results	24
Table 2.4: Everseries Variables	27
Table 2.5: Backcalculated Moduli for First Experiment and Overlay Experiment	27
Table 2.6: Backcalculated Moduli for Second Experiment	28
Table 4.1: HMA Creep Test Results.....	41
Table 4.2: First Numerical Simulation Properties of Materials	42
Table 4.3: Second Numerical Simulation Properties of Materials	43
Table 4.4: Rut Simulation Steps	49
Table 5.1: Geocell Peak Horizontal Microstrain First Experiment (Positive = Tension).....	53
Table 5.2: Peak Horizontal Strain on Geocell after Overlay (Positive = Tension).....	57
Table 5.3: Geocell Peak Horizontal Strain Second Experiment (Positive = Tension)	60
Table 5.4: KENLAYER Vertical Pressure Results (6.89 kPa = 1 psi).....	67
Table 5.5: KENLAYER HMA Strain.....	67
Table 5.6: Numerical Response Analysis Results	69
Table 5.7: HMA Strain Comparison.....	69
Table 5.8: Subgrade Stress Comparison	70
Table 5.9: Rut Depths	71
Table 5.10: Rut Depth Comparison at One Million Cycles.....	72
Table 5.11: Parametric Study Material Properties	73

List of Figures

Figure 1.1: Geocell Materials	2
Figure 1.2: Single-Axle Bogie	5
Figure 1.3: Side View of the Single-Axle Bogie	5
Figure 1.4: Lateral Wander System	6
Figure 1.5: APT Machine with Temperature-Control Chamber.....	7
Figure 2.1: KDOT AB-3 Control Points and Grain Size Distribution of AB-3 Used in the Study	10
Figure 2.2: Grain Size Distribution of Quarry Waste (QW).....	11
Figure 2.3: Grain Size Distribution of Reclaimed Asphalt Pavement (RAP).....	12
Figure 2.4: HMA Gradation with KDOT SM-12.5A Control Points	13
Figure 2.5: KSU Asphalt Mixture Performance Tester (AMPT) Machine	14
Figure 2.6: Master Curve Plot at 23 °C (73 °F).....	17
Figure 2.7: Hamburg Wheel-Tracking Machine.....	18
Figure 2.8: Hamburg Samples under Testing	18
Figure 2.9: Hamburg Results	19
Figure 2.10: Tested Hamburg Samples.....	20
Figure 2.11: Hamburg Test Output with Test Parameters (After AASHTO T 324, 2004)	21
Figure 2.12: Creep Compliance versus Time (After Brown et al., 2009).....	22
Figure 2.13: Permanent Strain versus Number of Cycles (After Brown et al., 2009).....	24
Figure 2.14: Failed Specimen	25
Figure 2.15: KDOT Dynatest FWD.....	26
Figure 3.1: Wheel Wander Distribution.....	30
Figure 3.2: Instrumentation Layout	30
Figure 3.3: Pressure Cells Installed in Subgrade	32
Figure 3.4: Geocell Installation.....	32
Figure 3.5: Infill after Vibratory Plate Compaction.....	33
Figure 3.6: Roller Compaction of Infill	33
Figure 3.7: Lightweight Asphalt Paver.....	34
Figure 3.8: Asphalt Compactor.....	35

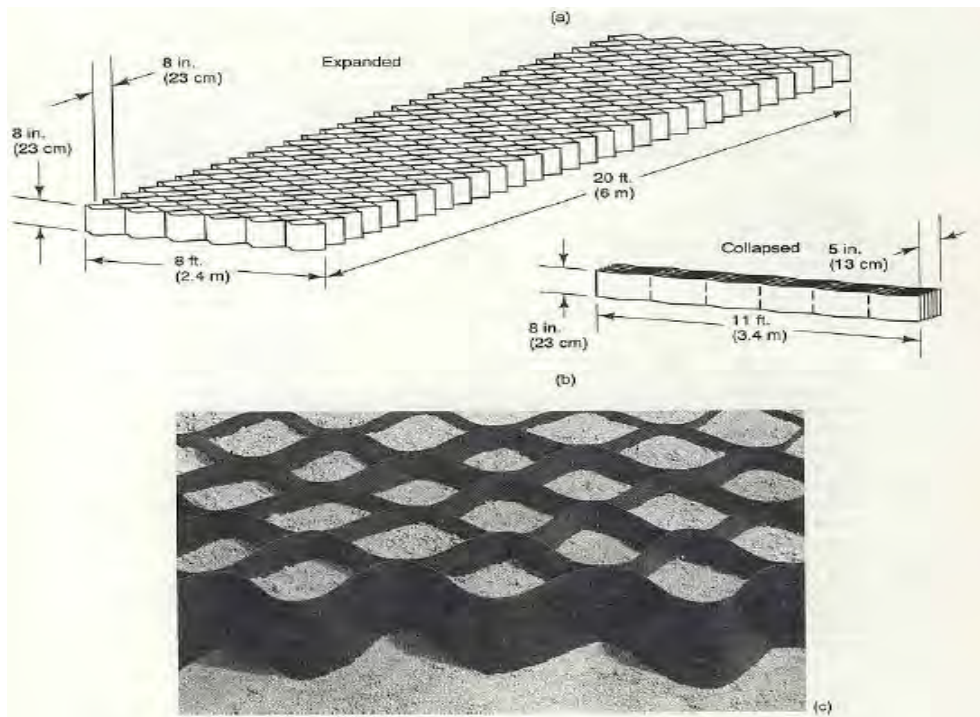
Figure 3.9: Transverse Profiler	35
Figure 3.10: Thin Cross Sections.....	37
Figure 3.11: QW Lane Failure First Experiment.....	37
Figure 3.12: Overlay Cross Sections	38
Figure 3.13: Thick Cross Sections.....	39
Figure 4.1: Simulated U-Shaped Rut Profile	41
Figure 4.2: Boundary Conditions for APT Models	44
Figure 4.3: HMA Mesh.....	45
Figure 4.4: Base Mesh	45
Figure 4.5: Subgrade Mesh.....	46
Figure 4.6: Geocell Mesh.....	46
Figure 4.7: Embedded Geocells in Base Layer.....	47
Figure 4.8: Loading of Model.....	48
Figure 4.9: Rut Simulation Loading	49
Figure 5.1: Typical Middle Pit Profile First Experiment.....	50
Figure 5.2: Typical South Pit Profiles First Experiment.....	51
Figure 5.3: Vertical Pressure on Subgrade of the Middle Pit during First Experiment.....	52
Figure 5.4: Vertical Pressure on Subgrade in South Pit for the First Experiment	53
Figure 5.5: Typical Profile of Middle Pit after Overlay	55
Figure 5.6: Typical Profile of South Pit after Overlay.....	55
Figure 5.7: Vertical Pressure on Subgrade of Middle Pit in Overlay Experiment	56
Figure 5.8: Vertical Pressure on Subgrade of South Pit in Overlay Experiment.....	56
Figure 5.9: Middle Pit Profiles in Second Experiment.....	58
Figure 5.10: South Pit Profiles Second Experiment	58
Figure 5.11: Vertical Pressure on Subgrade of Middle Pit in Second Experiment.....	59
Figure 5.12: Vertical Pressure on Subgrade of South Pit in Second Experiment.....	59
Figure 5.13: RAP Post Mortem of 2nd Test	61
Figure 5.14: AB-3 Post Mortem after 2nd Test	62
Figure 5.15: AB-3 Material after 2nd Test	62
Figure 5.16: Rut Depth Comparison for Middle Pit	63
Figure 5.17: Rut Depth Comparison for South Pit	64

Figure 5.18: Vertical Pressure on Subgrade Comparison.....	64
Figure 5.19: Geocell Strain Comparison	65
Figure 5.20: Geocell Path	68
Figure 5.21: Response Results for Varying Base Material Elastic Modulus.....	74
Figure 5.22: Subgrade Stress with Varying Geocell Height.....	74
Figure 5.23: Geocell Horizontal Strain with Varying Geocell Height	75
Figure A.1: Simulated Control Rut Profiles for First Test.....	80
Figure A.2: Simulated Control Rut Profiles for Overlay Test	81
Figure A.3: Simulated Control Rut Profiles for Second Test	81
Figure A.4: Simulated Quarry Waste Rut Profiles for First Test	82
Figure A.5: Simulated Quarry Waste Rut Profiles for Overlay Test.....	82
Figure A.6: Simulated Quarry Waste Rut Profiles for Second Test.....	83
Figure A.7: Simulated RAP Rut Profiles for First Test	83
Figure A.8: Simulated RAP Rut Profiles for Overlay Test	84
Figure A.9: Simulated RAP Rut Profiles for Second Test.....	84
Figure A.10: Simulated AB3 Rut Profiles for First Test	85
Figure A.11: Simulated AB3 Rut Profiles for Overlay Test.....	85
Figure A.12: Simulated AB3 Rut Profiles for Second Test.....	86

Chapter 1: Introduction

1.1 Introduction

Geosynthetics have been promoted over the last three decades to reinforce the geomaterials used for various civil engineering applications, including roadways. Geosynthetics are defined by the American Society for Testing and Materials (ASTM) as “a planar product manufactured from polymeric material used with soil, rock, earth, or other geotechnical engineering related material as an integral part of a man-made project, structure, or system” (ASTM D 4439-04, 2004). There are different types of geosynthetics with varying functions. These functions can be grouped as follows: separation, reinforcement, filtration, drainage, and containment (Koerner, 2005). Transportation engineers have been working on geosynthetics in pavement structures since the early 1980s. A combination of geotextile and geo-grid reinforcements have shown to increase bearing capacity when placed over a weak subgrade, and can increase the load distribution capacity by confining the soil particles. Geocellular confinement systems (geocells) are a type of geosynthetics that have seen an increasing interest in reinforcement for base courses of pavement structures. The original type of geocell is made from high-density polyethylene (HDPE) strips 200 mm (8 inches) wide and approximately 1.2 mm (50 mils) thick (Koerner, 1994). They are ultrasonically welded along their 200-mm (8-inch) width at approximately 33-cm (13-inch) intervals and are shipped to the job site in a collapsed configuration as shown in Figure 1.1. At the job site they are placed directly on the subsoil’s surface and propped open in an accordion fashion with an external stretcher assembly. This particular section expands into a 2.4 meter x 6.1 meter (8 ft x 20 ft) series of 561 cells, each approximately 200 mm (8 inches) in diameter. They are then filled with an infill material and compacted using a hand-operated, vibratory plate compactor (Koerner, 1994).



Source: Koerner, 1994

Figure 1.1: Geocell Materials

1.2 Problem Statement

Currently, geocells have more widespread use for confinement applications due to their 3-Dimensional (3-D) structure than any other planar geosynthetic reinforcement (Yuu, Han, Rosen, Parsons, & Leshchinsky, 2008). However, most studies have been done to demonstrate the use of geocells for increasing bearing capacity and reducing settlement of soft soil foundations (Dash, Krishnaswamy, & Rajagopal, 2001; Dash, Rajagopal, & Krishnaswamy, 2001; Dash, Rajagopal, & Krishnaswamy, 2004; Dash, Sireesh, & Sitharam, 2003; Sitharam, Sireesh, & Dash, 2005). Bathurst and Jarrett (1988) showed that geocell-reinforced bases had a higher load capacity over soft peat subgrades. Geocells can stiffen the base layer, reducing normal stresses while reorienting the shear stresses on the subgrade that limit the lateral movement of base material and subgrade soil (Giroud & Han, 2004a).

Even though these studies have demonstrated that geocells can provide outstanding soil confinement and perhaps enhance the performance of base courses on weak subgrade, the use of geocells in unpaved and paved roads is still limited due to the lack of accepted design methods and research (Yuu et al., 2008). Giroud and Han (2004a, 2004b) developed a theoretical equation

for the thickness of the base layer incorporating planar geogrid-reinforced unpaved roads. Pokharel, Han, Leshchinsky, Parsons, and Halahmi (2010) adjusted the Giroud and Han equation to design unpaved roads with a geocell-reinforced base layer.

The advantages of geocells include reduction of base and hot-mix asphalt (HMA) layer thicknesses needed over a marginal or weak subgrade. Lower quality infill materials, such as reclaimed asphalt pavement (RAP) and quarry waste (QW), can be used in the geocells because of the confining nature of these geocells. Thus, geocells have the possibility to be an economical option in rehabilitation of pavements including those on low-volume roads.

1.3 Research Objectives

The objectives of this study are:

- To test a geocell design with different infill materials and a thin HMA layer under simulated full-scale traffic on a marginal subgrade, using accelerated pavement testing (APT).
- To develop a finite element model for the geocell-reinforced paved roads considering the quality of the infill material to study the design of such pavements.

1.4 Scope of the Research Program

The study consisted of building eight test sections in two pits located at the Kansas State University Civil Infrastructure System Laboratory (CISL). There were two experiments of four test sections each. Each experiment consisted of three sections with three different infill materials, quarry waste, crushed limestone (AB-3), and reclaimed asphalt pavement (RAP), in the geocellular reinforcement, and one unreinforced control section with an AB-3 base layer. The APT machine was used to apply repeated dynamic wheel loading to the test sections. The original design had thin cross sections and failed rapidly. Therefore, thicker sections were designed, constructed, and tested.

A 3-D finite element (FE) model was constructed using the commercial FE software Abaqus. The developed model was calibrated with the results found from the CISL tests and used to study the design of such pavements.

1.5 Accelerated Pavement Testing (APT) at the Civil Infrastructure Systems Laboratory (CISL)

The Accelerated Pavement Testing (APT) facility at the Civil Infrastructure Systems Laboratory (CISL) at Kansas State University is an indoor facility with about 651 m² (7,000 ft²) of floor space. It is owned and operated by Kansas State University (KSU). The laboratory allows full-scale accelerated pavement testing on pavement structures. The test pavements are constructed in three 1.83-m (6-ft) deep test pits of varying width and 6.1 m (20 ft) in length.

The accelerated loading is provided by the APT machine that can be moved on rails between the testing pits. The main components of the machine are the steel frame, which has two main girders with a 12.8-m (42-ft) center-to-center span; and the bogie, which is supported by the frame (Figures 1.2 and 1.3). The bogie is pulled back and forth by a rubber belt attached to an electric motor fixed on the frame. The wheel-load assembly consists of a single or tandem axle mounted on the bogie. Loading of the axle assembly is accomplished with a hydraulic pump mounted on the bogie, above the axle, and connected to two hydraulic cylinders mounted on top of a single axle. The hydraulic pump pressurizes the oil in the hydraulic circuit and, thus, the two cylinders push the bogie into the steel frame and the axle on the top of the test pavement. The hydraulic pump is also used to raise the bogie when uni-directional loading is applied. The axle load is controlled by the pressure in the hydraulic circuit. Load cells mounted on each wheel are used to measure the instantaneous wheel loads.

The bogie moves with a constant speed of 11 km/h (7 mph) above the test pavement; acceleration and deceleration are done outside the test area. The bogie takes approximately 5.8 seconds to complete its travel distance in one direction. In bi-directional loading mode, approximately 650 passes of the bogie are applied in one hour of operation, and about 100,000 passes in one week. The operation is typically stopped for several hours weekly for maintenance of the machine and measurement of pavement response and performance. Typically, two test pavements are constructed in each pit and loaded simultaneously with one wheel of the axle passing above each test pavement.



Figure 1.2: Single-Axle Bogie



Figure 1.3: Side View of the Single-Axle Bogie

The machine is equipped with a lateral wandering device that moves the entire frame in a lateral direction, with a maximum lateral wander of ± 610 mm (± 24 inch). The lateral movement is applied in steps of 12.5 mm (0.5 inch) using a screw jack (Figure 1.4). Table 1.1 gives the number of wheel-load passes at each lateral position.

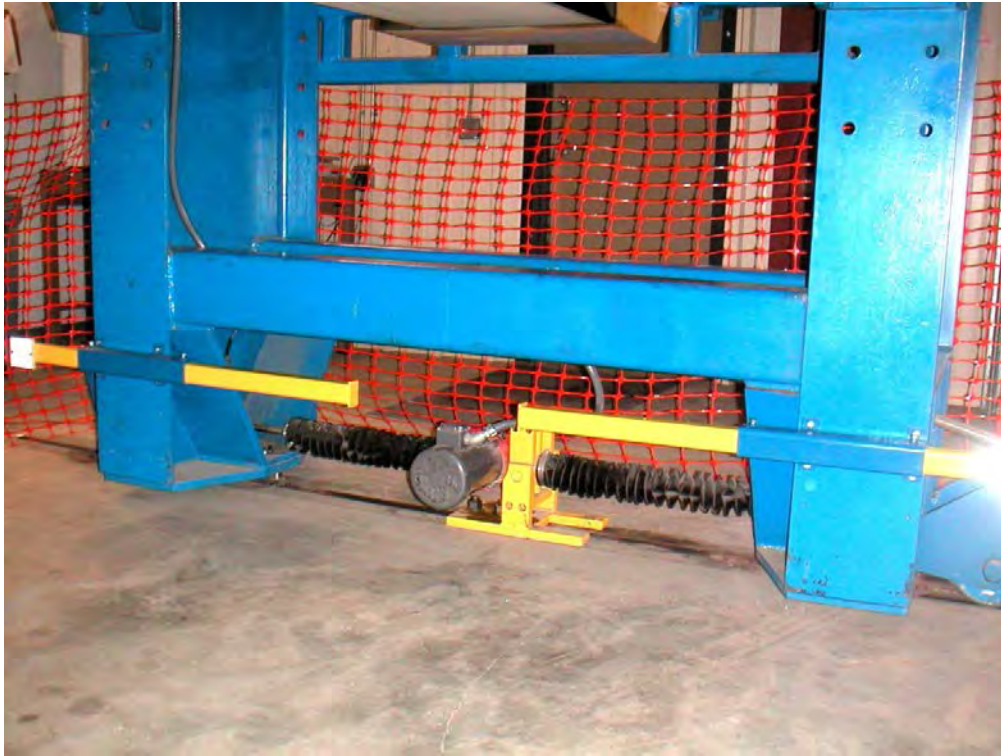


Figure 1.4: Lateral Wander System

A temperature-control chamber was built to encase the entire steel frame such that the temperature in the asphalt concrete layers could be controlled within ± 3 °C (± 6 °F). For the CISL 14 project, target testing temperatures were 20 °C (68 °F) and 35 °C (95 °F). Figure 1.5 shows the temperature-control chamber as used in the entire experiment.

1.6 Report Outline

This report is divided into five chapters. Chapter 1 covers the research background, problem statement, study objectives, study scope, and dissertation outline. Chapter 2 describes material characteristics used in this study. Chapter 3 describes the APT testing of this study.

Chapter 4 describes the numerical simulation of the APT testing. Chapter 5 compares the results of the APT testing and numerical simulation. Chapter 6 presents conclusions and recommendations based on this study.

Table 1.1: Number of Passes for Each Lateral Position of the APT Wheel

Lateral position (in.)	Number of wheel passes	Lateral position (in.)	Number of wheel passes
-6	10	0	38
-5.5	12	0.5	38
-5	15	1	37
-4.5	18	1.5	35
-4	21	2	33
-3.5	24	2.5	30
-3	27	3	27
-2.5	30	3.5	24
-2	33	4	21
-1.5	35	4.5	18
-1	37	5	15
-0.5	38	4.5	12
0	38	6	10
Maximum Distance = 6 in. P = 90% N=640 St. Dev. =3.65"			



Figure 1.5: APT Machine with Temperature-Control Chamber

Chapter 2: Material Characterization

2.1 Geocells and Geotextile

The geocells used in this study are NEOLOY™ polymeric alloy (NPA) geocells, a nano-composite alloy of polyester/polyamide nano fibers, dispersed in polyethylene matrix. The polymeric alloy has a similar flexibility at low temperatures as high density polyethylene (HDPE), along with an elastic behavior similar to engineering thermoplastics. The NPA geocell has a wall thickness of 1.1 mm. Han et al. (2011) calculated that the NPA geocell materials have a tensile strength of 19.1 megapascals (MPa), or 2.77 kilopounds per square inch (ksi), and secant elastic modulus of 355 MPa (51.5 ksi) at 2% strain. A 100 g (3.5 oz) non-woven geotextile was used as a separator between the subgrade and the base in the geocell-reinforced sections.

2.2 Subgrade

An American Association of State Highway and Transportation Officials (AASHTO) A-7-6 clay was used in subgrade construction. The optimum moisture content was found to be 21% with a maximum dry density of 1.61 g/cm³, or 100.5 pounds per cubic foot (pcf; Han et al., 2011). Yang (2010) conducted tests on the subgrade material and calculated the Young's modulus to be 10.3 MPa (1,493 pounds per square inch [psi]) and unconfined compressive strength to be 104.6 kilopascals (kPa, or 15.2 psi).

Plastic Limit (PL), Liquid Limit (LL), and percent finer than 75 µm sieve tests were found to be 22%, 43%, and 97.7%, respectively. The Plasticity Index was 21. In the first test, an approximate California Bearing Ratio (CBR) of 6% was achieved in the pits at a moisture content of 21%. In the second test, a CBR of 12% was used at a moisture content of 18%.

2.3 Base Material

2.3.1 AB-3

Crushed limestone, AB-3, was used in the control section with no geocells, as well as in a test lane with geocell reinforcement. AB-3 is a well-graded base material that is used in a variety of road applications by the Kansas Department of Transportation (KDOT). KDOT particle size

distribution specifications and particle size distribution of the AB-3 are shown in Figure 2.1. A mean particle size (d_{50}) of 4.4 mm (0.17 inches.), a coefficient of curvature of 7.4, and a coefficient of uniformity of 86 was found.

The optimum moisture content of 10.2% would result in a CBR of 45% (Pokharel et al., 2010). The maximum dry density was determined to be 2.13 g/cm³ (133.0 pcf). In the first test, the AB-3 layer was compacted at a moisture content of 9.17% in the control lane and 9.01% in the geocell lane. In the second test, the AB-3 layer was compacted at a moisture content of 6.7% in the control lane and at 6.3% in the geocell-reinforced lane.

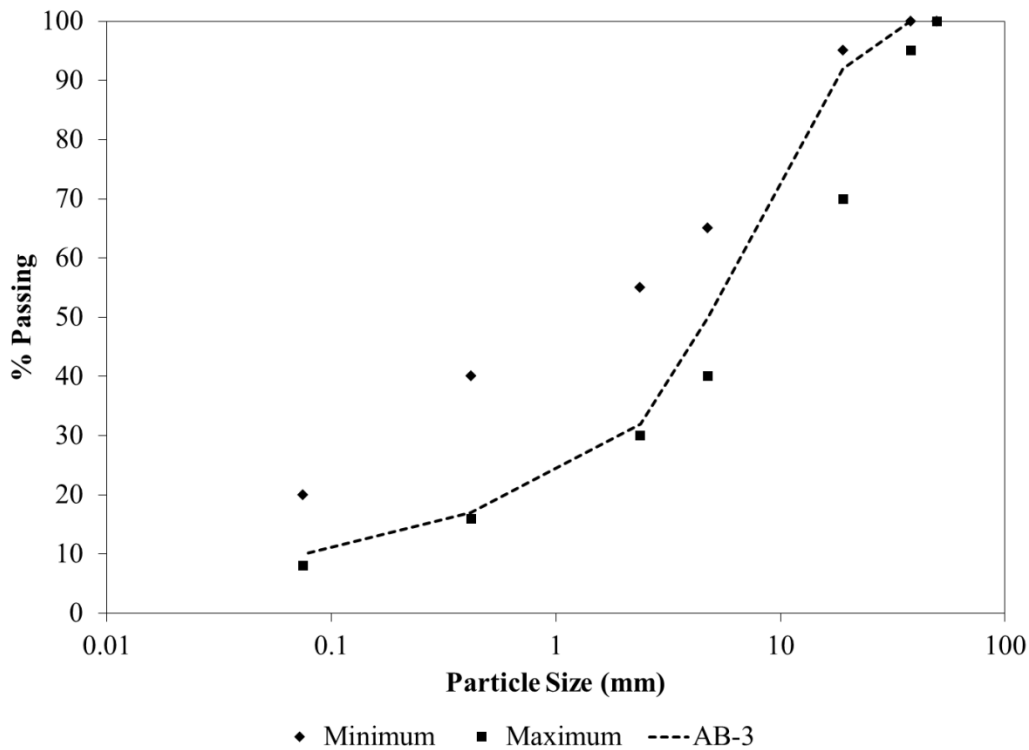


Figure 2.1: KDOT AB-3 Control Points and Grain Size Distribution of AB-3 Used in the Study

2.3.2 Quarry Waste

Eighteen to twenty million tonnes (20 to 22 million tons) of crushed rock are produced annually in Kansas. It is estimated that about 35% to 40% of the crushed rock is reduced to fines commonly called quarry waste (QW). Some of this QW is used in hot-mix asphalt production or

in agricultural applications. That leaves approximately 10% to 20% of QW stockpiled or land filled annually in Kansas (F. Rockers & W. Moses, personal communication, 2011). The QW in this study was obtained from a local quarry in Kansas. After a sieve analysis, as illustrated in Figure 2.2, the mean particle size (d_{50}) of 1.3 mm, a coefficient of curvature of 2.3, and a coefficient of uniformity of 24 was found. Pokharel et al. (2010) found optimum moisture content to be 11%, and a maximum dry density of 2.06 g/cm^3 . The optimum moisture content resulted in a CBR of 19%. In the first and second tests, the QW was compacted at moisture contents of 10.6% and 6.8%, respectively.

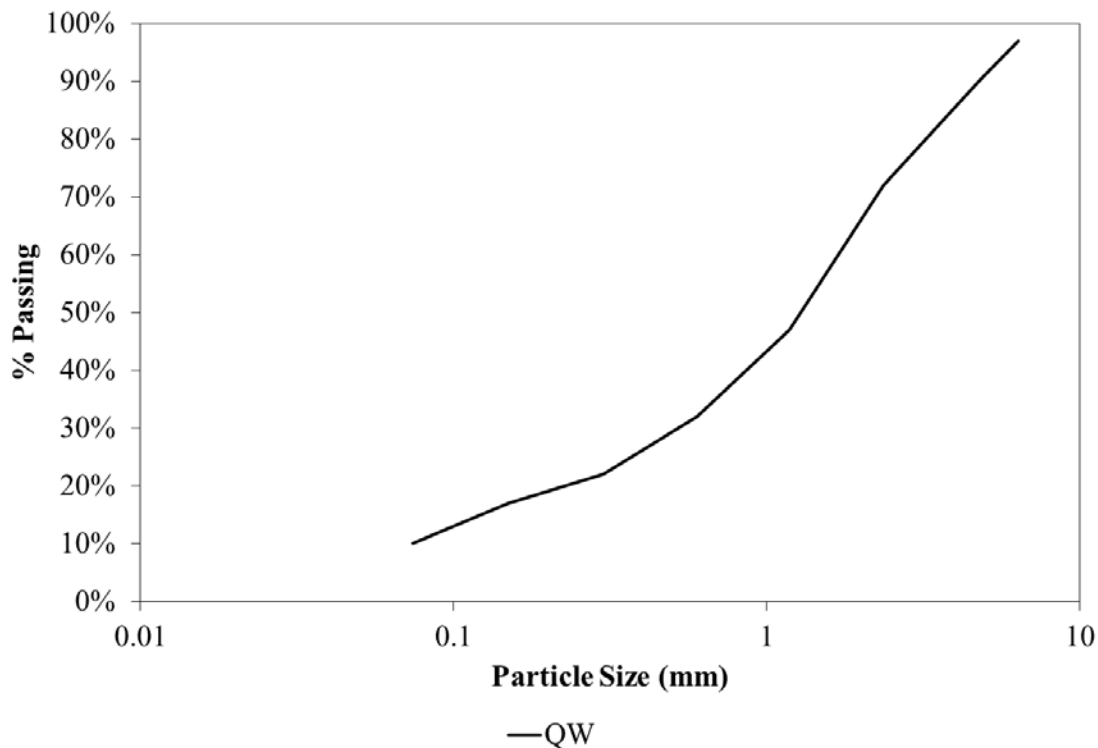


Figure 2.2: Grain Size Distribution of Quarry Waste (QW)

2.3.3 Reclaimed Asphalt Pavement (RAP)

Nationwide, approximately 91 million tonnes (100 million tons) of reclaimed asphalt pavement (RAP) are produced each year. Approximately, 73 million tonnes (80 million tons) are reused in various aspects of pavement construction (MAPA, 2012). The RAP in this study was collected from a local HMA plant. Han et al. (2011) found that RAP had an optimum moisture

content of 6%, maximum dry density of 1.81 g/cm³ (113.0 pcf), a CBR value of 10% at 5% moisture content, and 8% at the optimum moisture content.

The RAP grain size distribution is shown in Figure 2.3. The binder content of the RAP was determined by the ignition oven method to be 6.5%. In the first and second test, the RAP was compacted at moisture contents of 6.4% and 10.4%, respectively. Water was added to the RAP in the second test to help compact the RAP into the NPA geocells.

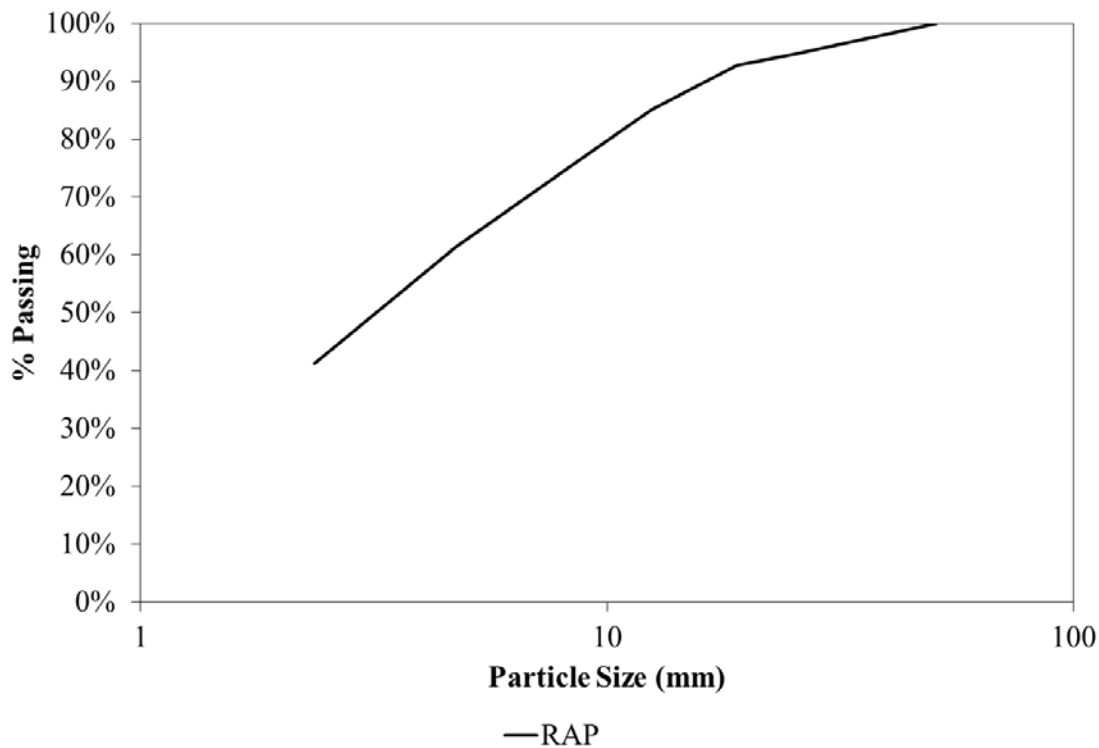


Figure 2.3: Grain Size Distribution of Reclaimed Asphalt Pavement (RAP)

2.4 Hot-Mix Asphalt

A Superpave mixture, or hot-mix asphalt (HMA) with 12.5-mm Nominal Maximum Aggregate Size and fine gradation, known as SM-12.5A at KDOT, was used. The aggregate blend consisted of 26% 19-mm (0.75-inch) rock, 17% 9.5-mm (0.375-inch) chips, 20% manufactured sand, and 17% concrete sand with a final gradation shown in Figure 2.4. A PG 70-28 binder was used. The total air void content at N_{design} was 4.04%. The HMA properties were found using both laboratory and in-place testing.

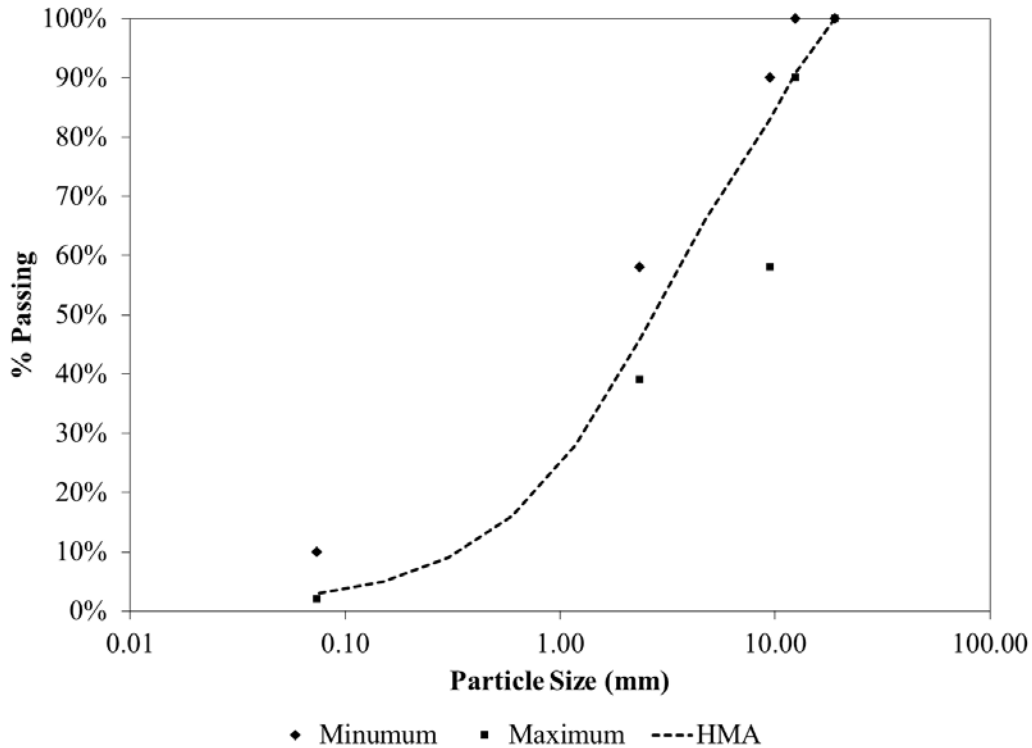


Figure 2.4: HMA Gradation with KDOT SM-12.5A Control Points

2.4.1 Laboratory Testing

2.4.1.1 Dynamic Modulus

“The complex modulus (E^*) is defined as a complex number that relates the stress to strain for a linear viscoelastic material subjected to sinusoidal loading” (Brown et al., 2009). The dynamic modulus is the absolute value of the complex modulus. For this study, the dynamic modulus test was performed following AASHTO TP 79 (2011) at 4 °C, 21 °C, and 37 °C (40 °F, 70 °F, and 100 °F). A sinusoidal vertical load was applied to 100-mm (4-inch) diameter and 150-mm (6-inch) tall HMA cylinders. During the test, the applied stresses and resulting strains are recorded as a function of time and then used to calculate the dynamic modulus and phase angle. The test was conducted in the Asphalt Mixture Performance Tester (AMPT) as seen in Figure 2.5. Four samples were used during dynamic modulus testing. The results can be seen Table 2.1.



Figure 2.5: KSU Asphalt Mixture Performance Tester (AMPT) Machine

A dynamic modulus master curve was plotted at 23 °C (73 °F) as a reference temperature, the temperature at which APT was conducted. Plotting the master curve was done using Mastersolver Version 2.3, released by Advance Asphalt Technologies, LLC. Three replicas were used to calculate the master curve. The sigmoid function equation solved during plotting of the master curve is shown in Equation 2.1. The master curve for the HMA is shown in Figure 2.6.

$$\log|E^*| = \log(\text{Min}) + \frac{(\log(\text{Max}) - \log(\text{Min}))}{1 + e^{\beta + \gamma(\log\omega + \frac{\Delta E_a}{19.14714}[\frac{1}{T} - \frac{1}{T_r}])}} \quad \text{Equation 2.1}$$

Where

$|E^*|$ = dynamic modulus

Min = limiting minimum modulus, ksi

Max = limiting maximum modulus, ksi

ω_r = reduced frequency at the reference temperature

ω = loading frequency at the test temperature, Hz

T_r = reference temperature, °K

T = test temperature, °K

ΔE_a = activation energy (treated as a fitting parameter)

B and γ = fitting parameters

Table 2.1: Dynamic Modulus Test Results (6.89 MPa = 1 ksi)

a. 4 °C (40 °F)

	Sample ID	4 °C (40 °F)					
		25 Hz	10 Hz	5 Hz	1 Hz	0.5 Hz	0.1 Hz
Dynamic Modulus (MPa)	1	15634	14276	13435	11488	10655	8791
	2	17636	18615	17592	15635	14512	12180
	3	16953	16191	15352	13647	12676	10524
	4	17962	16320	15798	13622	12610	10364
	Average	17046.25	16350.5	15544.25	13598	12613.25	10464.75
	SD	1031.1	1775.5	1707.1	1693.5	1575.2	1385.3
	CV (%)	6.05	10.86	10.98	12.45	12.49	13.24
Phase Angle (Degrees)	1	7.44	8.47	9.15	10.89	11.72	13.95
	2	3.73	6.57	7.65	8.98	9.79	11.64
	3	7.13	9.92	8.58	9.73	10.51	12.61
	4	7.36	9.88	8.88	10.36	11.19	13.59
	Average	6.4	8.7	8.5	9.9	10.8	12.9
	SD	1.794	1.577	0.652	0.823	0.837	1.039
	CV (%)	27.98	18.1	7.6	8.2	7.75	8.03

b. 21 °C (70 °F)

	Sample ID	21 °C (70 °F)					
		25 Hz	10 Hz	5 Hz	1 Hz	0.5 Hz	0.1 Hz
Dynamic Modulus (MPa)	1	10005	9160	8300	6333	5599	3948
	2	15179	11958	10830	8426	7383	5348
	3	12608	11822	9801	7588	6695	4752
	4	10735	9356	8322	6133	5327	3633
	Average	12131.7	10574	9313.2	7120	6251	4420.25
	SD	2308.4	1522.7	1231.2	1082.9	958.72	777.5
	CV (%)	19.03	14.40	13.22	15.21	15.34	17.59
Phase Angle (Degrees)	1	16.33	14.05	15.03	17.95	19.28	22.85
	2	21.04	12.82	13.53	16.18	17.45	20.75
	3	5.08	11.53	14.01	16.67	17.97	21.52
	4	15.36	15.81	16.92	20.29	21.64	25.29
	Average	14.4525	13.5525	14.8725	17.7725	19.085	22.6025
	SD	6.722	1.823	1.501	1.836	1.869	1.990
	CV (%)	46.5	13.45	10.10	10.3	9.79	8.81

c. 37 °C (100 °F)

	Sample ID	37 °C (100 °F)					
		25 Hz	10 Hz	5 Hz	1 Hz	0.5 Hz	0.1 Hz
Dynamic Modulus (MPa)	1	4480	3566	2983	1840	1503	859
	2	5159	4162	3512	2253	1870	1128
	3	4429	3513	2929	1815	1480	860.9
	4	4341	3393	2789	1651	1317	728.5
	Average	4602.25	3658.5	3053.25	1889.75	1542.5	894.1
	SD	375.58	343.37	316.57	256.26	233.50	167.79
	CV (%)	8.16	9.39	10.37	13.56	15.14	18.77
Phase Angle (Degrees)	1	24.19	26.08	27.16	29.77	29.99	30.87
	2	23.36	24.82	25.85	28.45	28.73	29.81
	3	24.37	26.11	27.09	29.36	29.42	29.9
	4	25.94	27.81	28.79	31.1	31.08	31.33
	Average	24.465	26.205	27.2225	29.67	29.805	30.4775
	SD	1.077	1.227	1.2058	1.101	0.993	0.743
	CV (%)	4.40	4.68	4.43	3.71	3.33	2.44

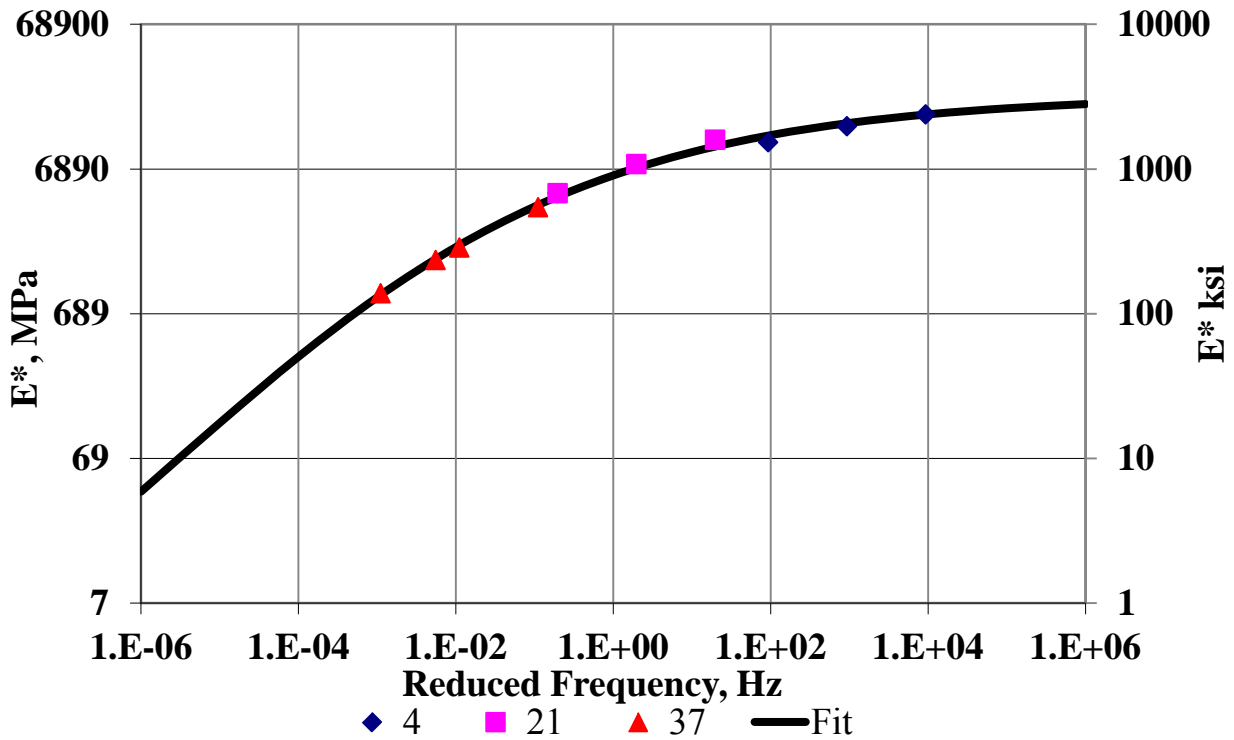


Figure 2.6: Master Curve Plot at 23 °C (73 °F)

Vehicles traveling across HMA pavement will induce loading with a corresponding frequency. HMA will have a dynamic modulus corresponding to the temperature and frequency. Recommendations are given for the frequency in the Mechanistic-Empirical Pavement Design Guide (MEPDG). The approximation ratio of the speed (mph) to frequency (Hz) is about 2:1 (NCHRP, 2011). APT testing was conducted at 11.3 km/hr (7 mph); therefore, this speed will induce a loading with a frequency of 3.5 Hz. From Figure 2.6, the corresponding dynamic modulus at 3.5 Hz is approximately 7,500 MPa (1,090 ksi).

2.4.1.2 Hamburg Wheel Tracking Machine Test

Rutting and moisture-susceptibility of HMA were tested in accordance with AASHTO T 324. Hamburg wheel tracking tests are used to “determine the premature failure susceptibility of HMA due to weakness in the aggregate structure, inadequate binder stiffness, or moisture damage” (AASHTO T 324, 2004). The test is completed by rolling loaded wheels across HMA

specimens immersed in a temperature-controlled water bath. Figure 2.7 shows the Hamburg wheel-tracking machine, and Figure 2.8 shows the samples being tested.



Figure 2.7: Hamburg Wheel-Tracking Machine

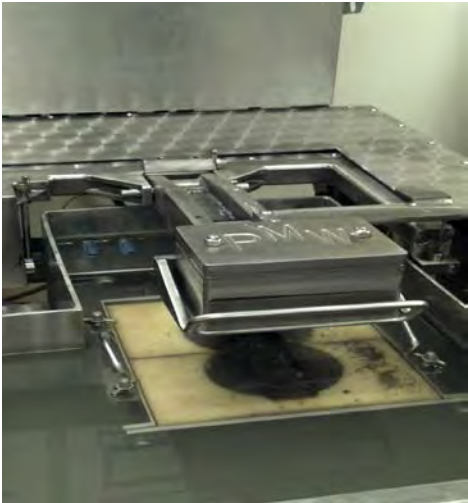


Figure 2.8: Hamburg Samples under Testing

The rut depths measured during testing can be graphically represented as shown in Figure 2.9. AASHTO T 324 is usually run until 20,000 passes with a failure depth set by an agency. The Texas Department of Transportation (TxDOT) sets a failure depth of 12.5 mm (0.5 inches; Button, Chowdhury, & Bhasin, 2004). However, for this study, 40,000 passes were completed without reaching the study failure depth of 12.5 mm. Figure 2.10 shows the tested specimens.

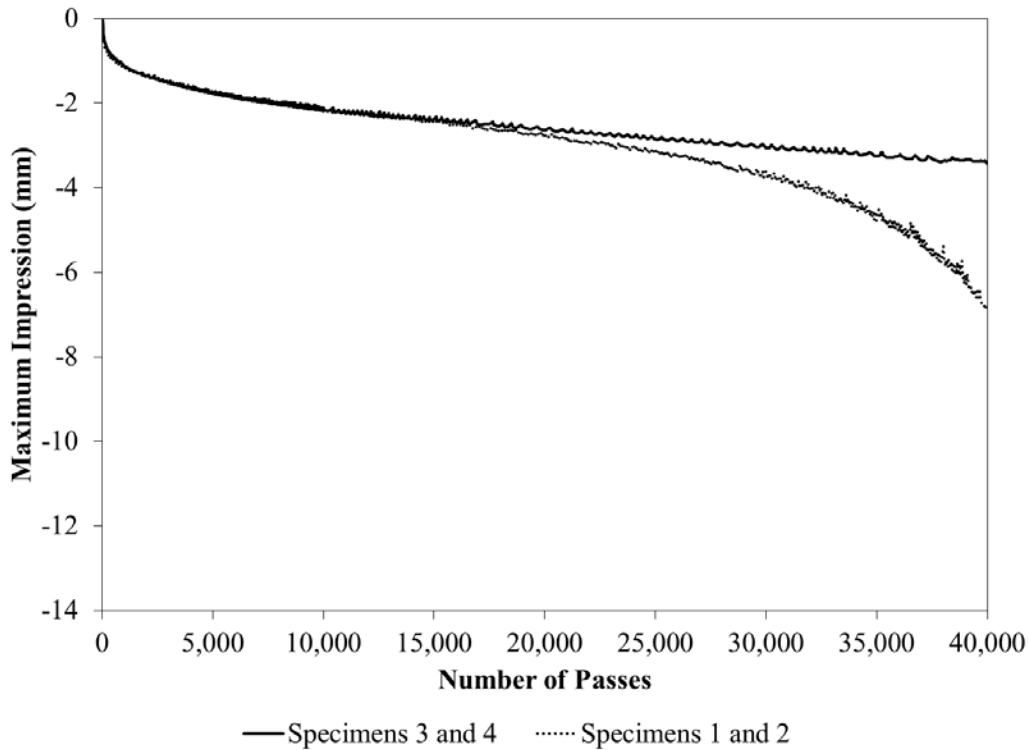


Figure 2.9: Hamburg Results

From the Hamburg wheel tracking test results, the creep slope, which is the inverse of the rate of deformation in the linear region of the deformation curve after post compaction, is obtained. Rutting from the plastic flow is related to the creep slope. At the Stripping Inflection Point (SIP), the stripping slope begins. Stripping slope is the inverse of the rate of deformation in the linear region of the deformation curve after the SIP (Aschenbrener, Terrel, & Zamora, 1994; Brown et al., 2009). These slopes can be seen on typical Hamburg test in Figure 2.11. By comparing Figure 2.9 and Figure 2.11, the HMA used in this study reached 20,000 passes

without reaching the SIP, which indicates a high quality HMA as far as rutting performance goes.



Figure 2.10: Tested Hamburg Samples

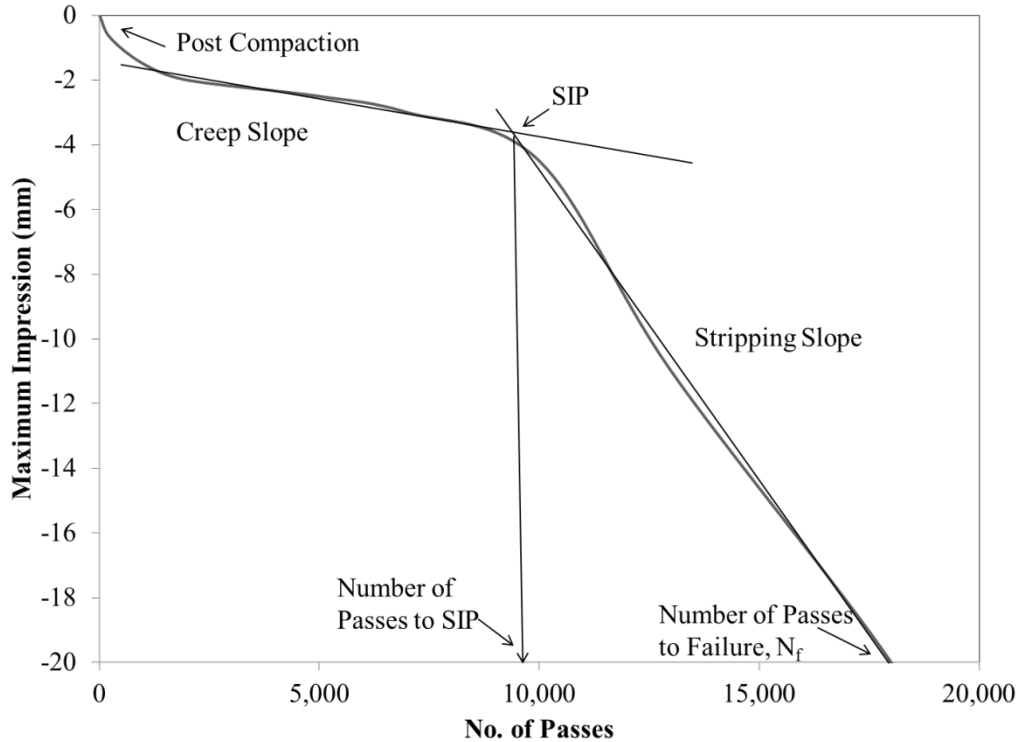


Figure 2.11: Hamburg Test Output with Test Parameters (After AASHTO T 324, 2004)

2.4.1.3 Flow Time Test

The flow time test is a static creep test which gives flow time or “the length of time the pavement can withstand steady pressure until flow occurs, causing permanent deformation” (Brown et al., 2009). NCHRP 465 Appendix C (Witczak, Kaloush, Pellinen, El-Basyouny, & Von Quintus, 2002) outlines the test procedure. The test can be conducted using a confining stress or without a confining stress. A specimen is loaded with a target deviator stress and the load is held until the total strain reaches 5%. Three stages of creep, primary, secondary, and tertiary, are obtained in this test. A nonlinear relationship between strain and time exist in the primary and tertiary stages. Secondary creep has a constant strain rate with loading. Flow time is the point where tertiary creep begins. Figure 2.12 shows the three stages of creep.

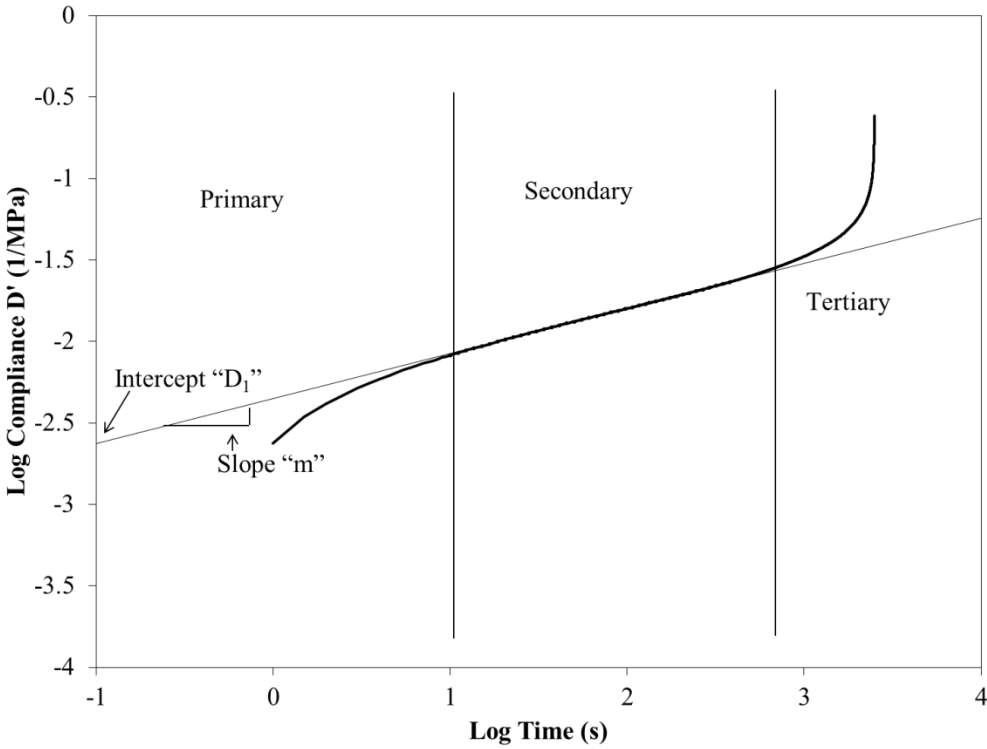


Figure 2.12: Creep Compliance versus Time (After Brown et al., 2009)

The secondary creep is linear and creep information can be obtained from this region. Axial creep compliance at any time is determined by Equation 2.2. A power law model is used to the secondary stage of creep compliance, shown in Equation 2.3 (Brown et al., 2009).

$$D(t) = \frac{\varepsilon(t)}{\sigma_0} \quad \text{Equation 2.2}$$

Where

$D(t)$ = creep compliance

$\varepsilon(t)$ = strain response

σ_0 = applied stress

$$D(t) = D_0 + D_1 t^m \quad \text{Equation 2.3}$$

Where

D_0 = instantaneous compliance

t = time

D_1 = time-dependent creep compliance at a time of one second

m = the slope of the creep compliance-time relationship in log-log scale

The flow time was conducted at 57 °C (135 °F) with no confining stress and deviator stress of 207 kPa (30 psi). Two specimens were tested and the results can be seen in Table 2.2.

Table 2.2: Flow Time Test Results

Sample ID	D₁	m	D₀	Flow Time
1	0.00445	0.2766	0.00627	603.5
2	0.00417	0.256	0.00571	1284
Average	0.00431	0.2663	0.00599	943.75

2.4.1.4 Flow Number Test

The flow number test gives the number of load cycles a pavement can tolerate before it flows. Appendix B in NCHRP 465 (Witczak et al., 2002) outlines the specifications of the test. Overall, the flow number tests and flow time tests are similar tests. However, the flow number uses haversine loading of 0.1 seconds of loading and 0.9 seconds of rest. The cyclic loading simulates a heavy vehicle driving repeatedly over a pavement structure (Brown et al., 2009). Again, the three stages of creep can be seen during testing, and data collected during the test is used to calculate dynamic creep parameters, intercept (a), slope (b), and flow number (F_n), as seen in Figure 2.13. F_n is defined as the cycle that tertiary flow begins. A power law can be used to model the relationship between the permanent strain and the number of loading cycles in the secondary zone, shown in Equation 2.4.

$$\varepsilon_p = aN^b \quad \text{Equation 2.4}$$

Confining stress is again optional in this test and was not used in this study. A deviator stress of 207 kPa (30 psi) at 57 °C (135 °F) was used. Results for the HMA used in this study can be seen in Table 2.3 and a specimen after the flow time test can be seen in Figure 2.14.

Table 2.3: Flow Number Test Results

Sample ID	Dynamic Creep Parameters		
	a ($\times 10^{-6}$)	b	FN
1	335.02	0.4459	1494
2	341.71	0.4518	842
Average	338.37	0.4489	1168

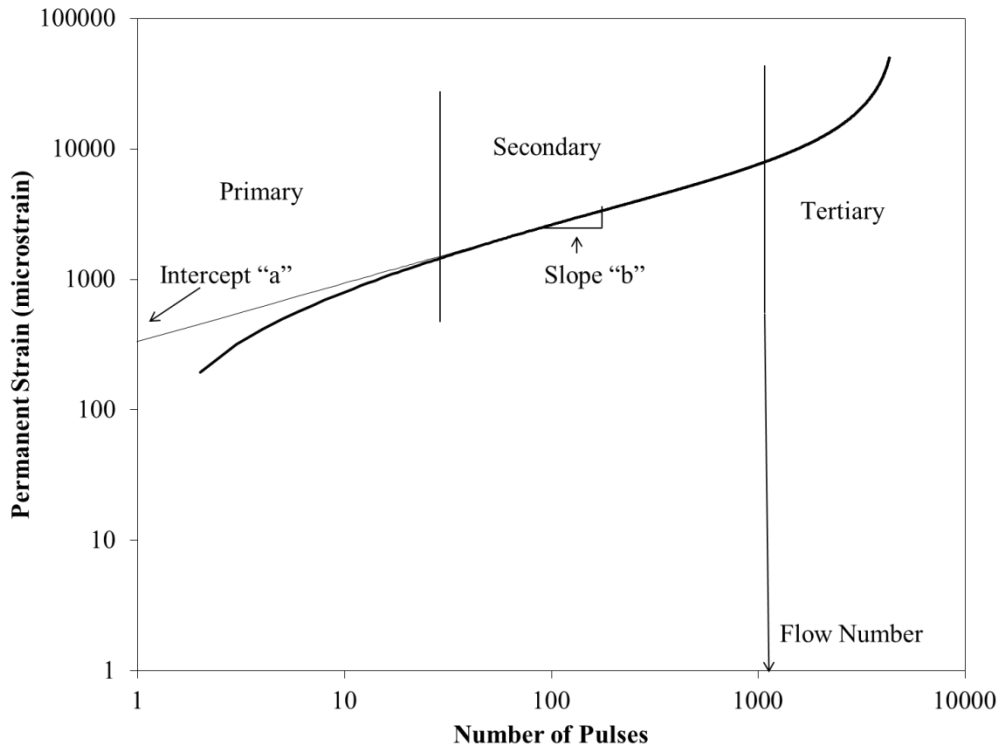


Figure 2.13: Permanent Strain versus Number of Cycles (After Brown et al., 2009)



Figure 2.14: Failed Specimen

2.4.2 In-place Testing

2.4.2.1 Density

The in-place density in both tests was 92% of the theoretical maximum specific gravity of 2.452. This density was measured using a nuclear gage.

2.4.2.2 Falling Weight Deflectometer

Falling weight deflectometer (FWD) testing is a non-destructive test used to evaluate pavement structural condition. A weight is dropped to cause a dynamic load to be applied to the pavement structure that simulates a moving wheel load. Geophones at various distances from the loading plate measure the surface deflections on the pavement. Deflection measurements are input in a backcalculation program to determine the modulus of each pavement structure layer (TxDOT, 2008). In most cases, backcalculation is an iterative elastic analysis of pavement surface deflection basin. Measured deflections are compared to the calculated deflections with associated layer moduli until a reasonable match is reached (WSDOT, 2005). KDOT performed

the FWD testing for this study using a Dynatest FWD, shown in Figure 2.15. Testing was conducted after the completion of paving and at scheduled intervals during APT loading. The Washington State Department of Transportation (WSDOT) has developed the Everseries backcalculation program that was used in this study. Variables that were set in the backcalculation process are listed in Table 2.4, and the resulting backcalculated moduli are tabulated in Table 2.5 and Table 2.6. Due to the pits being surrounded by concrete on three sides and at the bottom and to reduce the percent root mean square (%RMS) error, only the first four sensors were used during backcalculation. During the first test, the control section had the strongest base layer. In the second test, the modulus became higher through the first 500,000 passes and then started to decrease. Backcalculation results verified a stronger subgrade in the second test compared to the first test.



Figure 2.15: KDOT Dynatest FWD

Table 2.4: Everseries Variables

Variable	Set Point
Depth	Cross section dependent
Poisson Ratio	
HMA	0.35
Base/Geocell Layer	0.4
Subgrade	0.45
Concrete Bottom	0.45
Targeted %RMS	<1%
Analyzed Loads	≈9,000 lbs
Number of Sensors used	4

Table 2.5: Backcalculated Moduli for First Experiment and Overlay Experiment

	Layer	Number of Passes		
		0K	0K OL	50K OL
CTL	HMA (MPa)	3954	2557	3789
	Base (MPa)	115	93	106
	Subgrade (MPa)	64	61	60
QW	HMA (MPa)	3083	1417	2053
	Base (MPa)	43	338	308
	Subgrade (MPa)	39	47	54
RAP	HMA (MPa)	2165	1426	2518
	Base (MPa)	34	36	115
	Subgrade (MPa)	43	43	47
AB3	HMA (MPa)	2154	1416	2057
	Base (MPa)	35	235	596
	Subgrade (MPa)	45	44	49

Table 2.6: Backcalculated Moduli for Second Experiment

	Layer	Number of Passes				
		0K	250K	500K	1M	1.2M
CTL	HMA (MPa)	6468	5425	5507	4333	8650
	Base (MPa)	308	352	358	179	69
	Subgrade (MPa)	68	63	71	88	101
QW	HMA (MPa)	4867	6569	4511	3451	6602
	Base (MPa)	328	388	545	112	122
	Subgrade (MPa)	52	55	58	63	71
RAP	HMA (MPa)	4947	4947	3977	3608	9000
	Base (MPa)	140	311	325	89	58
	Subgrade (MPa)	58	66	75	84	81
AB3	HMA (MPa)	3848	5212	3020	3268	5536
	Base (MPa)	193	212	279	35	44
	Subgrade (MPa)	59	53	55	64	62

Chapter 3: Description of the Experiment

3.1 CISL 16 Experiment

CISL projects are numbered in the order that the experiment is conducted. This project was the 16th CISL experiment. The objective of the APT portion of the project was to test a geocell design with different infill materials and a thin HMA overlay under simulated traffic on a marginal subgrade. Three types of infill material (crushed limestone, AB-3; quarry waste [QW]; and reclaimed asphalt pavement [RAP]) were tested. Two pits were subdivided into two test sections, or lanes, each. These lanes were expected to be loaded to 1,000,000 repetitions in the bi-directional mode by an 80-kN (18-kip) single axle load assembly. Due to premature failures and machinery breakdowns, three experiments were conducted. The experiments were named: first (thin) experiment, overlay experiment, and second (thick) experiment.

All three experiments were conducted under similar test conditions. The single-axle, dual-tire bogie with a tire pressure of 552 kPa (80 psi) was used in these experiments. The experiments were conducted at a temperature of 23 °C (73 °F). A traffic wander of ± 150 mm (± 6 inches) was used in all three experiments. A complete wander from -150 mm (-6 inches) to +150 mm (+6 inches) took 676 passes. The wheel wander distribution, a truncated normal distribution, can be seen in Figure 3.1.

The test lanes were fully instrumented with stress and strain sensors, as shown in Figure 3.2. Data was recorded using a compact data acquisition system during load application at prescribed intervals for a full wander cycle (676 passes). The instrumentation included: four H-Bar strain gages below the HMA layer; two Type T thermocouples below the HMA layer; two pressure cells below the base layer; and five strain gages glued with epoxy to the geocell walls.

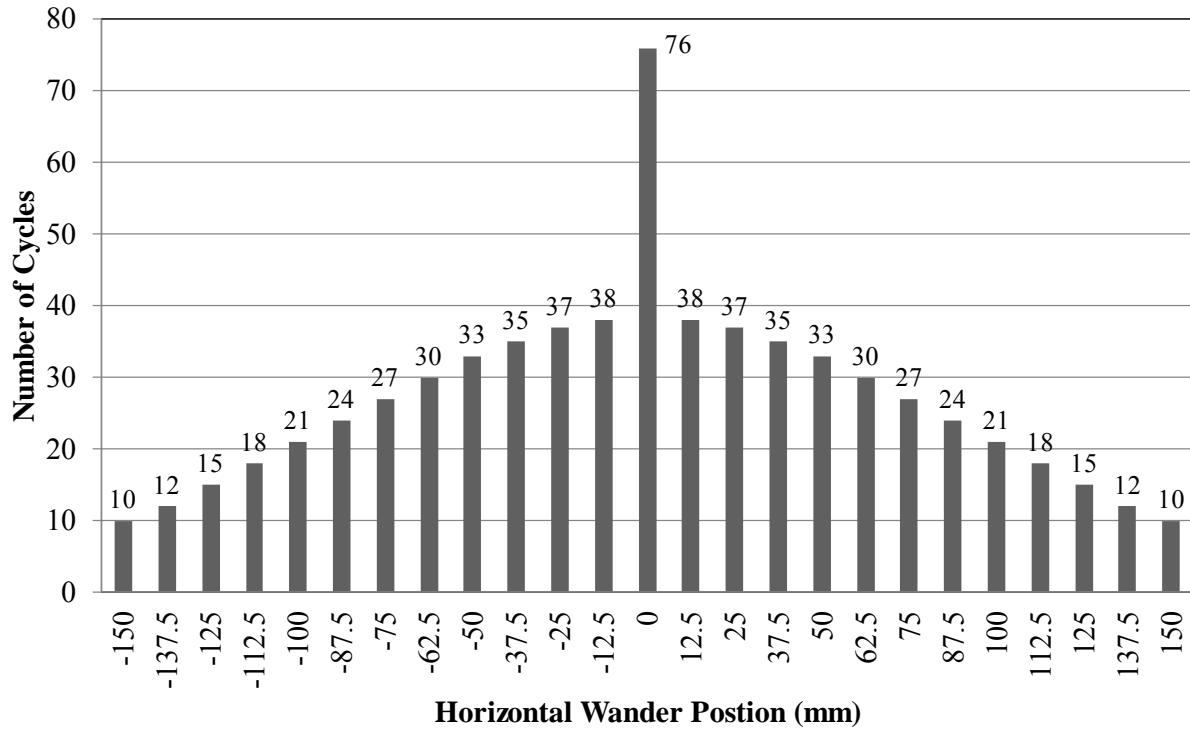


Figure 3.1: Wheel Wander Distribution

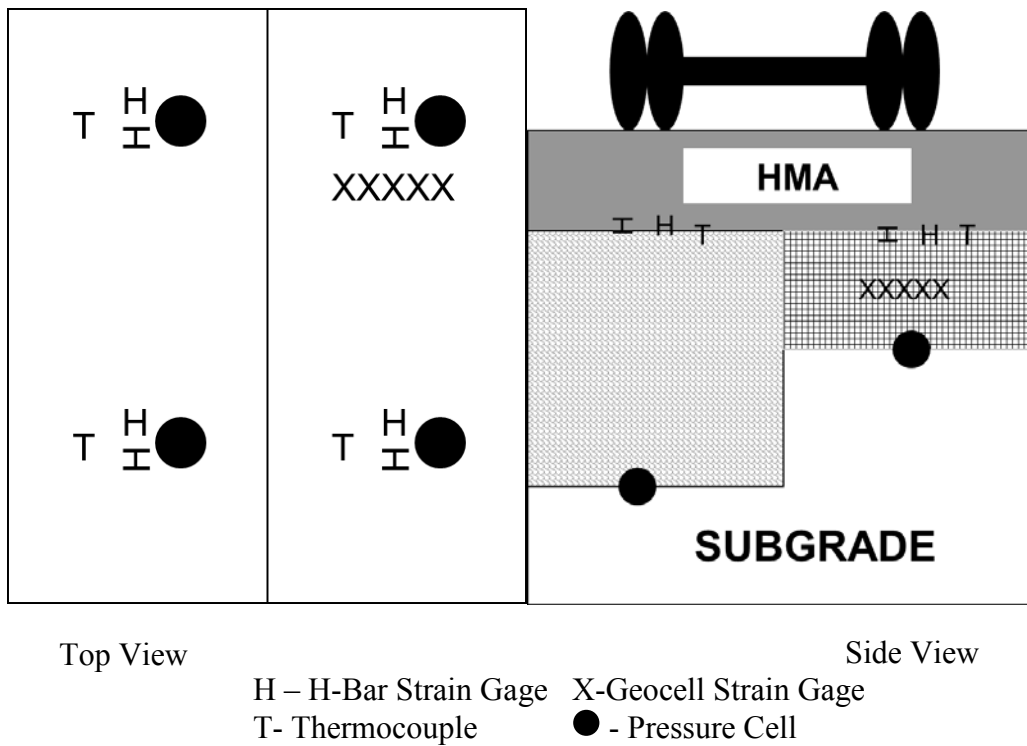


Figure 3.2: Instrumentation Layout

3.2 General Test Preparation

The pavement test sections in this study were built in similar fashion. A-7-6 clay soil was placed in 150-mm (6-inch) lifts. In the first experiment, the subgrade was compacted with a combination of a “jumping jack” compactor and a vibratory plate compactor. In the second experiment, a sheepsfoot trench compactor was used to do compaction. Compaction level was checked using a Dynamic Cone Penetrometer (DCP) until the desired CBR for each lift was reached. Pressure cells were installed on top of the subgrade as seen in Figure 3.3. A layer of non-woven geotextile was placed on top of the subgrade. The geotextile was used as a separation layer only; no reinforcement credit was expected out of it. Steel bars were driven into the subgrade to hold the geocells during installation and placement of infill as seen in Figure 3.4.

After the infill materials were placed in the geocells, the steel bars were removed and the vibratory plate compactor was used to start compaction of the infill, as seen in Figure 3.5. A 3,600-kg (4-ton) roller compactor was used to finish that compaction of the infill and cover as seen in Figure 3.6. By using the roller compactor, the target density of the infill in all test sections was more easily reached. The target density was 95% of the maximum dry density as determined by the standard Proctor tests. Infill density was determined using a nuclear density gage.



Figure 3.3: Pressure Cells Installed in Subgrade



Figure 3.4: Geocell Installation



Figure 3.5: Infill after Vibratory Plate Compaction



Figure 3.6: Roller Compaction of Infill

Once the base layer (geocells with infill) was compacted to the desired level, H-bar strain gages and thermocouples were installed on top of the base layer. HMA was produced, delivered, and placed by a local contractor. A Superpave HMA mix was placed with a lightweight asphalt paver as seen in Figure 3.7. The strain gages and thermocouples were covered before paving commenced in an attempt to protect them. A 3,940-kg (4.3-ton) asphalt roller compactor was used to compact the HMA as shown in Figure 3.8. The target density of 92% of theoretical maximum density was intended. A nuclear density gage was used to test for density compliance. After paving, KDOT performed FWD testing before any APT loading started. An initial profile was taken using a transverse profiler, shown in Figure 3.9. APT testing started as soon as all the preliminary testing was completed. Profiles were taken at scheduled intervals. FWD testing was also completed after scheduled intervals.

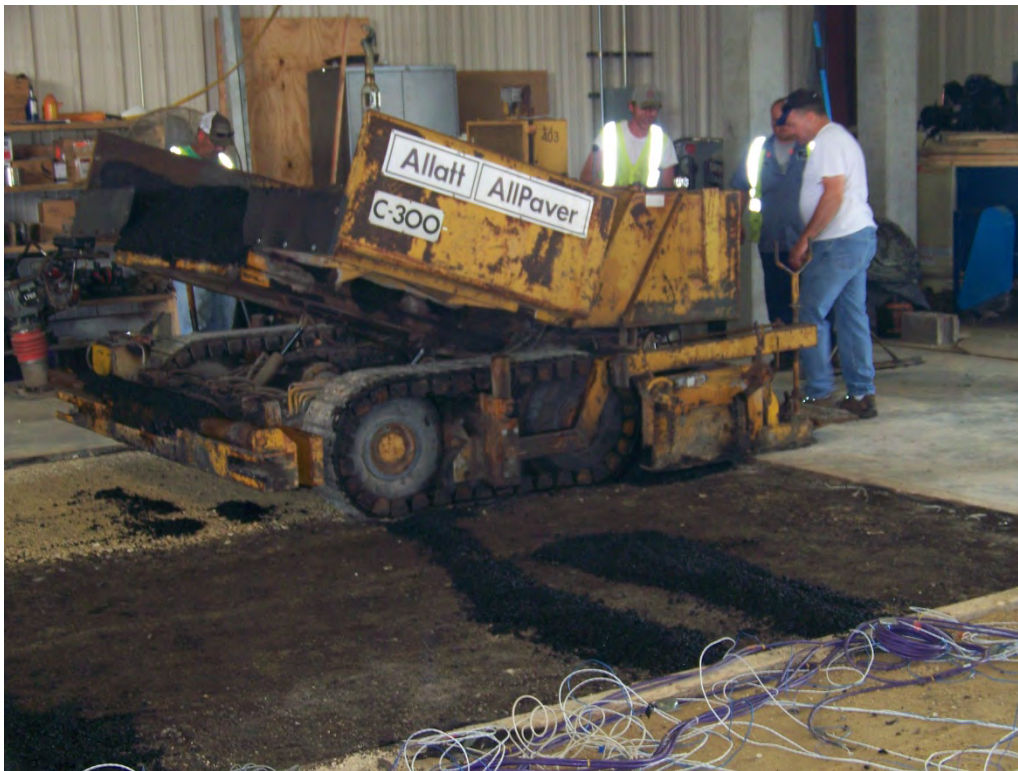


Figure 3.7: Lightweight Asphalt Paver



Figure 3.8: Asphalt Compactor



Figure 3.9: Transverse Profiler

3.2.1 First (Thin) Experiment

The first experiment consisted of four paved test lanes. The original four lanes consisted of the following base thicknesses and a 50-mm HMA layer, as shown in Figure 3.10:

- Lane 1 – 300-mm thick crushed limestone (AB-3) aggregate (control)
- Lane 2 – 75-mm geocell-reinforced quarry waste (QW) plus 25-mm cover
- Lane 3 – 75-mm geocell-reinforced reclaimed asphalt pavement (RAP) plus 25-mm cover
- Lane 4 – 75-mm geocell-reinforced AB-3 plus 25-mm cover

The subgrade was compacted to a CBR of 6% at a moisture content of 21%. The control section out of AB-3 was compacted with a moisture content of 9.2% and a dry density of 2.03 g/cm^3 (126.73 pcf), and the AB-3 geocell reinforced section was compacted at 9.0% moisture content to a dry density of 2.03 g/cm^3 (126.73 pcf). The quarry waste-geocell reinforced section was compacted at 10.6% moisture content dry density of 1.95 g/cm^3 (121.73 pcf), and the RAP-geocell reinforced section was compacted at 6.4% moisture content dry density of 1.78 g/cm^3 (111.12 pcf). HMA was compacted until a density of 2.250 g/cm^3 (140 pcf) was reached. Under APT loading, the thin test sections failed quickly. The QW lane failed dramatically as seen in Figure 3.11. A steel plate was placed over the failed area to allow for continuation of testing other lanes. The rest of the lanes also failed rather quickly as will be seen in Chapter 6. An overlay was decided to be placed in an attempt to continue testing.

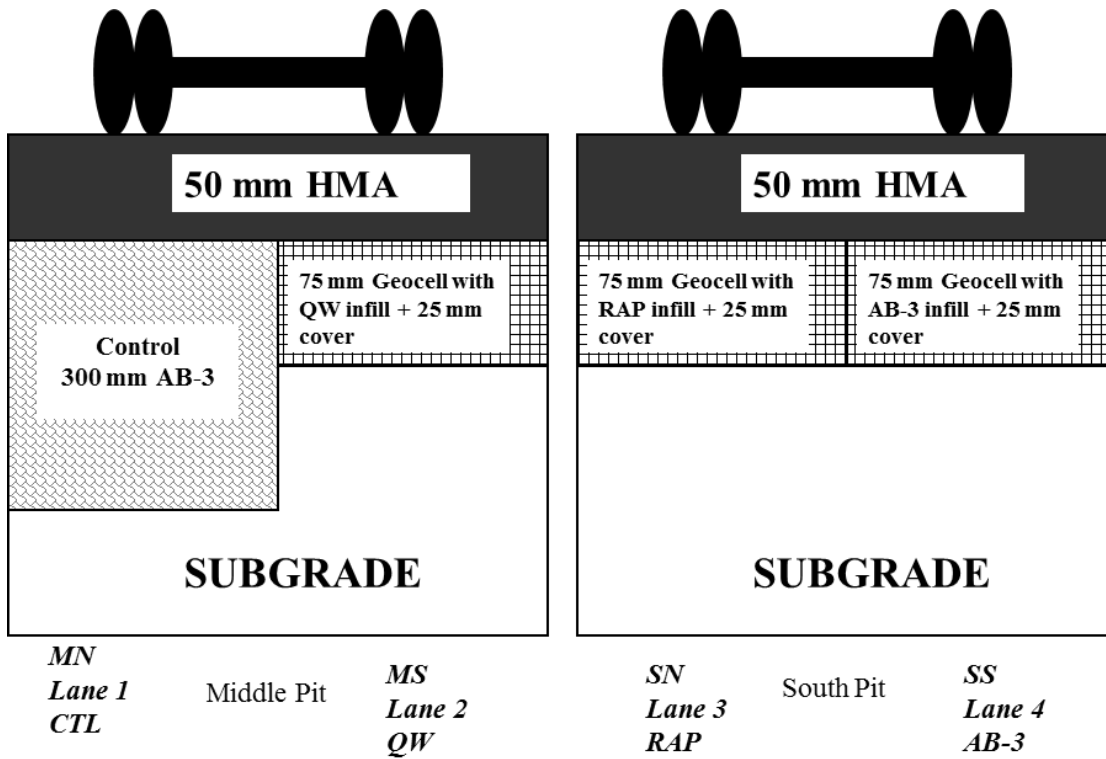


Figure 3.10: Thin Cross Sections



Figure 3.11: QW Lane Failure First Experiment

3.2.2 Overlay Experiment

A 37.5-mm (1.5-inch) HMA overlay was placed over the failing sections resulting in cross section shown in Figure 3.12. This overlay elevation was beyond the working range of the APT machine, resulting in multiple machine breakdowns. A decision was then made to terminate the testing.

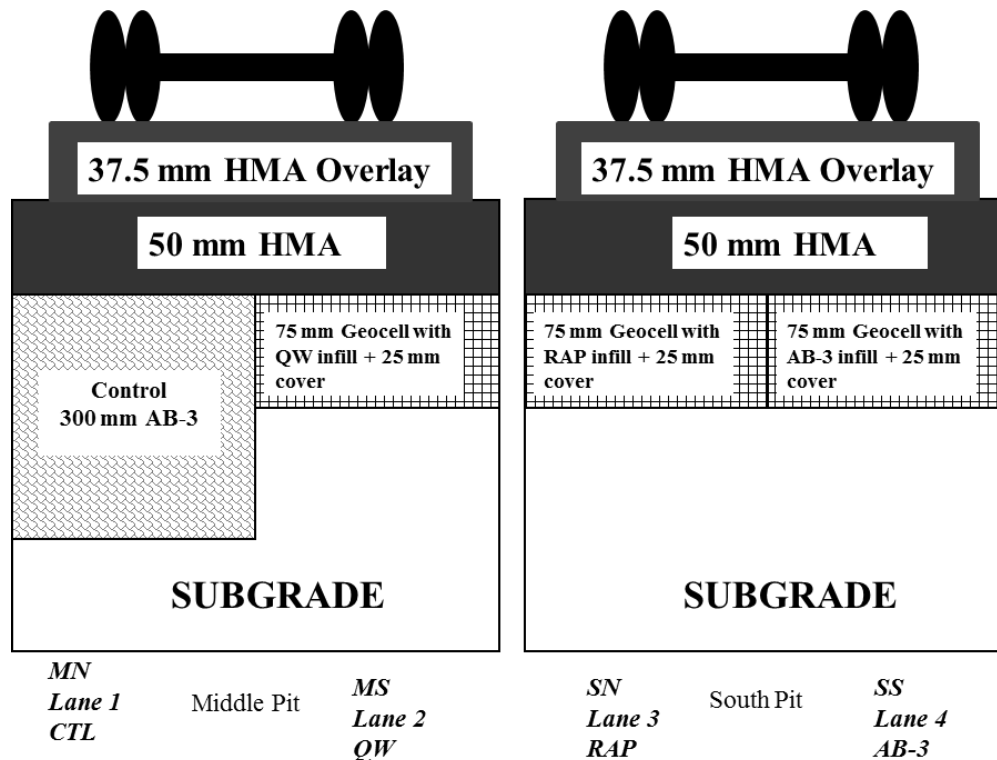


Figure 3.12: Overlay Cross Sections

3.2.3 Second (Thick) Experiment

Thicker cross sections were designed based on linear elastic evaluation of the stresses on the subgrade (as described later in Chapter 5). The subgrade was compacted to a CBR of 12% after calculations showed similar in-situ CBRs on most KDOT reconstruction projects. The subgrade was compacted at 18% moisture content. The sections were then reconstructed. The thicker cross sections had a 100-mm HMA layer with the following base thicknesses (shown in Figure 3.13):

- Lane 1 – 200-mm thick AB-3 aggregate (control)
- Lane 2 – 100-mm geocell reinforced QW plus 50-mm cover
- Lane 3 – 100-mm geocell reinforced RAP plus 50-mm cover
- Lane 4 – 100-mm geocell reinforced AB-3 plus 50-mm cover

The control section out of AB-3 was compacted with a moisture content of 6.7% and a dry density of 2.03 g/cm³ (126.73 pcf), and the AB-3 geocell reinforced section was compacted at 6.3% content to a dry density of 1.97 g/cm³ (122.98 pcf). The quarry waste-geocell reinforced section was compacted at 6.8% moisture content and a dry density of 1.97 g/cm³ (122.98 pcf), and the RAP-geocell reinforced section was compacted at 6.4% moisture content with a dry density of 1.81 g/cm³ (112.99 pcf). HMA was compacted until a density of 2.250 g/cm³ (140 pcf) was reached.

APT machine passes were to be applied until 500,000 passes or a rut depth of 12.5 mm was reached whichever came first. The second test section performed very well, and due to the completion of 500,000 passes without failure, it was decided to apply 1,200,000 passes.

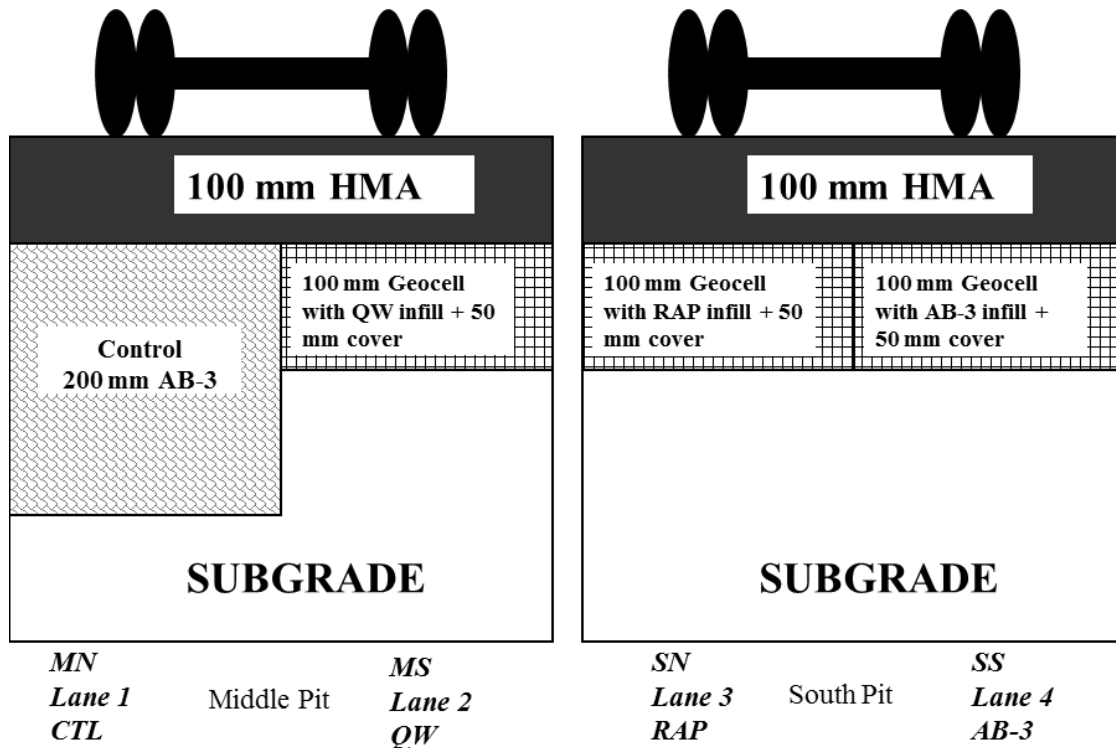


Figure 3.13: Thick Cross Sections

Chapter 4: Numerical Simulation of APT Tests

4.1 Introduction

Abaqus, commercially available finite element (FE) software, was used to numerically simulate the geocell-reinforced sections under APT tests. Material properties obtained from testing and simulation in addition to actual geometry and boundary conditions were used in the models. Two dimensional models cannot account for the three-dimensional effects of geocells. Due to the high costs of APT testing, validation by numerical modeling increases the reliability of future analysis with less cost.

4.2 Numerical Simulations

Two types of numerical analysis were conducted. The first simulation evaluated the response in the base and subgrade during the APT tests. Rutting in the HMA layer was evaluated in the second simulation.

4.2.1 Material Properties

Material properties were determined from the laboratory and in-situ tests. In the first simulation, the base material was modeled with Mohr-Coulomb plasticity. HMA layers were considered as linear elastic. Geocells were modeled as elastic materials since no damage to the geocells were seen during testing. The material properties used are tabulated in Table 4.2. The geocells were modeled as diamonds to simplify meshing while maintaining basic reinforcing functionality. Yang (2010) and Leshchinsky and Ling (2013) were successful in modeling multiple geocells as diamonds.

In the second simulation, the base material was modeled as linear elastic. HMA layers were considered as visco-elastic. Geocells were modeled as elastic materials as in the first test. Creep tests were conducted on the HMA and subgrade materials. The creep results can be seen in Table 4.1. When rut simulations were conducted with the properties obtained from test data, the results were not within reason of the actual results. A shallow U-shaped rut profile emerged as seen in Figure 4.1. A W-shaped rut profile, as obtained with a transverse profiler, could be developed by calibrating the material properties. It was found that using one-half of the HMA

modulus with creep parameters of $1.00\text{E-}04$, 0.47 , and -0.5 and one-third of the base modulus returned more accurate results. The material properties used are tabulated in Table 4.3.

Table 4.1: HMA Creep Test Results

	A	m	n
HMA Sample 1	$1.10\text{E-}09$	-0.764	0.97191
HMA Sample 2	$1.0\text{E-}09$	-0.8277	0.96279
HMA Sample 3	$1.00\text{E-}09$	-0.709	0.93499
Subgrade Average	$5.26\text{E-}05$	-0.58	0.6

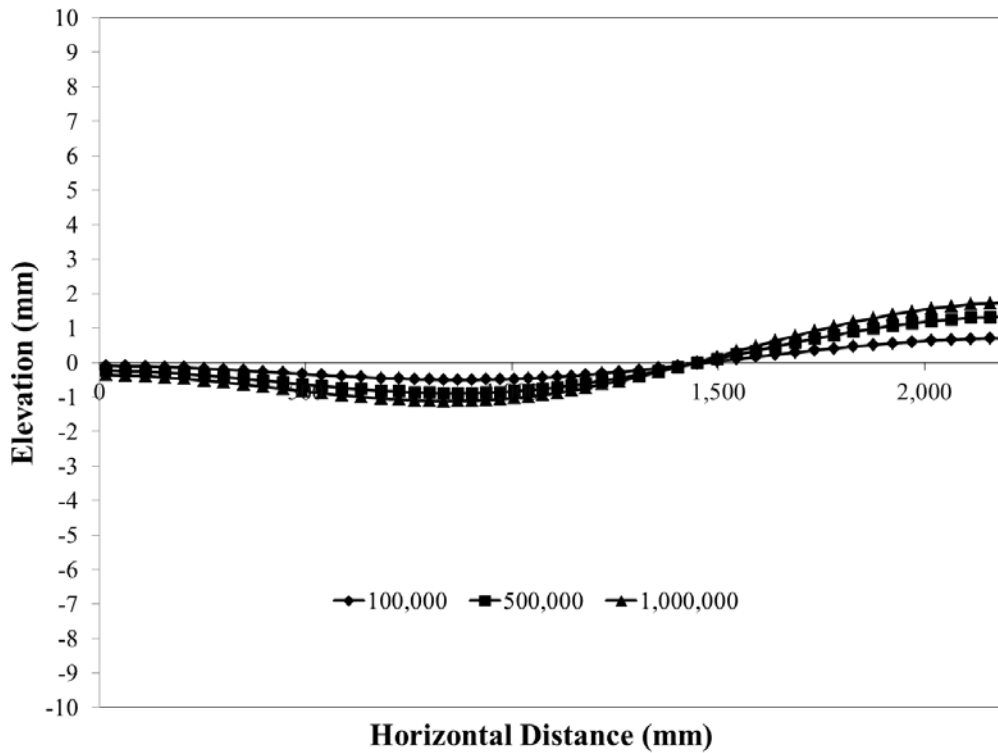


Figure 4.1: Simulated U-Shaped Rut Profile

Table 4.2: First Numerical Simulation Properties of Materials

Material	Lane	CTL	CTL	CTL	QW	QW	QW	RAP	RAP	RAP	AB3	AB3	AB3
	Test #	1	OL	2									
Subgrade	Density (tonne/mm ³)	1.52E-06	1.52E-06	1.56E-06									
	E (MPa)	64	64	68	39	39	52	43	43	58	45	45	59
	v	0.45	0.45	0.45	0.45	0.45	0.45	0.45	0.45	0.45	0.45	0.45	0.45
	Friction Angle	0	0	0	0	0	0	0	0	0	0	0	0
	Dilation Angle	0	0	0	0	0	0	0	0	0	0	0	0
	Cohesion (MPa)	0.104	0.104	0.104	0.104	0.104	0.104	0.104	0.104	0.104	0.104	0.104	0.104
Base	Density (tonne/mm ³)	2.03E-06	2.03E-06	2.03E-06	1.95E-06	1.95E-06	1.95E-06	1.78E-06	1.78E-06	1.81E-06	2.03E-06	2.03E-06	1.97E-06
	E (MPa)	115	115	308	43	43	328	34	34	140	35	35	193
	v	0.4	0.4	0.4	0.4	0.4	0.4	0.4	0.4	0.4	0.4	0.4	0.4
	Friction Angle	47.2	47.2	47.2	47.2	47.2	47.2	37	37	37	47.2	47.2	47.2
	Dilation Angle	17.2	17.2	17.2	17.2	17.2	17.2	7	7	7	17.2	17.2	17.2
	Cohesion (MPa)	0.0047	0.0047	0.0047	0.005	0.005	0.005	0.05	0.05	0.05	0.0047	0.0047	0.0047
GC	E (MPa)	550	550	550	550	550	550	550	550	550	550	550	550
	v	0.45	0.45	0.45	0.45	0.45	0.45	0.45	0.45	0.45	0.45	0.45	0.45
HMA	Density (tonne/mm ³)	2.26E-06											
	E (MPa)	3954	3954	6468	3083	3083	4867	2165	2165	4947	2154	2154	3848
	v	0.3	0.3	0.3	0.3	0.3	0.3	0.3	0.3	0.3	0.3	0.3	0.3

Table 4.3: Second Numerical Simulation Properties of Materials

	Lane	CTL	CTL	CTL	QW	QW	QW	RAP	RAP	RAP	AB3	AB3	AB3
	Test #	1	OL	2									
Subgrade	Density (tonne/mm³)	1.52E-06	1.52E-06	1.56E-06									
	E (MPa)	64	64	68	39	39	52	43	43	58	45	45	59
	v	0.45	0.45	0.45	0.45	0.45	0.45	0.45	0.45	0.45	0.45	0.45	0.45
	Power Law Multiplier	5.26E-05											
	Eq Stress Order	0.6	0.6	0.6	0.6	0.6	0.6	0.6	0.6	0.6	0.6	0.6	0.6
	Time Order	-0.58	-0.58	-0.58	-0.58	-0.58	-0.58	-0.58	-0.58	-0.58	-0.58	-0.58	-0.58
Base	Density (tonne/mm³)	2.03E-06	2.03E-06	2.03E-06	1.95E-06	1.95E-06	1.95E-06	1.78E-06	1.78E-06	1.81E-06	2.03E-06	2.03E-06	1.97E-06
	E (MPa)	38	38	102	14	14	109	11	14	47	12	12	64
	v	0.4		0.4	0.4	0.4	0.4	0.4	0.4	0.4	0.4	0.4	0.4
GC	E (MPa)	550	550	550	550	550	550	550	550	550	550	550	550
	v	0.45	0.45	0.45	0.45	0.45	0.45	0.45	0.45	0.45	0.45	0.45	0.45
HMA	Density (tonne/mm³)	2.26E-06											
	E (MPa)	1977	1977	3234	1541	1541	2433	1082	1082	2474	1077	1077	1924
	v	0.3	0.3	0.3	0.3	0.3	0.3	0.3	0.3	0.3	0.3	0.3	0.3
	Power Law Mutiplier	1.00E-04											
	Eq Stress Order	0.47	0.47	0.47	0.47	0.47	0.47	0.47	0.47	0.47	0.47	0.47	0.47
	Time Order	-0.5	-0.5	-0.5	-0.5	-0.5	-0.5	-0.5	-0.5	-0.5	-0.5	-0.5	-0.5

4.2.2 Boundary Conditions

To decrease the computational time required, only a quarter of the test pit was modeled. Since the pit is surrounded by concrete, displacement was set for the bottom and two sides (back and left) of the model. The left side was restrained from moving in the x-direction, and the bottom was restrained from moving in the z-direction. The front and right sides used symmetrical boundary conditions. The front used symmetry in the y-direction, while the right side used symmetry in the x-direction. Symmetry conditions were also included for the geocells as shown in Figure 4.2.

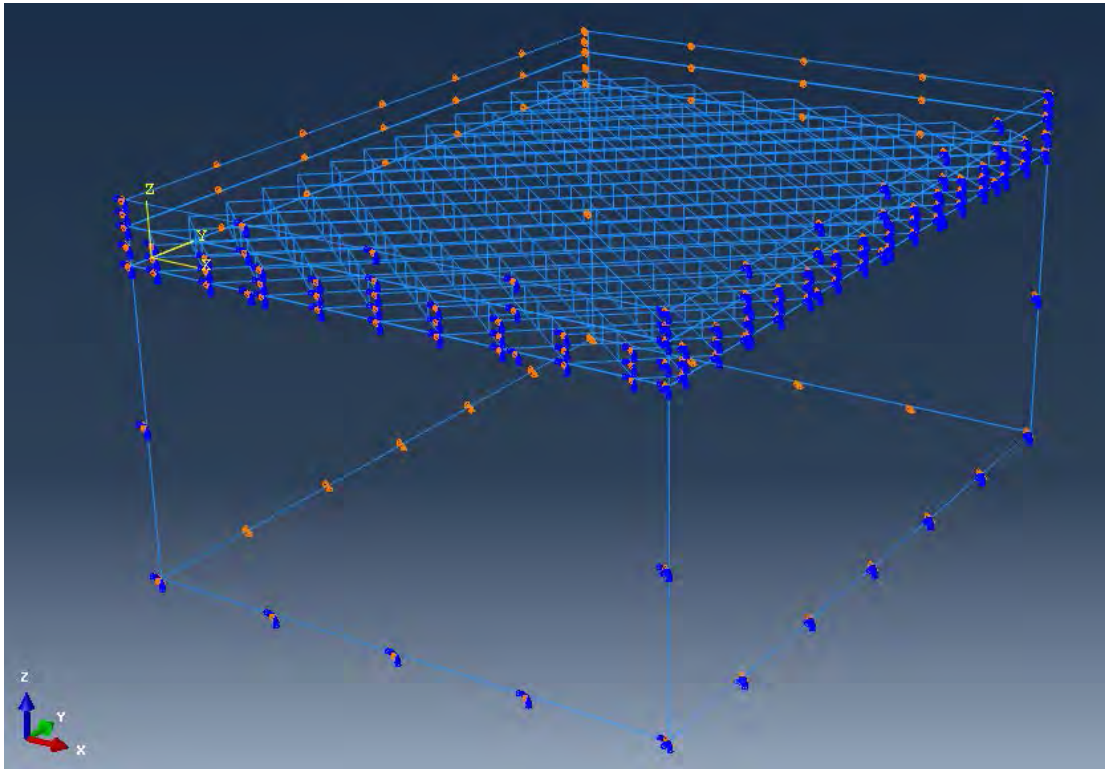


Figure 4.2: Boundary Conditions for APT Models

4.2.3 Element/Mesh

Solid materials (HMA, base material, and subgrade) were meshed using an 8-noded linear brick reduced integration hexahedral element (C3D8R). There was a tradeoff between accuracy and computational size. Coarser meshes tend to be inaccurate, while the finer mesh

increases computational time. For the geocell-reinforced section simulation a balance was found with the HMA layer (shown in Figure 4.3), base layer (shown in Figure 4.4), and subgrade (shown in Figure 4.5) having 1,716, 1,449, and 6,279 elements, respectively. Tie constraints were used at the interfaces between the HMA and the base material and between the subgrade and the base material to help in convergence issues. Geocells were meshed using 10,080 S4R 4-node doubly curved thin or thick shell, reduced integration elements as shown in Figure 4.6. Shell elements can be used when the ratio of one dimension is higher than the other dimensions (Dassault Systèmes, 2011).

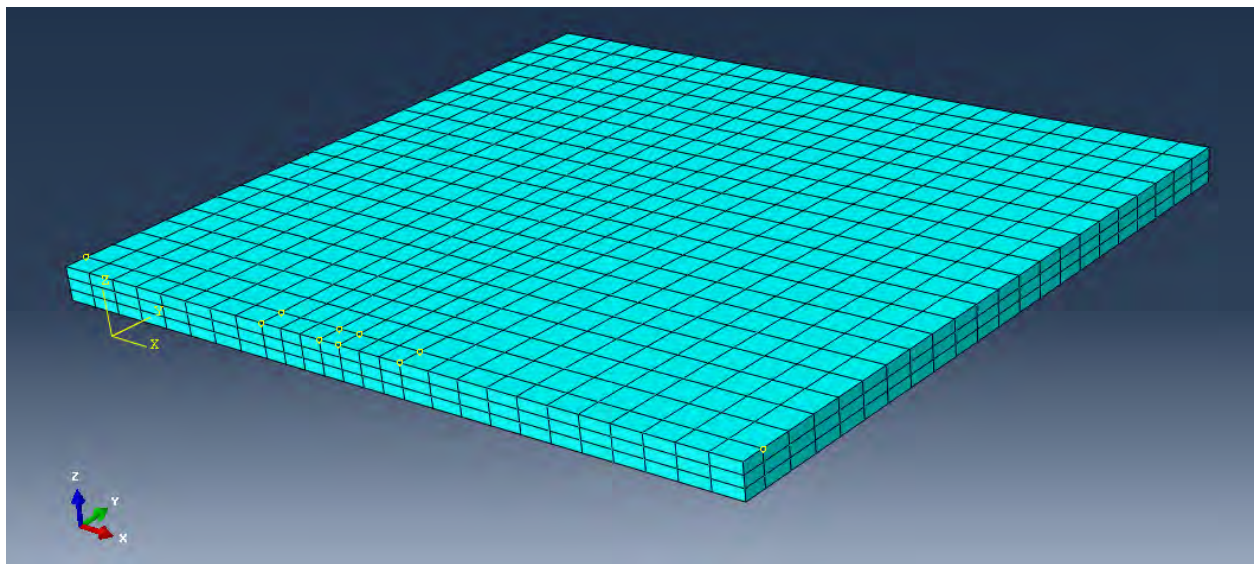


Figure 4.3: HMA Mesh

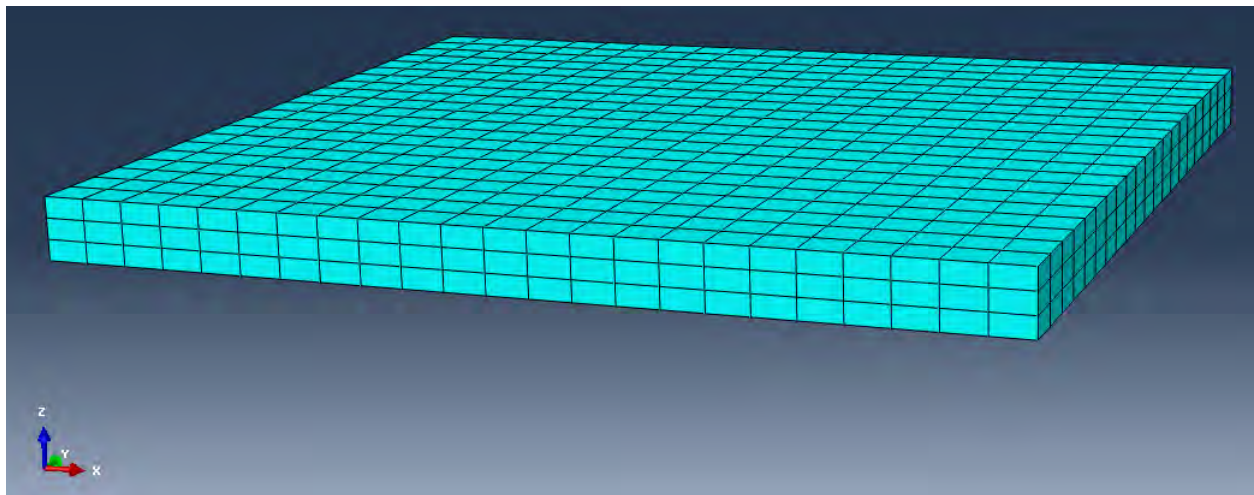


Figure 4.4: Base Mesh

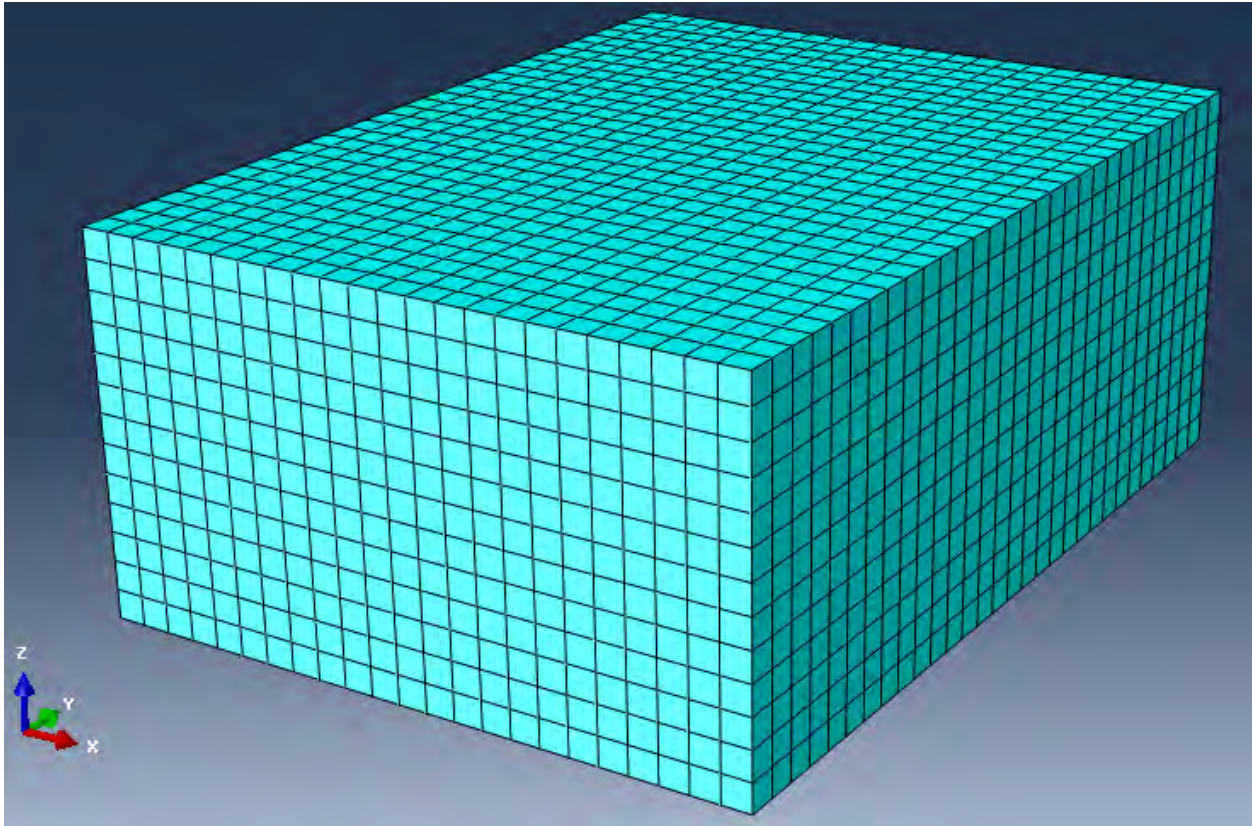


Figure 4.5: Subgrade Mesh

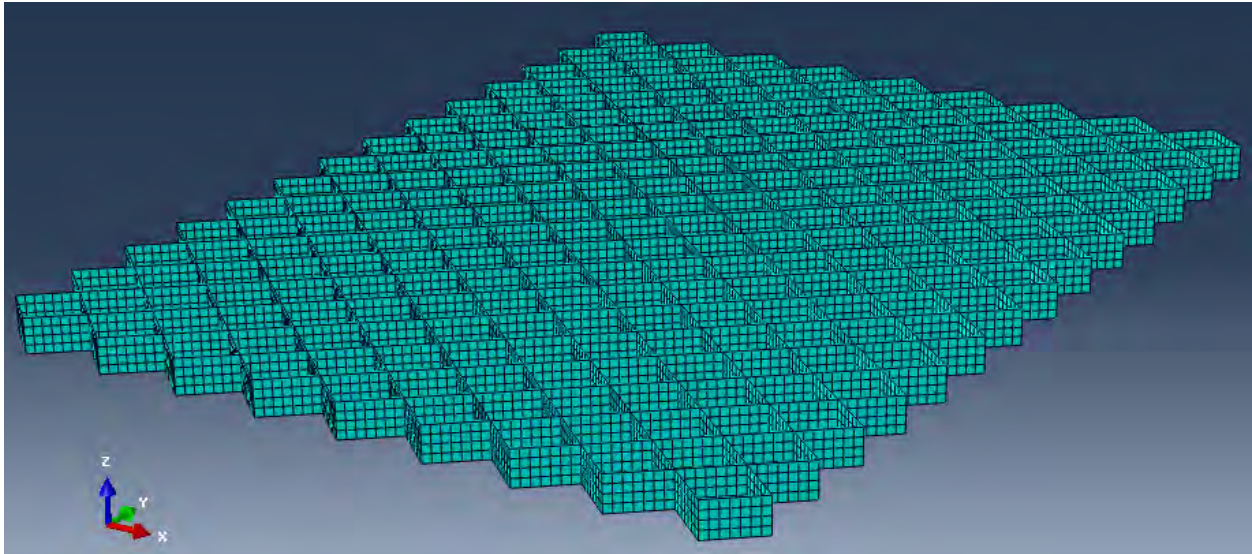


Figure 4.6: Geocell Mesh

An embedded region was used to place the geocells in the base layer. Embedded regions are a group of elements that are within a “host” region. The embedded region allows for shell elements to be embedded into solid elements as shown in Figure 4.7. The infill of the material was sandwiched between the HMA layer and the subgrade by not allowing movement of the infill. Embedded elements were constrained by the response of the host elements; therefore, no contact friction could be attributed to the geocell wall. However, due to the infill having no room to move to, it was assumed that the friction between the geocell wall and infill gave no or little help to the reinforcement. This is different in unpaved roads where the infill has room to move. Infill material in unpaved roads can be pushed out of the cells; therefore, the friction is important. The embedded region elements act in a slab-like motion. Since the control section had no geocells, the model used the same setup without the embedded geocell.

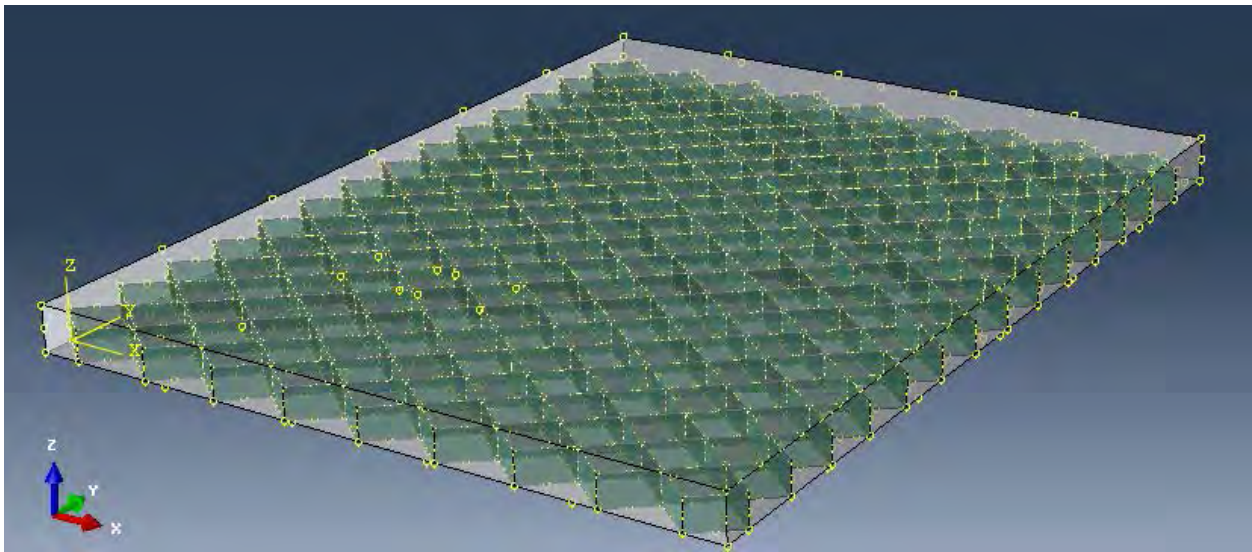


Figure 4.7: Embedded Geocells in Base Layer

4.2.4 Loading

4.2.4.1 Stress and Strain Simulation Loading

Loading of the model occurred over the area of the tire imprint at a given point in the load cycle. Symmetry was used for the half of the tire imprint, as shown in Figure 4.8. This type of loading represents the results obtained from the sensors. A static load was applied using

Abaqus/Explicit. Abaqus/Explicit analysis handles highly non-linear behavior of materials better than Abaqus/Standard (Implicit) analysis. Abaqus/Standard has convergence issues and very small time increments in soil analysis due to the yielding of the soil (Dassault Systèmes, 2011). The base material in this study has cohesion of less than 10% of the applied load. However, the creep material model is not available in Abaqus/Explicit, therefore, the HMA layer was modeled as a linear elastic material.

The load was applied as a pressure over an area equal to the tire imprint. The 80-kN (18- kip) total force was applied to the APT loading assembly through two sets of dual tires. A tire pressure of 552 kPa (80 psi) was maintained during testing. Rectangular tire imprints were assumed in this study, resulting in a total tire imprint of 208-mm (8.2-inches) wide (measured tire imprint width) x 174.5-mm (6.9-inches) long (calculated tire imprint length). The tire imprint length was divided into two due to symmetry. One load cycle on a unit tire imprint was calculated to take 0.05 seconds to pass. The step in the numerical analysis placed a pressure of 552 kPa (80 psi) on the tire imprint for 0.05 seconds.

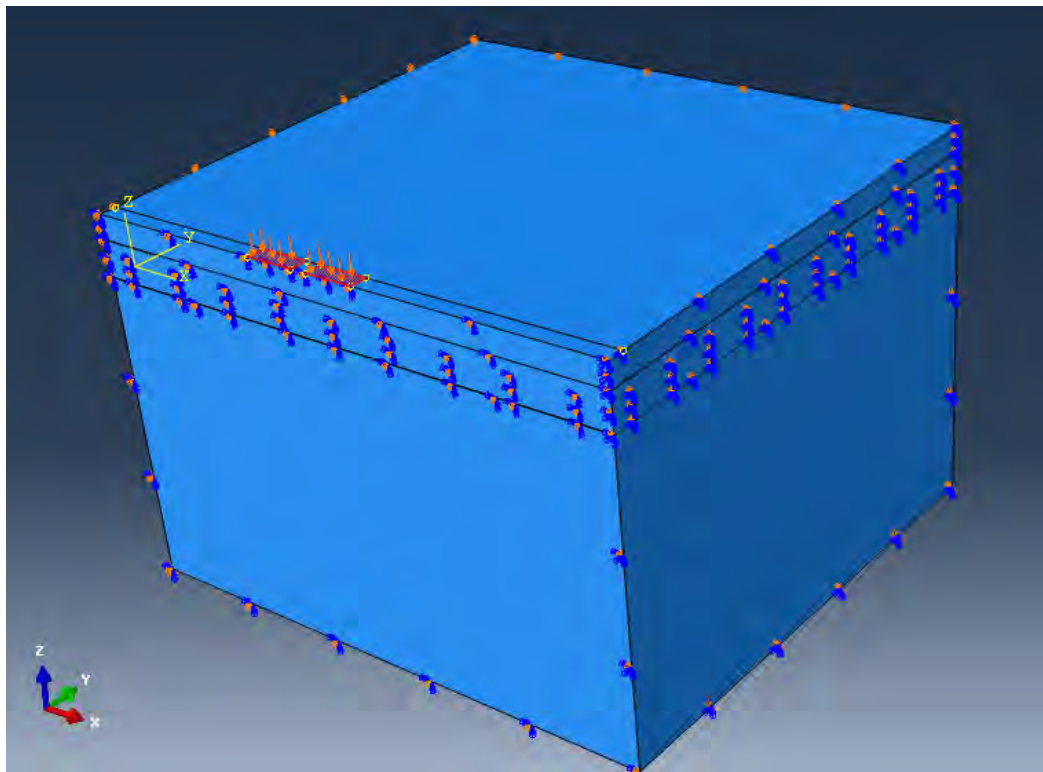


Figure 4.8: Loading of Model

4.2.4.2 Rut Simulation Loading

A load pressure of 552 kPa (80 psi) was applied to the tire imprint as seen in Figure 4.9. Rut depths were taken three times (at 100,000, 500,000, and 1,000,000 cycles) during the simulation. Seven steps were used to simulate the loading. A review of the steps can be seen in Table 4.4. Lateral wander was not taken into account during rut simulations.

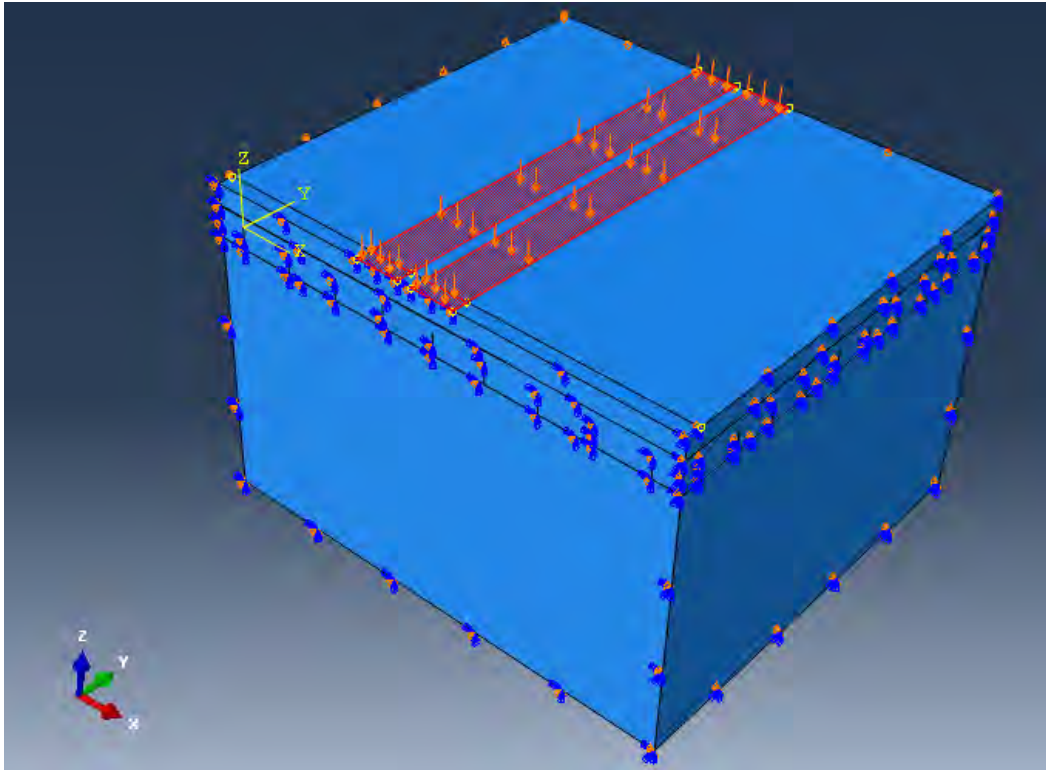


Figure 4.9: Rut Simulation Loading

Table 4.4: Rut Simulation Steps

Step	Duration (s)	Loading (kPa)	Comment
Initial	0	0	Setting up of Boundary Conditions
1	5,000	552	100,000 cycles
2	1	0	First rut depth measurements
3	20,000	552	Total cycles to 500,000
4	1	0	Second rut depth measurements
5	25,000	552	Total cycles to 1,000,000
6	1	0	Third rut depth measurements

Chapter 5: Results and Discussion

5.1 APT Test Results

Throughout APT testing, the instrumentation was used to record data for one wander cycle at specified load intervals. Vertical pressure on the subgrade, strain at the bottom of the HMA layer, and strain on the body of geocell were recorded. Transverse profiles were taken at regular intervals to measure rut depths.

5.1.1 First Experiment

In the first test, profiles showed dramatic changes in elevation as seen in Figure 5.1 and Figure 5.2. Some heaving was evident in Figure 5.2. This type of heaving usually corresponds to the shear failure of the base and subgrade layers. In the first set of test sections, the quarry waste (QW) section had a localized heaving failure, shown in Figure 3.11. The failure is believed to have been caused by the subgrade failure. No geocell material was found in the heaved area. Ruts on the control lane did not increase as rapidly as on the geocell-reinforced sections.

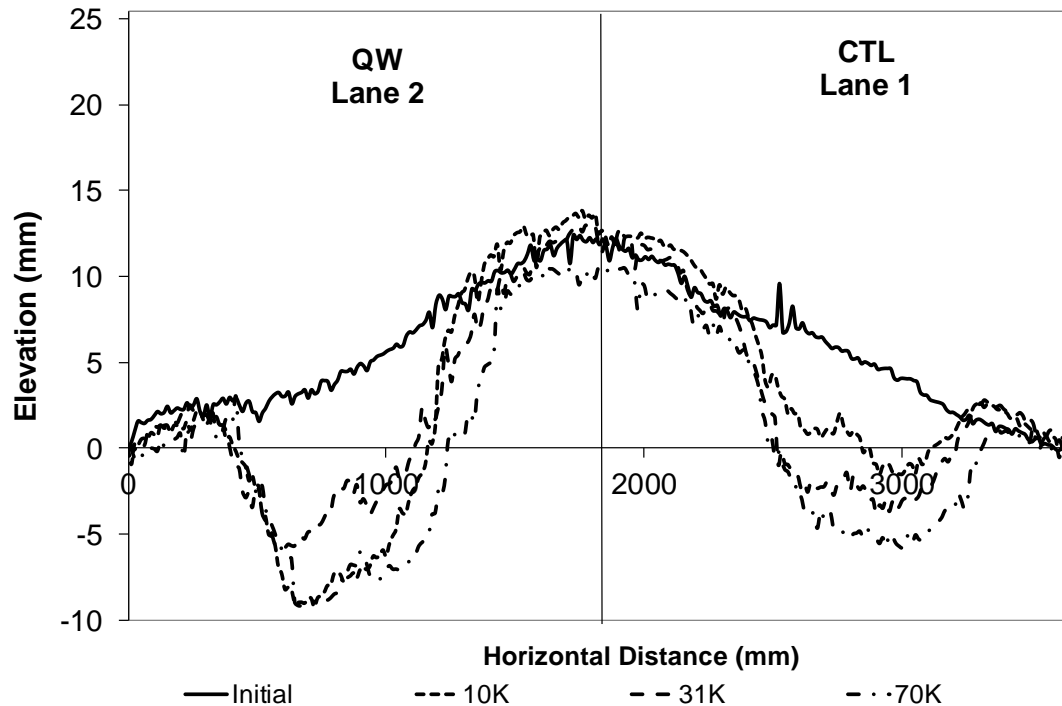


Figure 5.1: Typical Middle Pit Profile First Experiment

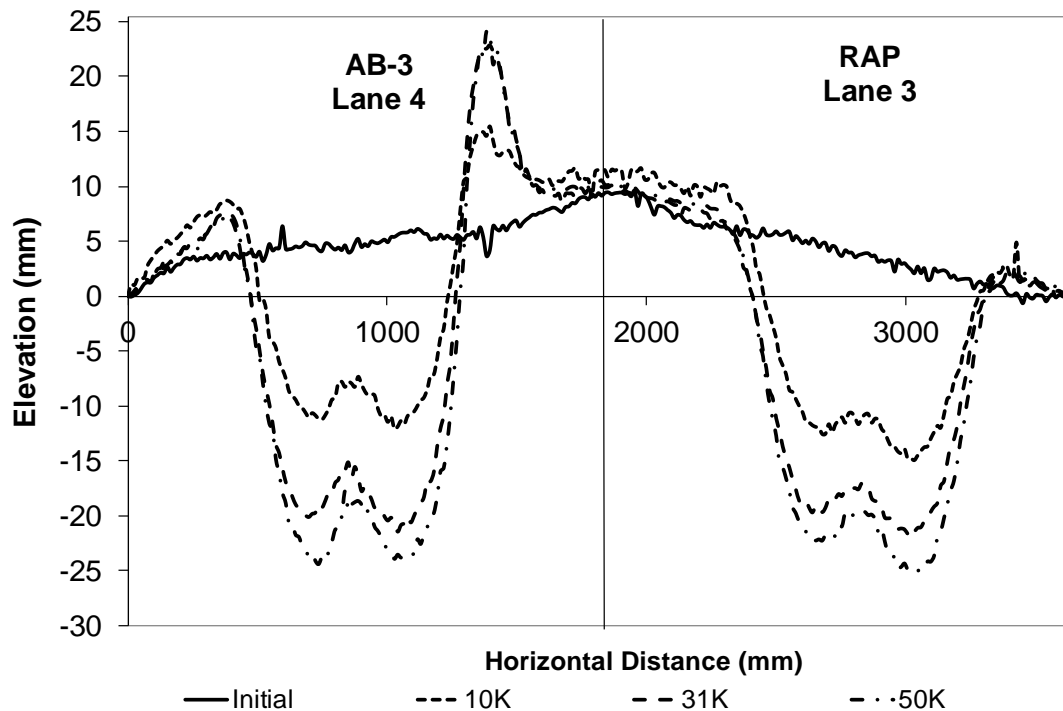


Figure 5.2: Typical South Pit Profiles First Experiment

Vertical pressures on the subgrade, shown in Figure 5.3 and Figure 5.4, show that all geocell-reinforced sections had higher vertical stress at the top of the subgrade than the control lane. The QW lane showed a very high vertical stress in one of the lane's two pressure gages. This pressure gage was located directly below the area that heaved. The pressure was greatly reduced after the steel plate was used to span the failed area. Average vertical pressure readings in the south pit were higher than the 104.6-kPa (15.17-psi) unconfined compressive strength of the subgrade soil.

Many strain gages on the geocells did not last through construction as seen in Table 5.1. The location of the geocell strain gages in the middle pit was covered with the steel plate; therefore, the strain recorded was not accurate and not shown. Traffic wander induced both compression and tension in the geocells. When the geocell strain gage was at a distance from the center of the loading, the geocell tended to be under compression while middle geocells were in tension. The reclaimed asphalt pavement (RAP) lane had the highest peak tensile strain of 3,524 microstrain and the lowest strain (compression) of -1,790 microstrain. The AB-3 lane had the

second highest tension and compressive strain with 2,462 microstrain and -1,254 microstrain, respectively. The QW lane had the lowest tension and compressive strain with 1,403 microstrain and -848 microstrain; however, the strain was recorded only for the first 676 passes before the lane heaved, and the strain readings were no longer meaningful.

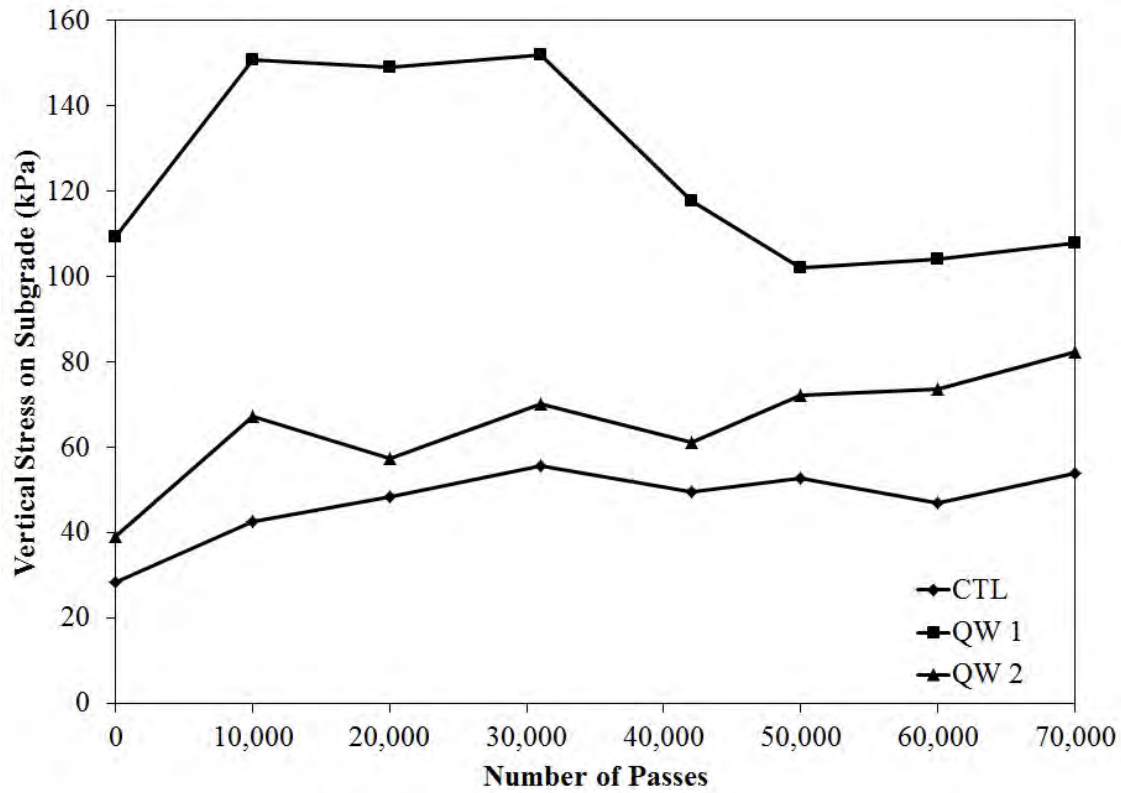


Figure 5.3: Vertical Pressure on Subgrade of the Middle Pit during First Experiment

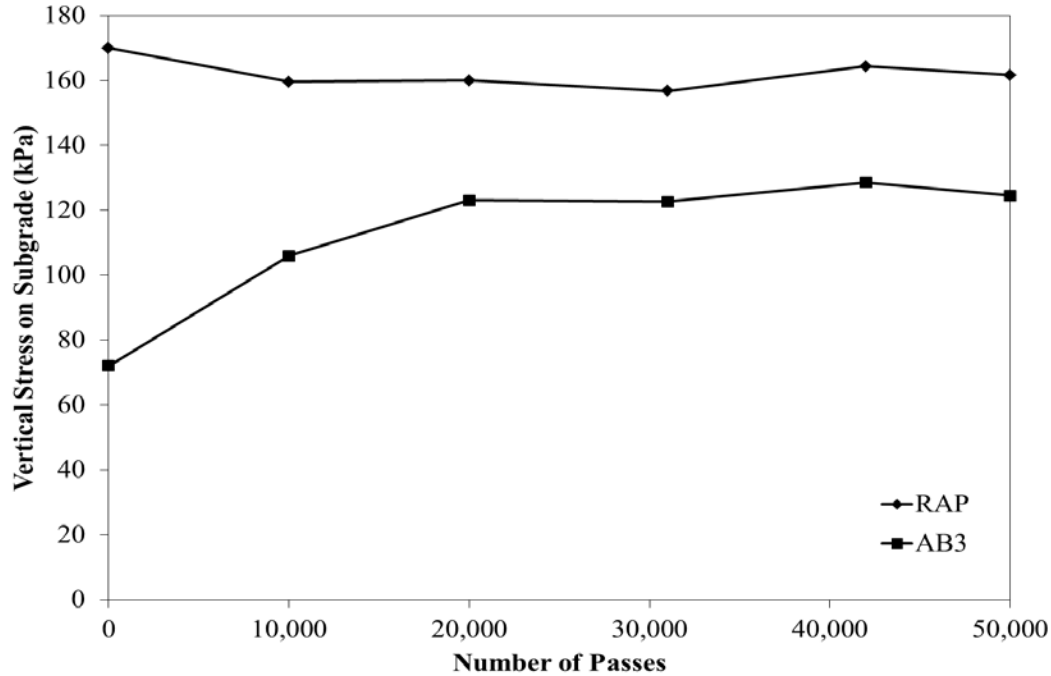


Figure 5.4: Vertical Pressure on Subgrade in South Pit for the First Experiment

Table 5.1: Geocell Peak Horizontal Microstrain First Experiment (Positive = Tension)

a. Middle Pit (QW Lane)

	Middle Pit				
	S				
Cycle	1	2	3	4	5
0	-0.000731	-0.000848	0.001403	0.001203	-0.000562
20K					
50K					

b. South Pit (RAP Lane)

	South Pit				
	N				
Cycle	1	2	3	4	5
0	-0.00179	0.003524		0.003523	
20K	-0.00065				
50K	-0.000677				

c. South Pit (AB-3 Lane)

	South Pit				
	S				
Cycle	1	2	3	4	5
0	0.000562	0.002252		0.000466	
20K	-0.0009	0.002462		0.00215	
50K	-0.00125	0.00245			

5.1.2 Overlay Experiment

Thicker cross sections led to the profiles not deteriorating as badly or as quickly as seen in Figure 5.5 and Figure 5.6. After the overlay was placed, the vertical stress was reduced and was more or less constant during testing as seen in Figure 5.7. Vertical pressure on subgrade of the middle pit in the overlay experiment is shown in Figure 5.7, and that in the south pit is shown in Figure 5.8. The south pit still had higher vertical stress on the subgrade than the middle pit, and larger than the unconfined compressive strength of the subgrade soil. While the overlay did lead to better performance, the APT machine was not designed to test pavements with high elevations above the top of the pits. After several major breakdowns, it was decided to discontinue testing.

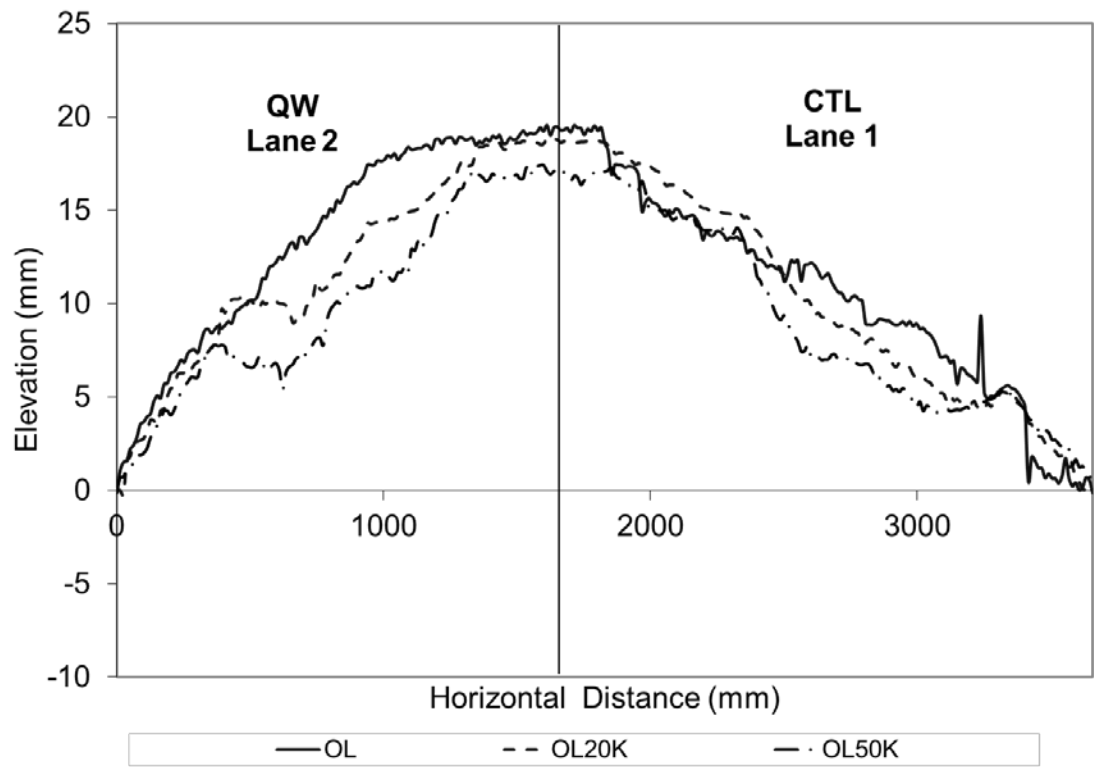


Figure 5.5: Typical Profile of Middle Pit after Overlay

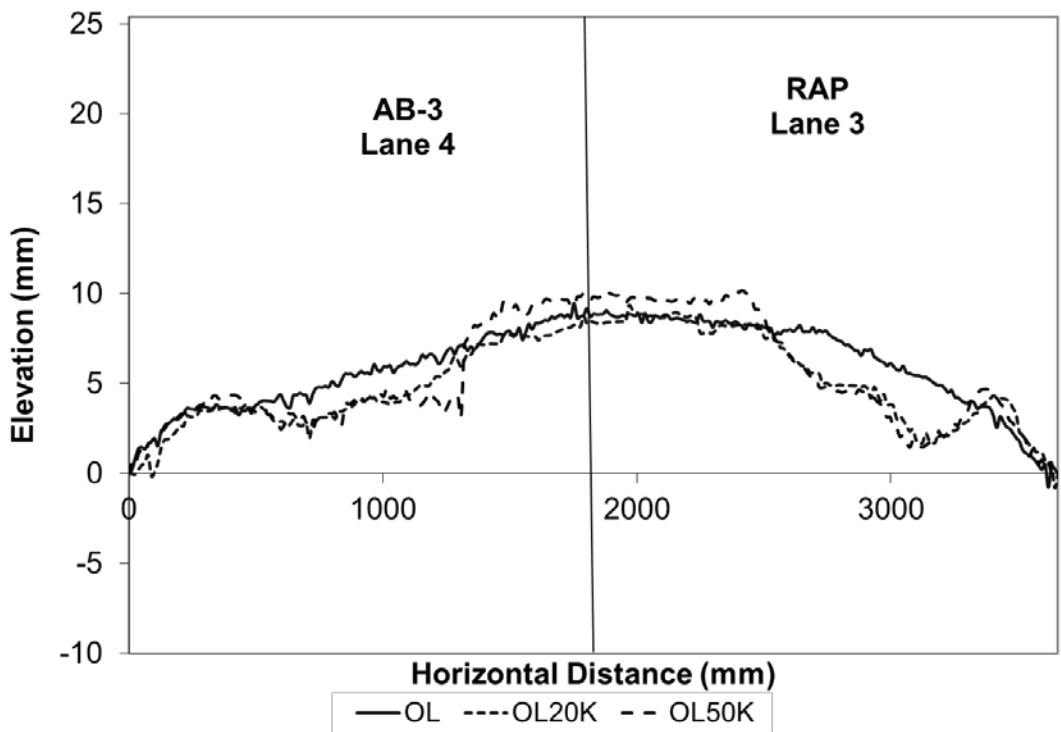


Figure 5.6: Typical Profile of South Pit after Overlay

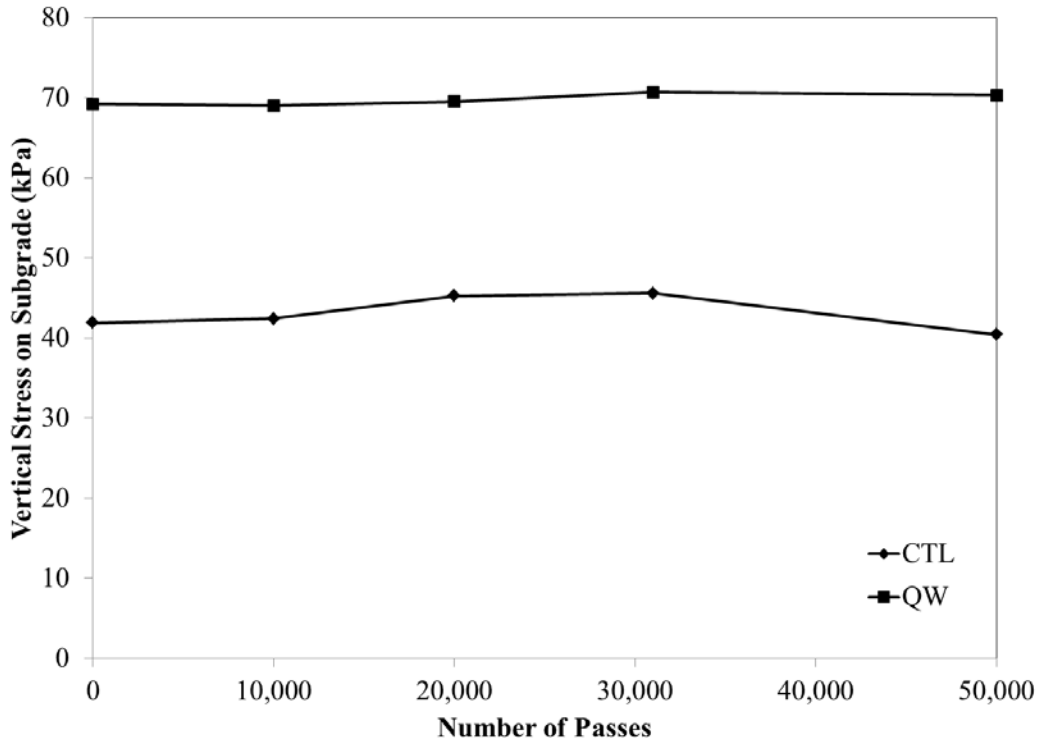


Figure 5.7: Vertical Pressure on Subgrade of Middle Pit in Overlay Experiment

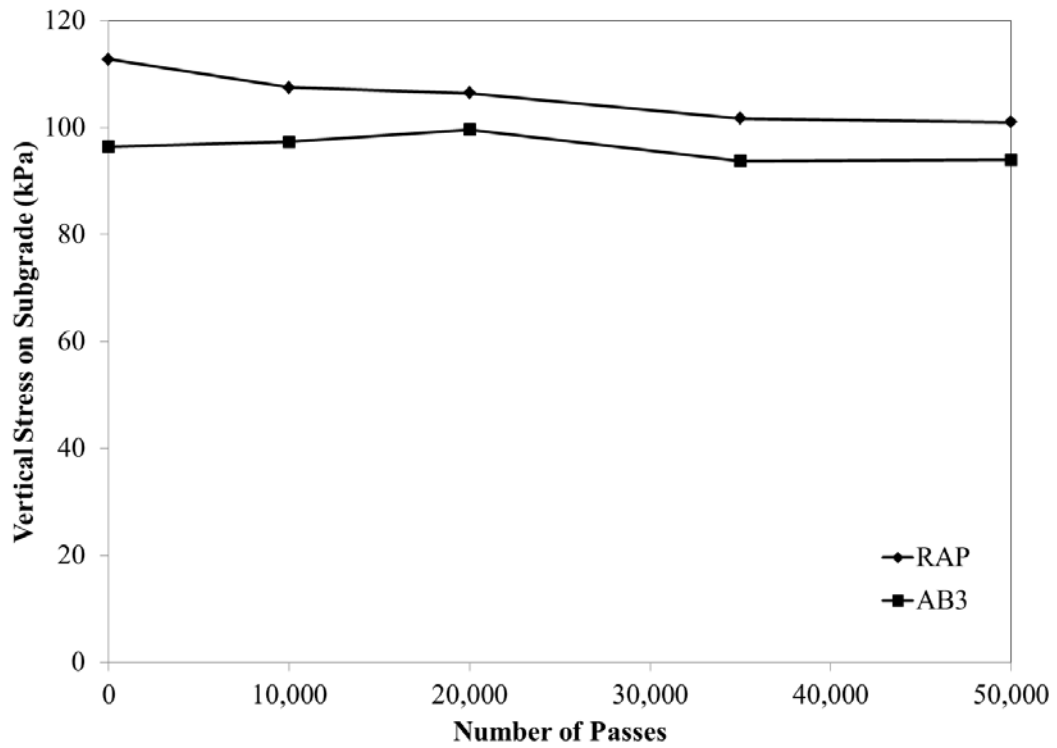


Figure 5.8: Vertical Pressure on Subgrade of South Pit in Overlay Experiment

The strain results showed that the RAP lane still had higher compressive strain than the AB-3 lane as shown in Table 5.2. The strain in the geocells decreased after the overlay as exhibited by the tensile strain in the AB-3 lane reducing from 2,462 microstrain in the first experiment to 1,812 microstrain after overlay. The thicker HMA section helped in reduction of strain in the body of the geocells.

Table 5.2: Peak Horizontal Strain on Geocell after Overlay (Positive = Tension)

a. South Pit (RAP Lane)

	South Pit				
	N				
Cycle	1	2	3	4	5
0	-0.000837				
20K	-0.000505				
50K					

b. South Pit (AB3 Lane)

	South Pit				
	S				
Cycle	1	2	3	4	5
0	-0.000442	0.001812			
20K	-0.000338	0.001760			
50K	-0.000897	0.002462			

5.1.3 Second Experiment

The subgrade protection provided by the thicker cross sections in the second test led to a longer pavement life and lower rut depth, as shown in Figure 5.9 and Figure 5.10. The vertical stress on the subgrade was well below the unconfined compressive strength of the subgrade soil. Figure 5.11 and Figure 5.12 show that as the test progressed, vertical pressure increased; however, this started happening well after the initial test termination point of 500,000 passes. All test sections appeared to be starting to fail at that point. The measured rut depths lent support to

this, as the rut depths were starting to increase rapidly. Again, this only happened after 500,000 passes.

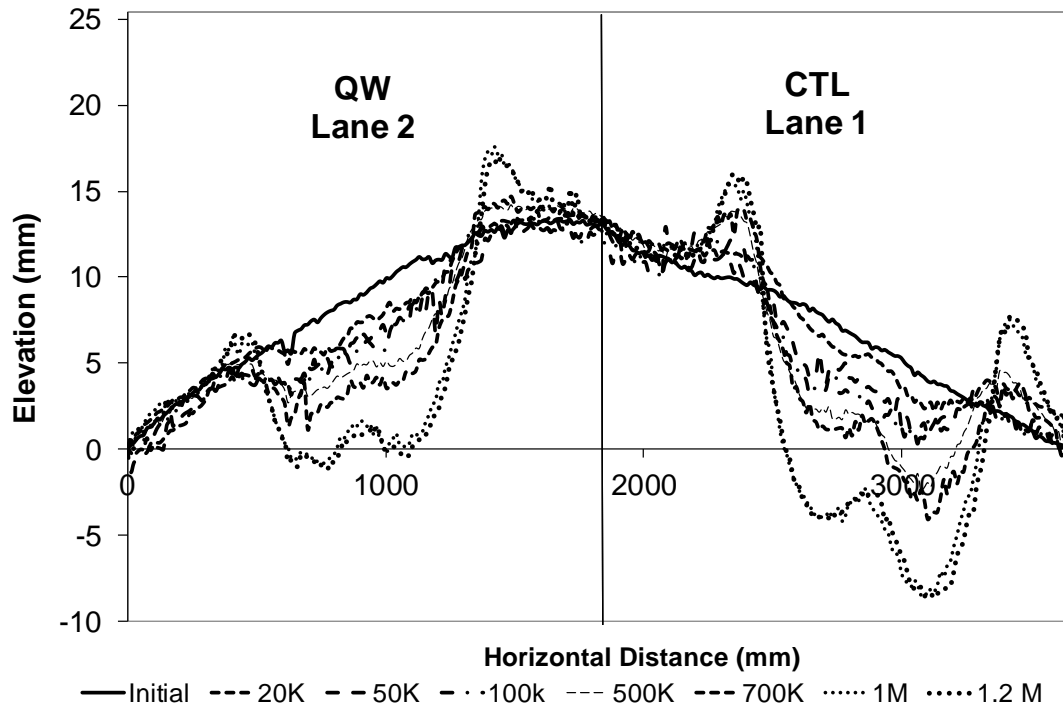


Figure 5.9: Middle Pit Profiles in Second Experiment

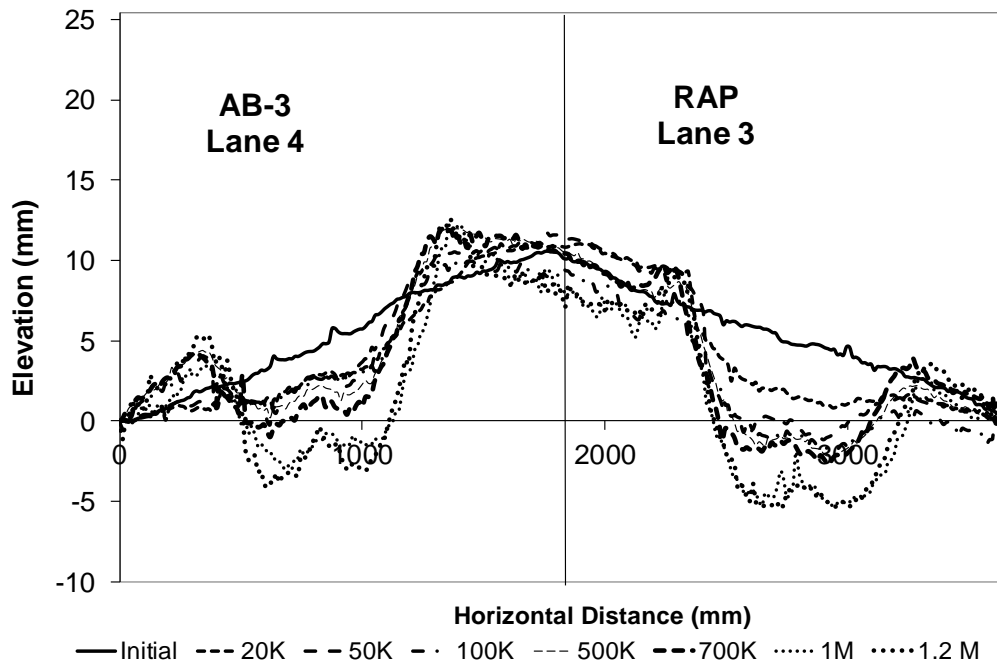


Figure 5.10: South Pit Profiles Second Experiment

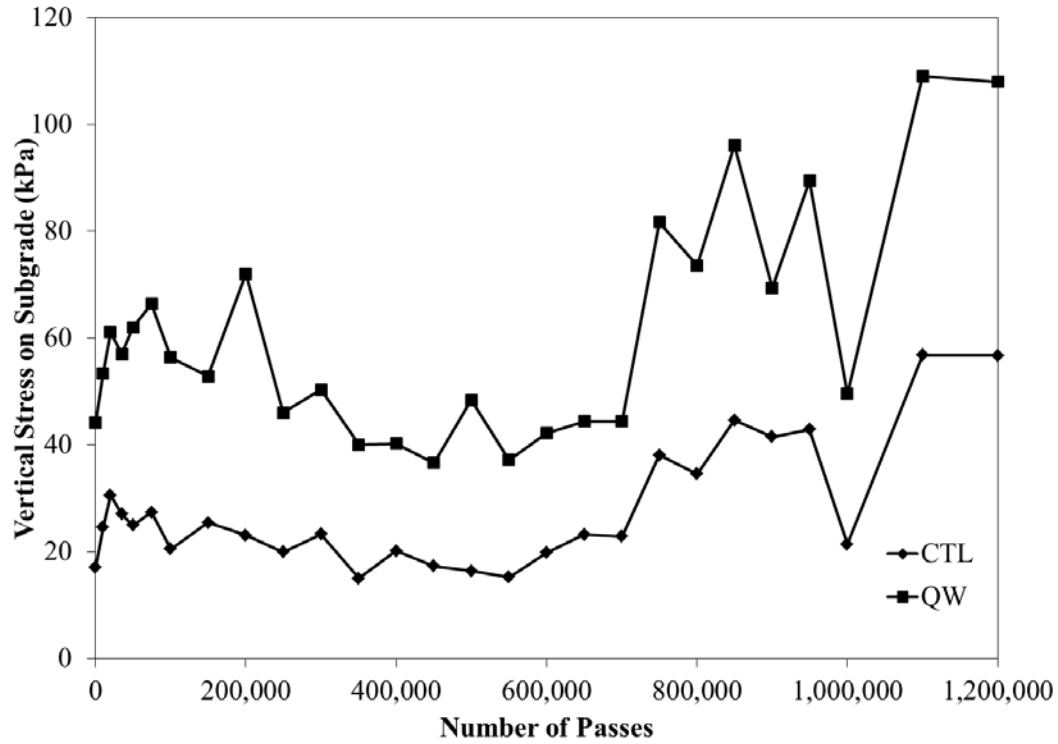


Figure 5.11: Vertical Pressure on Subgrade of Middle Pit in Second Experiment

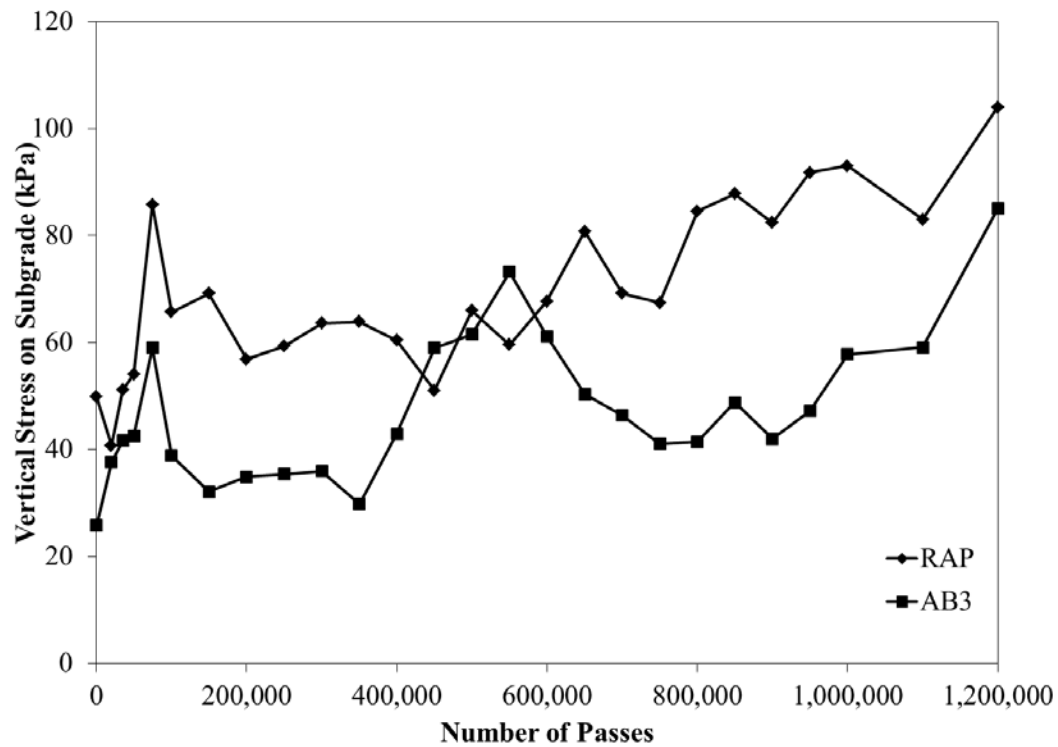


Figure 5.12: Vertical Pressure on Subgrade of South Pit in Second Experiment

The geocell strain gages showed the RAP lane had higher tensile and compressive strains (maximum of 772 microstrain and minimum of -512 microstrain) than the QW (maximum of 477 microstrain and minimum of -254 microstrain) and AB-3 (maximum of 440 microstrain and minimum of -195 microstrain) lanes as shown in Table 5.3. However, all these strain levels are smaller than the first and overlay experiments.

Table 5.3: Geocell Peak Horizontal Strain Second Experiment (Positive = Tension)
a. Middle Pit (QW lane)

Cycle	Middle Pit				
	S				
	1	2	3	4	5
0	0.000263	0.000365	0.000459	-0.000254	-0.000140
20K	0.000260	0.000373	0.000370	-0.000193	-0.000060
50K	0.000210	0.000288	0.000297	-0.000134	-0.000041
100K	0.000230	0.000233	0.000167	-0.000101	-0.000032
500K	0.000230	0.000343	0.000256	-0.000088	0.000035
1,200K	0.000198	0.000477		-0.000250	

b. South Pit (RAP lane)

Cycle	South Pit				
	N				
	1	2	3	4	5
0	-0.000175	-0.000512	0.000772	0.000649	
20K	-0.000062	-0.000218	0.000314	0.000369	
50K	-0.000505	-0.000512	0.000772	0.000649	
100K	-0.000066	-0.000256	0.000309	0.000299	
500K	-0.000065	-0.000252	0.000318	0.000267	
1,200K	-0.000034	-0.000271	0.000284	0.000181	

c. South Pit (AB3 Lane)

Cycle	South Pit				
	S				
	1	2	3	4	5
0	0.000401	0.000440	0.000172		
20K	0.000393	0.000268	0.000172		
50K	0.000401	0.000176	0.000172		
100K	0.000436	0.000291	0.000153		
500K	0.000357	0.000300			
1,200K	0.000400	0.000431			

After the second test was completed, a post-mortem examination of the test sections was done. The geocells changed from their sinusoidal shapes to diamond shapes as shown in Figure 5.13 and Figure 5.14. However, the damage to the geocells seen in the pictures was caused by a pick used to chip through the base layer. The geocell reinforced AB-3 base layer was very compact and was able to hold its shape after extruding the geocells from the base layer, as shown in Figure 5.15. QW showed similar compacted shape retention. During coring of the HMA in the RAP lane, it was noticed up to 50 mm (2 inches) of RAP was bonded to the HMA layer. Highly compacted base materials seemed to behave like a slab instead of individual cells.



Figure 5.13: RAP Post Mortem of 2nd Test



Figure 5.14: AB-3 Post Mortem after 2nd Test



Figure 5.15: AB-3 Material after 2nd Test

5.1.4 Comparison of First and Second Experiment

Rut depths from these experiments are compared in Figure 5.16 and Figure 5.17. Thicker cross sections reduced the rut depths, rate of rut depth formation, and applied vertical pressure on the subgrade, as shown in Figure 5.18. Pressure on the subgrade was reduced by 43% for the control lane, 40% for the QW lane, 71% for the RAP lane, and 69% for the AB-3 lane after the first 50,000 passes. The strain in the geocells was reduced similarly as shown in Figure 5.19. The QW, RAP, and AB-3 lanes saw a reduction of 68%, 75%, and 83%, respectively. Thicker sections were stronger and performed better.

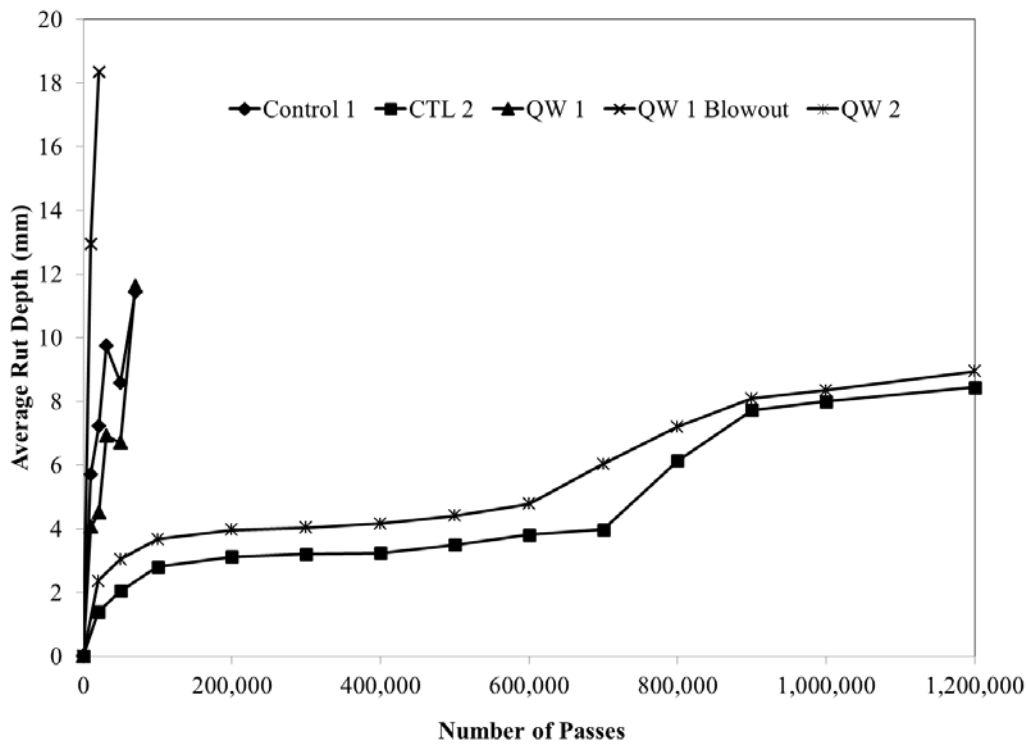


Figure 5.16: Rut Depth Comparison for Middle Pit

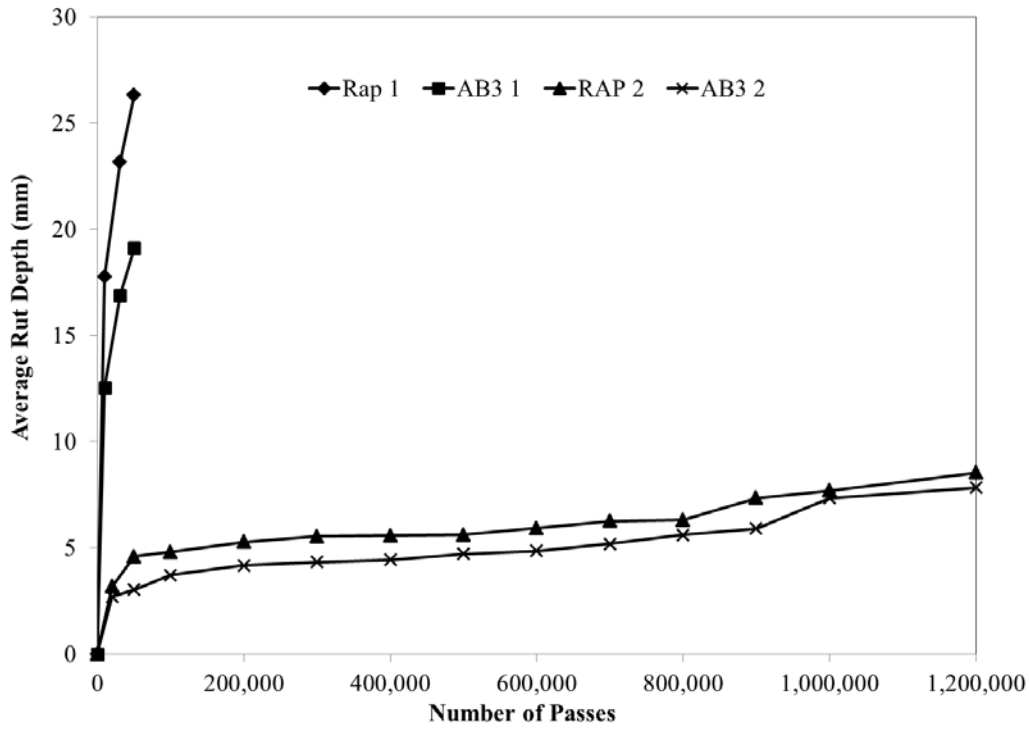


Figure 5.17: Rut Depth Comparison for South Pit

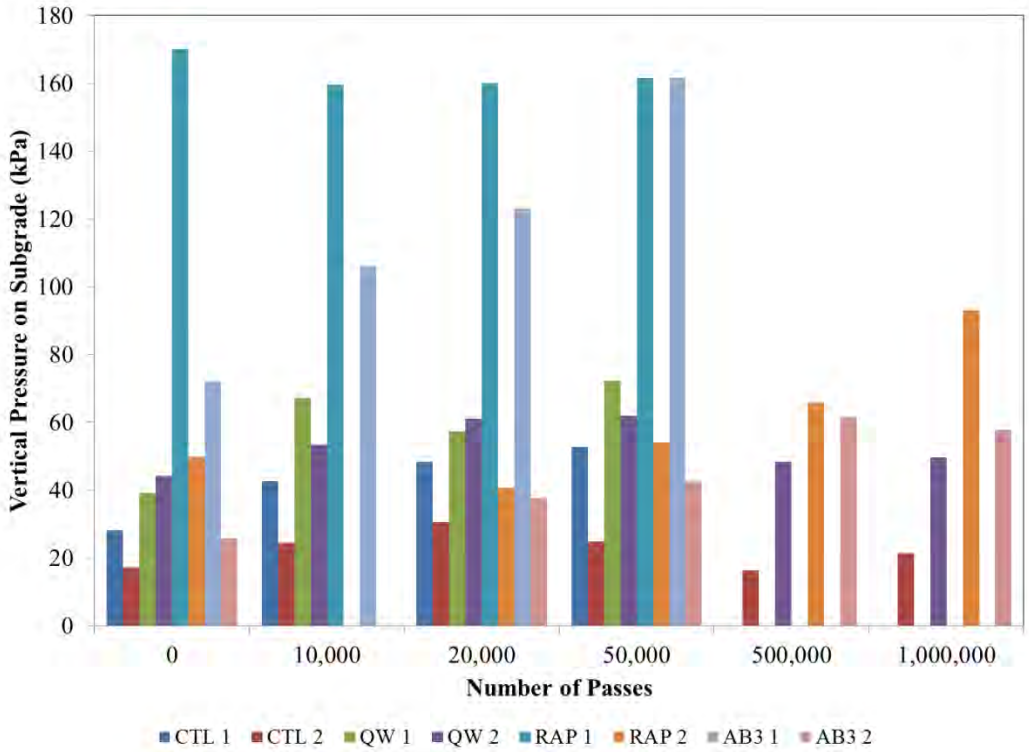


Figure 5.18: Vertical Pressure on Subgrade Comparison

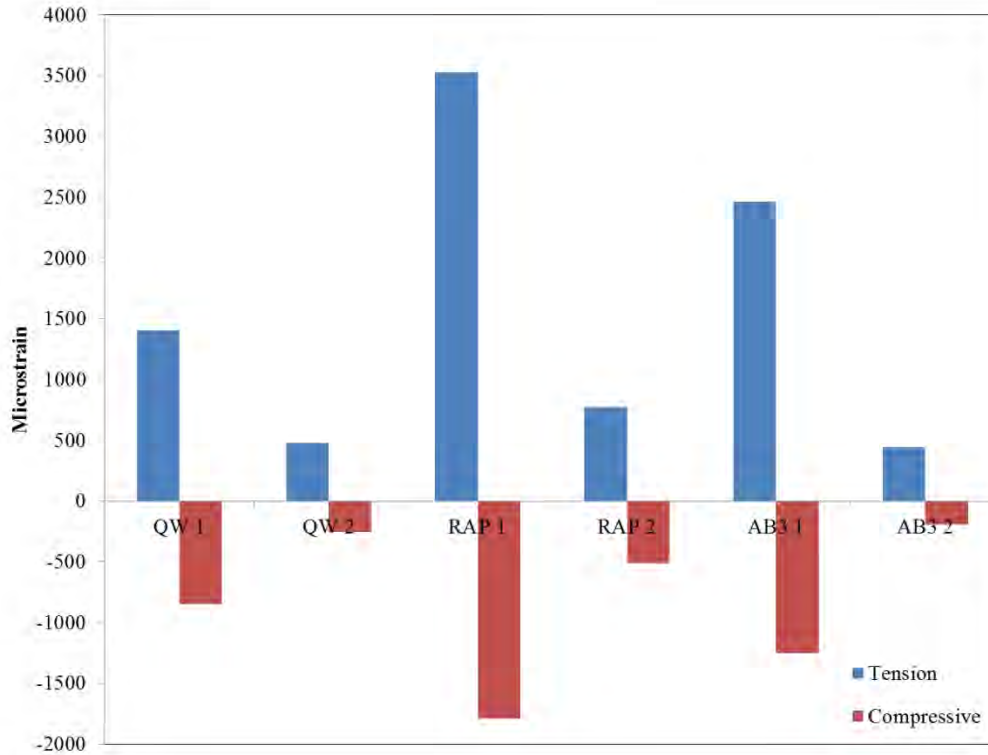


Figure 5.19: Geocell Strain Comparison

5.2 Layered Elastic (KENLAYER) Analysis

KENLAYER is a computer program that solves for the responses of a multilayer, elastic system under a circular loaded area (Huang, 2004). The program can be used to predict deflections, stresses, and strains in different pavement layers under different loading conditions. KENLAYER was used to predict and compare the vertical stress on the subgrade and the strain at the bottom of the HMA layer. Backcalculation using FWD data was used to find the moduli of the layers in the test sections. However, KENLAYER does not have the capability to account for 3-D reinforcing elements such as geocells. Predicted responses have been compared with the measured responses for the first set of data as shown in Table 5.4 and Table 5.5.

Two pressure cells were placed in each lane. Individual gage readings for each lane are shown in Table 5.4. KENLAYER predicted higher vertical stress on the subgrade in the first test than in the second test. The vertical stress on subgrade for the RAP lane was underestimated the most with an average of 57% underestimation in the first test, and 23% in the second test. Sensor 3 on the QW section was directly below the eventually heaved area on the lane. That sensor

showed much higher pressure than its companion gage in the same lane, hinting at overstressing of subgrade and a possible failure. Differences in individual gage readings can be attributed to the differences in initial compaction of the base layers inducing variable loading on the pressure cells.

Strain gages were placed beneath the HMA layer. KENLAYER predicts the principal strains at the desired locations. Again, KENLAYER predicted higher strains in the first test than in the second test. The QW lane strain gage showed 6,330 microstrains indicating the HMA layer was failing rather quickly. In the second test, KENLAYER predicted strain values that were rather closer to the measured values with all predicted values being within 25% of the measured values.

Table 5.4: KENLAYER Vertical Pressure Results (6.89 kPa = 1 psi)

	Control Lane 1		QW Lane 2		RAP Lane 3		AB3 Lane 4	
	Pressure on Subgrade		Pressure on Subgrade		Pressure on Subgrade		Pressure on Subgrade	
First Test								
KENLAYER (kPa)	58.3		121.7		130.5		132.0	
Sensor	1	2	3	4	1	2	3	4
MEASURED (kPa)	29.5	54.1	130.0	56.6	186.1	222.6	92.5	157.4
% Difference	49.5%	7.3%	-6.8%	53.5%	-42.6%	-70.6%	29.9%	-19.2%
Second Test								
KENLAYER (kPa)	39.9		43.2		52.2		54.1	
Sensor	1	2	3	4	1	2	3	4
MEASURED (kPa)	32.2	22.9	52.8	54.4	46.4	81.3	40.6	38.0
% Difference	19.3%	42.5%	-22.1%	-25.8%	11.0%	-56.0%	25.0%	29.8%

Table 5.5: KENLAYER HMA Strain

	Control	QW	RAP	AB3
	Strain (Below HMA)	Strain (Below HMA)	Strain (Below HMA)	Strain (Below HMA)
First Test				
KENLAYER	-0.0003631	-0.0008571	-0.0009215	-0.0009024
MEASURED	-0.000369	-0.00633	-0.000429	-0.000273
% Difference	-1.6%	-638.5%	53.5%	69.85%
Second Test				
KENLAYER	-0.0001626	-0.0001897	-0.0002456	-0.0002535
MEASURED	-0.00014	-0.000146	-0.000209	-0.00022
% Difference	13.9%	23.0%	14.9%	13.2%

5.3 Numerical Analysis Results

5.3.1 Numerical Response Analysis Comparison

5.3.1.1 Stress and Strain Numerical Analysis

The results for different simulations are shown in Table 5.6. During the analysis, the strain on the geocell was analyzed at two different locations. A path was set along five geocells where the strain gages were located, as shown in Figure 5.20. The maximum and minimum strain values along the path were obtained. Next, the maximum and minimum strain values on the entire geocell part were obtained.

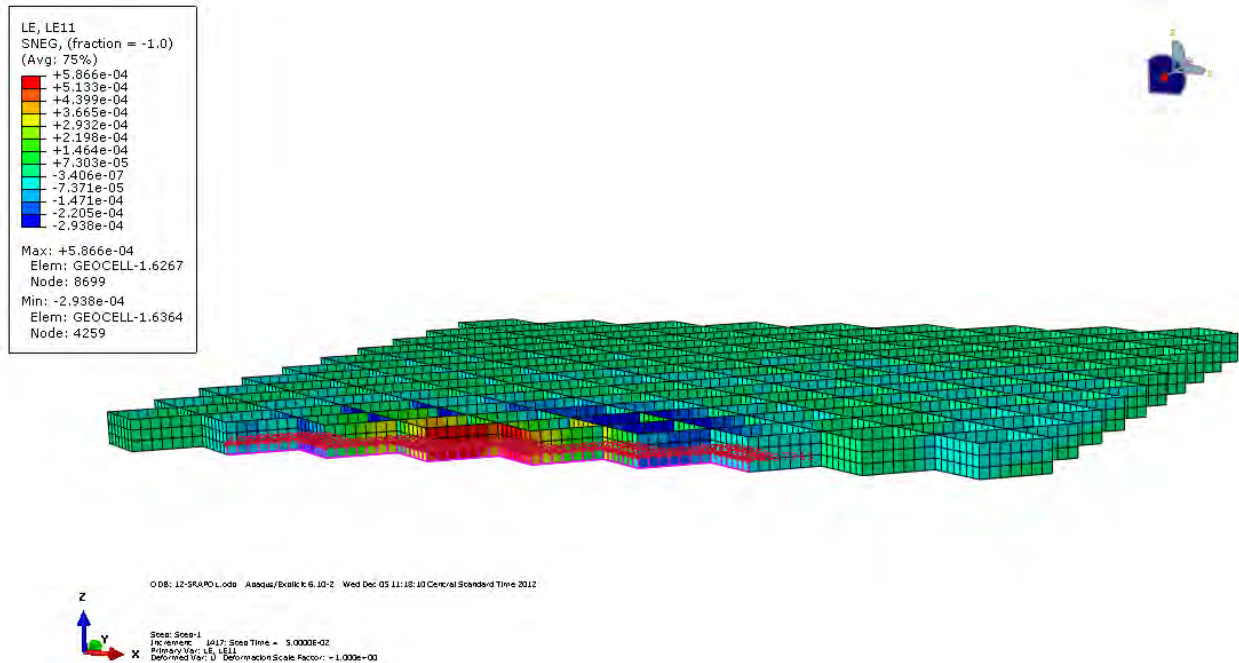


Figure 5.20: Geocell Path

The results followed the intuition that the thicker and stronger sections were, the less stress would be applied to the subgrade, and lower strain would result in the geocell and HMA layers. Table 5.7 compares the numerical analysis results with the measured results. The control lane model resulted in the closest results with the highest difference among all three experiments being 11%. However, it was noticed that numerical analysis tended to over predict the HMA strain.

Table 5.6: Numerical Response Analysis Results

Lane	Test #	HMA Strain	GC Path Strain Max	GC Path Strain Min	GC Max Strain	GC Min Strain	Subgrade Stress
		Microstrain					
CTL	1	414					92
CTL	OL	250					72
CTL	2	148					28
QW	1	496	803	-271	817	-450	90
QW	OL	328	493	-157	494	-264	70
QW	2	159	313	-57	393	-140	43
RAP	1	651	911	-313	930	-511	119
RAP	OL	441	560	-187	587	-293	91
RAP	2	162	220	-63	328	-180	40
AB3	1	641	870	-299	883	-500	124
AB3	OL	433	531	-182	564	-297	95
AB3	2	186	334	-82	407	-194	41

Table 5.7: HMA Strain Comparison

	Control	QW	RAP	AB3
	Microstrain (Below HMA)	Microstrain (Below HMA)	Microstrain (Below HMA)	Microstrain (Below HMA)
First Test				
Numerical Analysis	414	496	651	641
MEASURED	369	6330	429	273
% Difference	10.87%	-1176.21%	34.10%	57.41%
Overlay Test				
Numerical Analysis	250	328	441	433
MEASURED	240	x	421	x
% Difference	4.00%	x	4.54%	x
Second Test				
Numerical Analysis	148	159	162	486
MEASURED	140	146	209	220
% Difference	5.41%	8.18%	-29.01%	54.73%

A comparison of the subgrade stress results from the numerical analysis and the measured values is shown in Table 5.8. Subgrade stress results varied depending on location. This variation can be attributed to the construction of the base layer and initial layer compaction due to loading. AB-3 had unique results with one sensor measuring response that is below the predicted value and a measured response above the predicted one. Numerical analysis under-predicted the subgrade pressure on all RAP sections. Results from the numerical simulations of the second test were closer across the board (with the exception of one RAP sensor) than the results from the simulation of the first test.

Table 5.8: Subgrade Stress Comparison

	Control		QW		RAP		AB3	
	Pressure on Subgrade		Pressure on Subgrade		Pressure on Subgrade		Pressure on Subgrade	
First Test								
Numerical Analysis (kPa)	92.0		90.0		119.0		124.0	
Sensor	1	2	3	4	1	2	3	4
MEASURED (kPa)	29.5	54.1	130.0	56.6	186.1	222.6	92.5	157.4
% Difference	68.0%	41.2%	-44.4%	37.1%	-56.4%	-87.1%	25.4%	-26.9%
Overlay Test								
Numerical Analysis (kPa)	72.0		70.0		91.0		95.0	
Sensor	1	2	3	4	1	2	3	4
MEASURED (kPa)	42.2	41.6	x	47.7	104.3	121.3	87.7	109.1
% Difference	41.4%	42.2%	x	31.9%	-14.6%	-33.3%	7.7%	-14.8%
Second Test								
Numerical Analysis (kPa)	28.0		43.0		40.0		41.0	
Sensor	1	2	3	4	1	2	3	4
MEASURED (kPa)	32.2	22.9	52.8	54.4	46.4	81.3	35.2	48.2
% Difference	-14.9%	18.1%	-22.7%	-26.4%	-16.0%	-103.4%	14.2%	-17.5%

Since the numerical simulations were run using Abaqus/Explicit, the HMA layer was modeled as consisting of linear elastic materials. Therefore, rutting results could not be extracted from these numerical simulations.

5.3.1.2 Rut Numerical Analysis

The rut numerical analysis did not predict the quick summation of rut depths seen in the first test. The rut profile shape was similar to the profiles seen during the APT test. Simulated profiles can be seen in the Appendix. The simulations showed a W-shaped profile and the heaving at the edge of the tires as seen in the APT test. Differences could be seen in material properties as seen in Table 5.9. The table shows the height of the heave, the depth of the rut, and the total difference in elevation from heave to rut. The numerical analysis did not show significant rutting in the first 50,000 cycles so each APT test was simulated to 1,000,000 cycles. The second test performed better in all analyses. Unique results came from the overlay simulation. The overlay simulation had deeper rutting than the first test simulation in all of the base materials even though the only difference was a thicker HMA layer.

Table 5.9: Rut Depths

	Cycle	Highest Elevation			Lowest Elevation			Difference in Elevation		
		100,000	500,000	1,000,000	100,000	500,000	1,000,000	100,000	500,000	1,000,000
CTL	1	0.95	1.86	2.49	-1.71	-2.94	-3.78	2.65	4.80	6.27
	OL	0.90	1.79	2.39	-1.95	-3.33	-4.28	2.85	5.11	6.67
	2	1.11	2.03	2.66	-2.03	-3.47	-4.41	3.14	5.50	7.07
QW	1	1.04	2.04	2.73	-2.59	-4.28	-5.40	3.63	6.32	8.13
	OL	1.01	2.02	2.72	-2.79	-4.68	-5.92	3.80	6.70	8.64
	2	1.04	2.00	2.66	-1.96	-3.55	-4.61	3.00	5.55	7.26
RAP	1	1.03	2.04	2.72	-2.68	-4.45	-5.60	3.71	6.49	8.32
	OL	1.01	2.02	2.72	-2.71	-4.67	-5.98	3.73	6.70	8.70
	2	1.01	1.97	2.64	-2.25	-3.89	-4.99	3.25	5.86	7.63
AB3	1	1.03	2.04	2.72	-2.60	-4.34	-5.48	3.63	6.38	8.20
	OL	1.02	2.03	2.73	-2.63	-4.58	-5.87	3.65	6.61	8.60
	2	1.01	1.98	2.64	-2.01	-3.65	-4.76	3.02	5.63	7.40

Table 5.10 shows the comparison between the second APT test and the numerical analysis results. Numerical analysis underestimated the rut depth by at least 130%. However, when the actual rut depth was compared to the difference between the bottom of the rut and the top of the heave obtained from the numerical analysis, the results were very similar, with the south pit being within 1%.

Table 5.10: Rut Depth Comparison at One Million Cycles

	Control	QW	RAP	AB3
	Rut Depth (mm)	Rut Depth (mm)	Rut Depth (mm)	Rut Depth (mm)
Second Test				
Numerical Analysis Rut Depth	3.14	3.00	3.25	3.02
MEASURED	9.12	12.04	7.69	7.34
% Difference	-190.45%	-301.33%	-136.62%	-143.05%
Second Test				
Numerical Analysis Rut Depth + Heave	7.07	7.26	7.63	7.40
MEASURED	9.12	12.04	7.69	7.34
% Difference	-29.00%	-65.84%	-0.79%	0.81%

5.3.2 Parametric Studies of Numerical Simulation

To investigate the effects of the modulus of the base material and the height of geocells, a parametric study was performed using the finite element model. The variables were limited to the base layer. The modulus of the base material gives an insight into the quality of base material and compaction level in the geocells. Analysis used a range of base material elastic modulus starting from 25 MPa (3,626 psi) to 500 MPa (72,519 psi). The results have been shown in Figure 5.21.

Stronger base material showed a decrease of stress on the subgrade layer up to a point and then continued to level off. The strain on the geocells increased as the base material modulus increased up to 200 MPa (29,008 psi) and then decreased. Infill material placed in the geocell has a significant effect on the effectiveness of geocell; however, the increase in modulus of base material becomes less significant.

In the geocell height study, ratios of geocell height, h_{GC} , and two HMA thicknesses (150 mm [6 inches] and 100 mm [4 inches]), h_{HMA} , were investigated. In the APT test sections, a 50-mm (2-inch) cover was determined to be the minimum cover for constructability. During the study, the height of the base layer was maintained at 50 mm (2 inches) over the height of the geocell. Other parameters in the model were held constant, as shown in Table 5.11.

In the height study, vertical stress on the subgrade decreased or remained the same as the ratio of the geocell height to the thickness of HMA increased from less than 1 to 2. In both cases, the vertical stress on the subgrade increased as the ratio was greater than 2 and then decreased significantly, as shown in Figure 5.22. Strain in the geocells decreased as the ratio increased. There was a decrease in the benefit of reduced strain as the ratio exceeded 2, as shown in Figure 5.23.

Table 5.11: Parametric Study Material Properties

	Study	Base Modulus	Geocell Height
Subgrade	Density (tonne/mm ³)	1.52E-06	1.52E-06
	E (MPa)	45	45
	v	0.45	0.45
	Friction Angle	0	0
	Dilation Angle	0	0
	h (mm)	1274	1274
	Cohesion (Mpa)	0.104	0.104
Base	Density (tonne/mm ³)	2.03E-06	2.03E-06
	E (MPa)	Variable	150
	v	0.4	0.4
	Friction Angle	47.2	47.2
	Dilation Angle	17.2	17.2
	h (mm)	150	Geocell height + 50mm
	Cohesion (Mpa)	0.0047	0.0047
Geocell	E (MPa)	550	550
	v	0.45	0.45
	h (mm)	100	Variable
HMA	Density (tonne/mm ³)	2.26E-06	2.26E-06
	E (MPa)	4000	4000
	v	0.3	0.3
	h (mm)	100	100 or 150

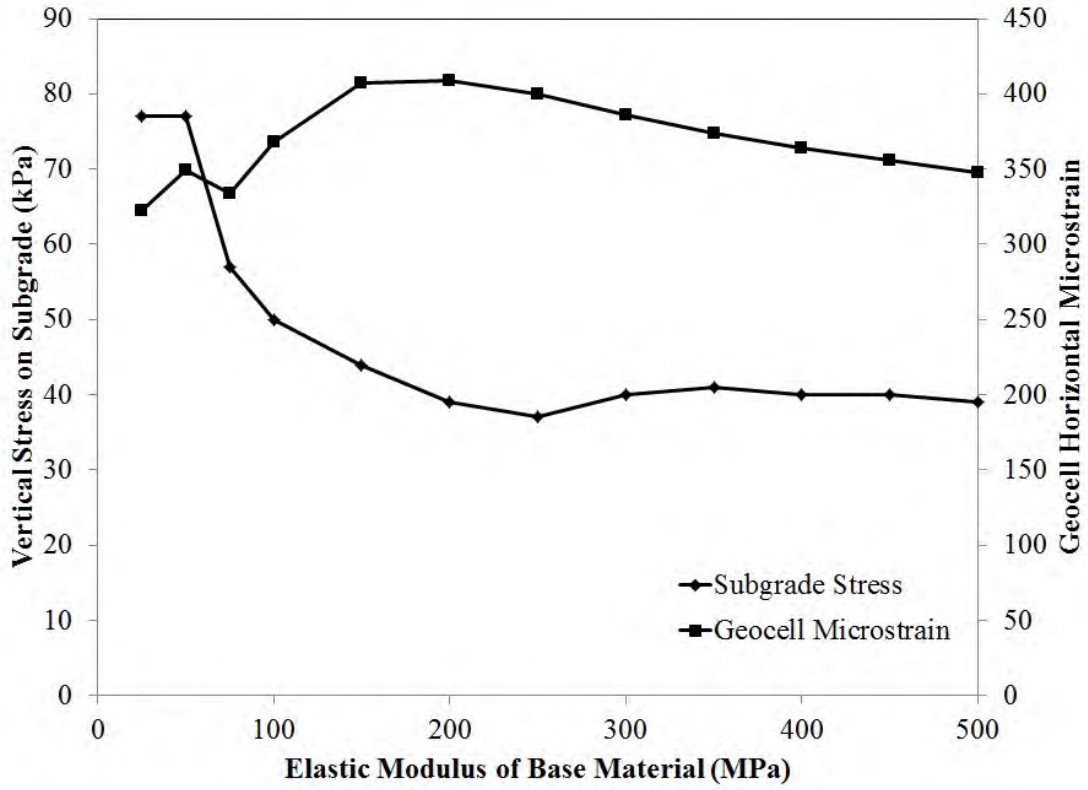


Figure 5.21: Response Results for Varying Base Material Elastic Modulus

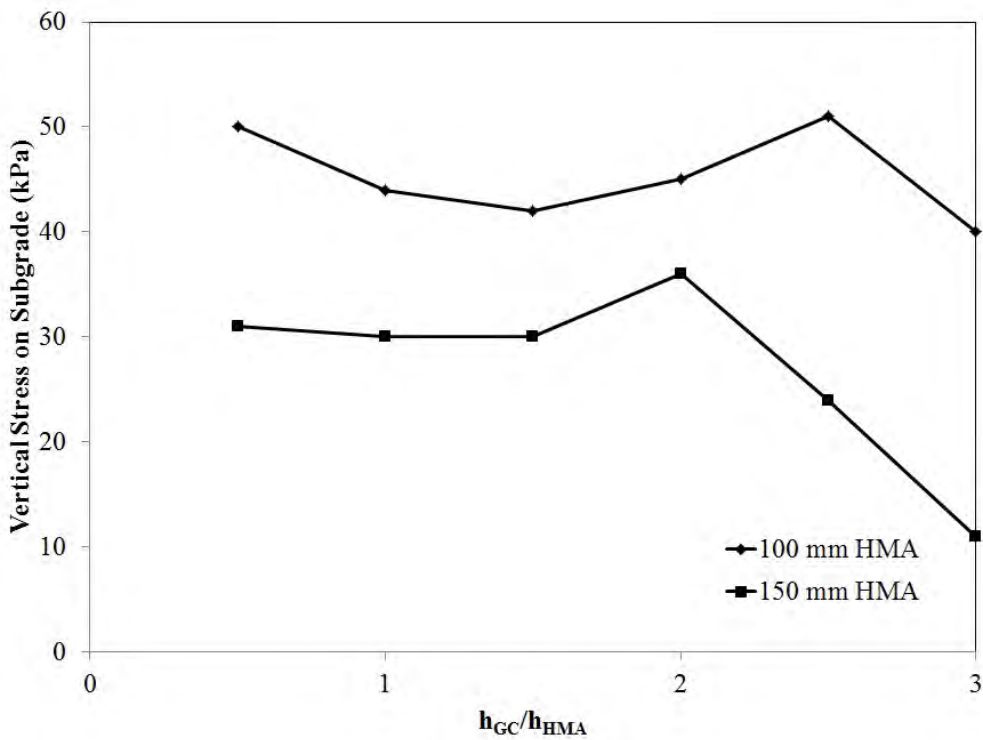


Figure 5.22: Subgrade Stress with Varying Geocell Height

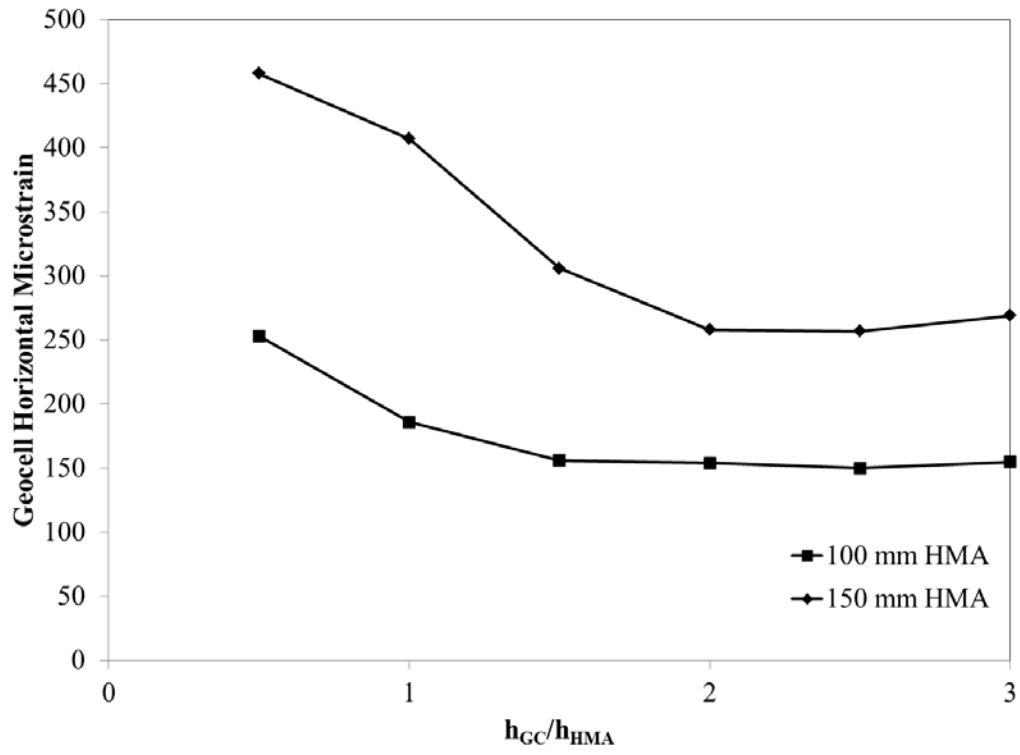


Figure 5.23: Geocell Horizontal Strain with Varying Geocell Height

Chapter 6: Conclusions and Recommendations

In this study, accelerated pavement testing was completed on geocell-reinforced base layers overlaid with HMA. Rut depths, stresses in the subgrade, and strain in the geocells and HMA layers were recorded to study behavior of different infill materials. The experimental data was used to validate numerical models developed based on the geocell-reinforced pavement sections. Parametric simulations were conducted to evaluate different variables in the study.

Based on this study, the following conclusions and recommendations can be made for the geocell-reinforced base layers for low-volume paved roads:

1. Under HMA and after initial compaction due to loading, the base materials become solidified and begin to behave like a slab instead of individual cells.
2. A 50-mm cover over the geocells ensures a better compaction of infill materials in the geocells, and provides protection to the geocells during compaction and HMA placement.
3. A 75-mm thick geocell reinforced base layer approaches the maximum capacity of the geocells. A 100-mm thick geocell enhances the load-bearing capacity of the base layer. Taller geocells provide more friction to overcome, increasing the bearing capacity. However, the numerical analysis showed an increase in the vertical subgrade stress when the ratio of the height of the geocell to the height of the HMA layer approached 2.
4. Lower quality infill materials can perform just as well as high-quality infill material. Geocells enhance lower quality materials to allow them to be used. Increase in the quality of the base material increased the overall structural stability of the system. However, the benefit diminishes with increasing base modulus.
5. A HMA layer of 50 mm is too thin for the existing legal axle load. The minimum thickness for the HMA layer is recommended to be 100 mm.

References

- AASHTO T 324 (2004). *Standard method of test for Hamburg wheel-track testing of compacted hot-mix-asphalt (HMA)*. Washington, DC: American Association of State Highway and Transportation Officials.
- AASHTO TP 79 (2011). *Standard method of test for determining the dynamic modulus and flow number for hot mix asphalt (HMA) using the asphalt mixture performance tester (AMPT)*. Washington, DC: American Association of State and Highway Transportation Officials.
- Aschenbrener, T., Terrel, R. L., & Zamora, R. A. (1994). *Comparison of the Hamburg wheel-tracking device and the environmental conditioning system to pavements of known stripping performance*. Report no. CDOT-DTD-R-94-1. Denver, CO: Colorado Department of Transportation.
- ASTM D 4439-04 (2004). *Standard terminology for Geosynthetics*. West Conshohocken, PA: ASTM International.
- Bathurst, R. J., & Jarrett, P. M. (1988). Large-scale model tests of geocomposite mattresses over peat subgrades. *Transportation Research Record 1188*, 28-36. Washington, DC: Transportation Research Board.
- Brown, E. R., Kandhal, P. S., Roberts, F. L., Kim, Y. R., Lee, D. Y., & Kennedy, T. W. (2009). *Hot mix asphalt materials, mixture design and construction* (3rd ed.). Lanham, MD: NAPA Research and Education Foundation.
- Button, J. W., Chowdhury, A., & Bhasin, A. (2004). *Design of TxDOT asphalt mixtures using the Superpave gyratory compactor*. Report no. FHWA/TX-05/0-4203-1. Austin, TX: Texas Department of Transportation.
- Dash, S. K., Krishnaswamy, N. R., & Rajagopal, K. (2001). Bearing capacity of strip footings supported on geocell-reinforced sand. *Geotextiles and Geomembranes 19*(4), 235-256.
- Dash, S. K., Rajagopal, K., & Krishnaswamy, N. R. (2001). Strip footing on geocell reinforced sand beds with additional planar reinforcement. *Geotextiles and Geomembranes 19*(8), 529-538.
- Dash, S. K., Rajagopal, K., & Krishnaswamy, N. R. (2004). Performance of different geosynthetic reinforcement materials in sand foundations. *Geosynthetics International 11*(1), 35-42.

- Dash, S. K., Sireesh, S., & Sitharam, T. G. (2003). Model studies on circular footing supported on geocell reinforced sand underlain by soft clay. *Geotextiles and Geomembranes* 21(4), 197-219.
- Dassault Systèmes. (2011). *ABAQUS user's manual*. Providence, RI: Dassault Systèmes.
- Giroud, J.P. & Han, J. (2004a). Design method for geogrid-reinforced unpaved roads. I. Development of design method. *Journal of Geotechnical and Geoenvironmental Engineering* 130(8), 775-786.
- Giroud, J.P. & Han, J. (2004b). Design method for geogrid-reinforced unpaved roads. II. Calibration and verification. *Journal of Geotechnical and Geoenvironmental Engineering* 130(8), 787-797.
- Han, J., Pokharel, S. K., Yang, X. M., Manandhar, C., Leshchinsky, D., Halahmi, I., & Parsons, R. L. (2011). Performance of geocell-reinforced RAP bases over weak subgrade under full-scale moving wheel loads. *Journal of Materials in Civil Engineering* 23(11), 1525-1534.
- Huang, Y.H. (2004). *Pavement analysis and design* (2nd ed.). Upper Saddle River, NJ: Prentice Hall, Inc.
- Koerner, R. M. (1994). *Designing with geosynthetics* (3rd ed.). Englewood Cliffs, NJ: Regents/Prentice Hall.
- Koerner, R. M. (2005). *Designing with geosynthetics* (5th ed.). Upper Saddle River, NJ: Pearson Prentice Hall.
- Leshchinsky, B. & Ling, H. (2013). Effects of geocell confinement on strength and deformation behavior of gravel. *Journal of Geotechnical and Geoenvironmental Engineering* 139(2), 340-352.
- Missouri Asphalt Pavement Association (MAPA). Asphalt pavement recycling facts. <http://moasphalt.org/facts/environmental/facts.htm> (accessed Sept. 2012).
- NCHRP (2011). *Guide for mechanistic-empirical design of new and rehabilitated pavement structures*. Champaign, IL: Applied Research Associates (ARA), Inc., ERES Consultants Division.
- Pokharel, S. K., Han, J., Leshchinsky, D., Parsons, R. L., & Halahmi, I. (2010). Investigation of factors influencing behavior of single geocell-reinforced bases under static loading. *Geotextiles and Geomembranes* 28(6), 570-578.

- Sitharam, T. G., Sireesh, S., & Dash, S. K. (2005). Model studies of a circular footing supported on geocell-reinforced clay. *Canadian Geotechnical Journal* 42(2), 693-703.
- Texas Department of Transportation (TxDOT). (2008). Frequently asked questions about the falling weight deflectometer (FWD): Technical advisory. Austin, TX: TxDOT. ftp://ftp.dot.state.tx.us/pub/txdot-info/cst/tips/falling_weight_deflectometer.pdf
- Washington State Department of Transportation (WSDOT). (2005). *Everseries© user's guide: Pavement analysis computer software and case studies*. Olympia, WA: WSDOT. <http://www.wsdot.wa.gov/NR/rdonlyres/0C02BB7B-C345-4958-AA08-089E5E512B96/0/EverseriesUserGuidePart1.pdf>
- Witczak, M. W., Kaloush, K., Pellinen, T., El-Basyouny, M., & Von Quintus, H. (2002). *Simple performance test for Superpave mix design*. NCHRP Report 465. Washington, DC: Transportation Research Board.
- Yang, X. (2010). *Numerical analyses of geocell-reinforced granular soils under static repeated loads*. (Doctoral dissertation). University of Kansas, Lawrence.
- Yuu, J., Han, J., Rosen, A., Parsons, R. L., & Leshchinsky, D. (2008). Technical review of geocell-reinforced base courses over weak subgrade. *Geoamericas 2008: Proceedings of the First Pan American Geosynthetics Conference & Exhibition, March 2-5, Cancun, Mexico*. Roseville, MN: Industrial Fabrics Association International (IFAI).

Appendix: Numerical Analysis Profiles

The figures in the appendix show the profile results of the numerical analysis. Each figure shows the simulated rut profiles at 100,000, 500,000, and 1,000,000 cycles. The conversion factor is 25.4 mm to 1 inch.

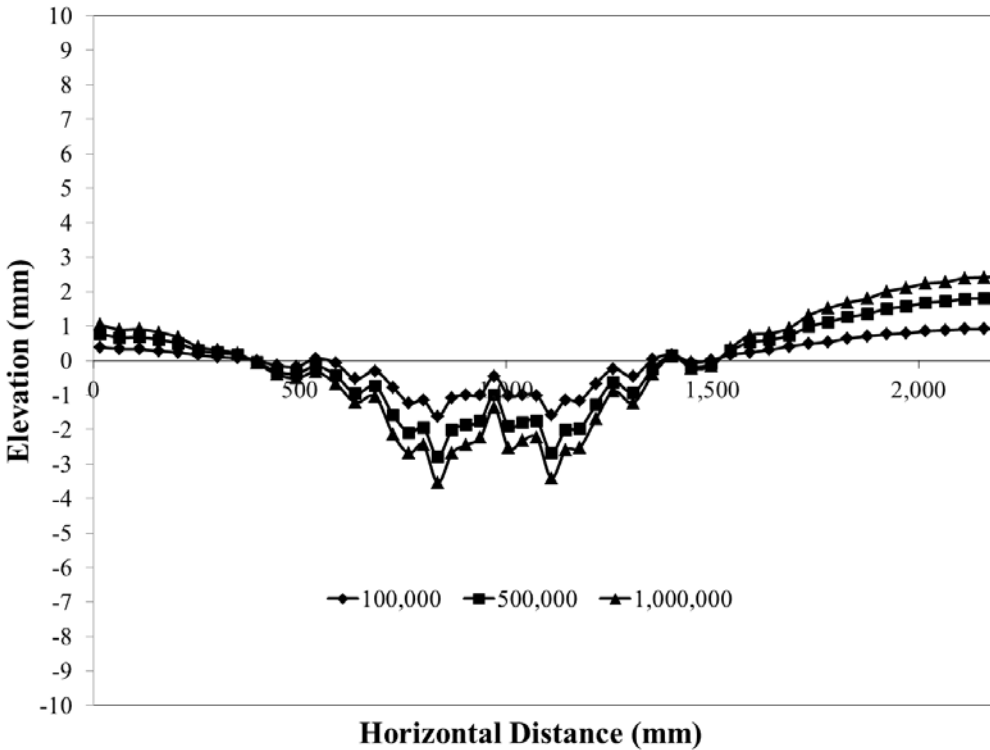


Figure A.1: Simulated Control Rut Profiles for First Test

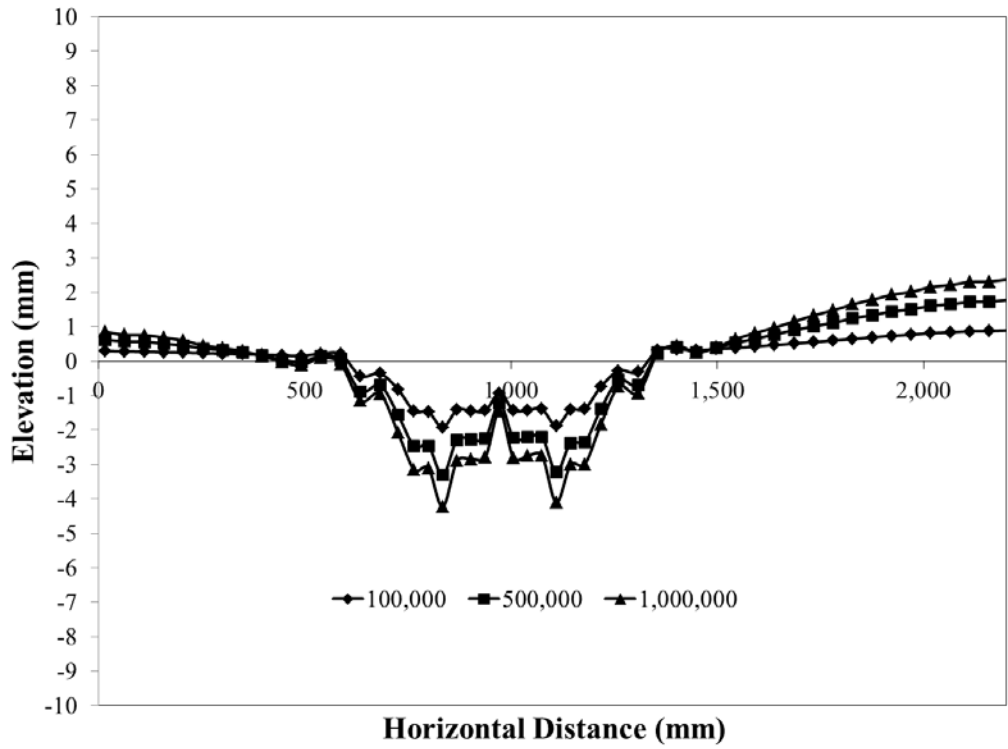


Figure A.2: Simulated Control Rut Profiles for Overlay Test

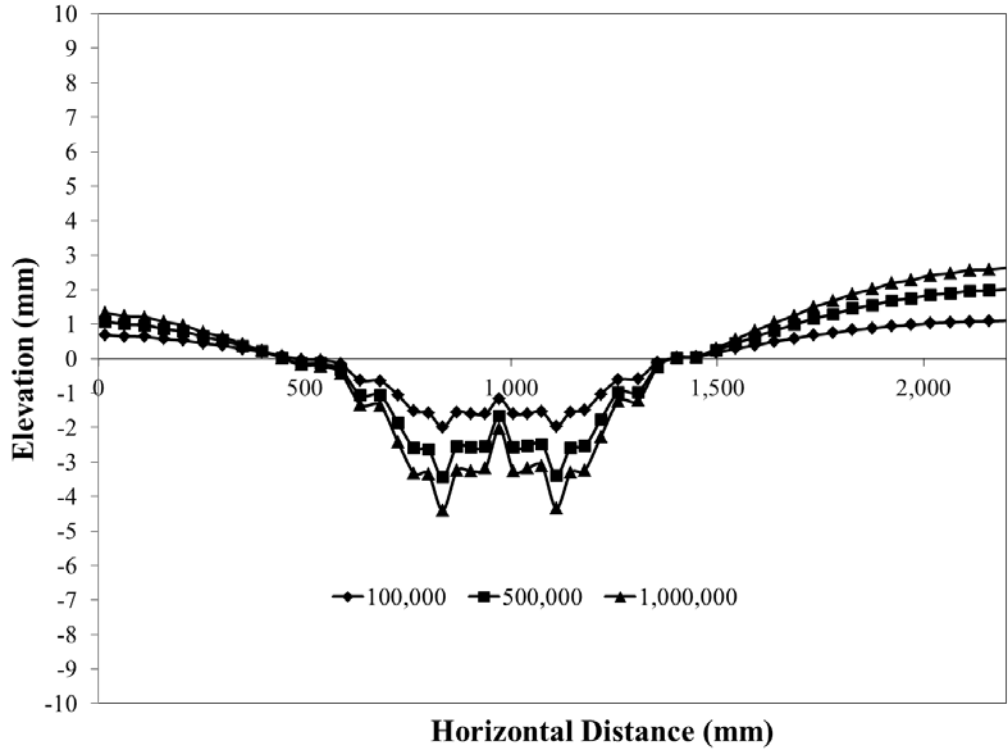


Figure A.3: Simulated Control Rut Profiles for Second Test

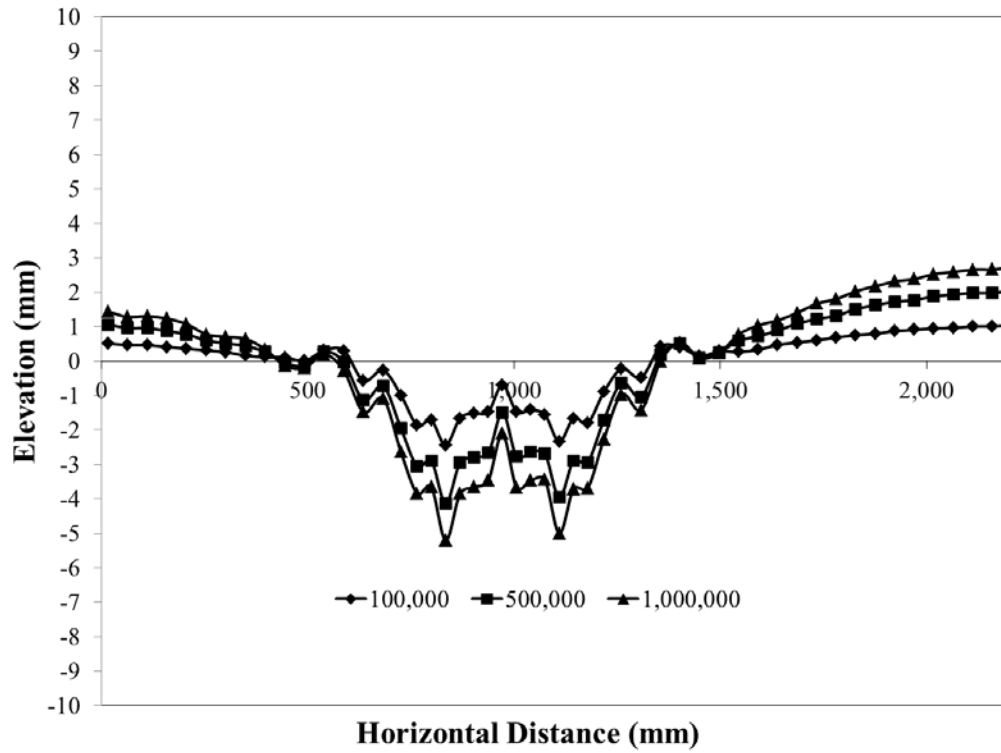


Figure A.4: Simulated Quarry Waste Rut Profiles for First Test

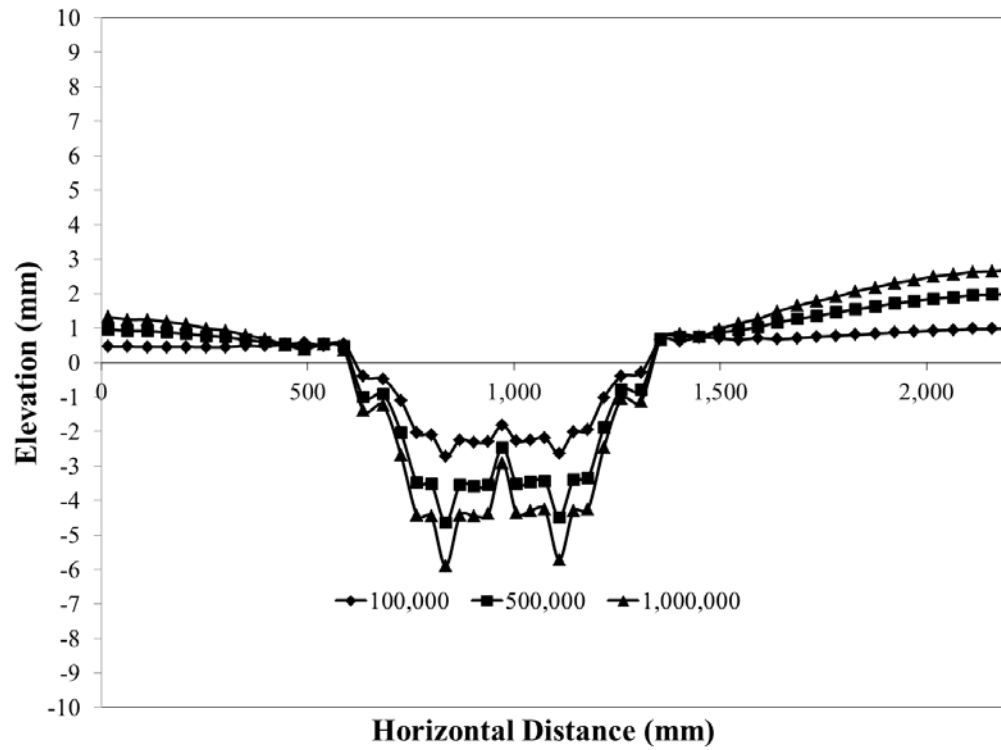


Figure A.5: Simulated Quarry Waste Rut Profiles for Overlay Test

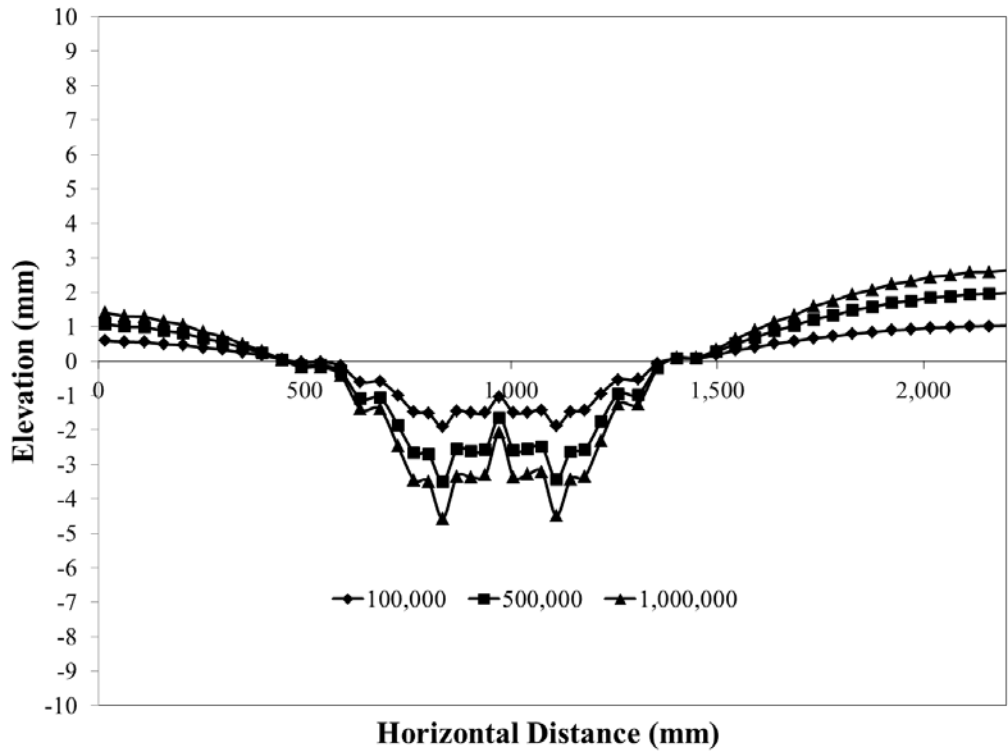


Figure A.6: Simulated Quarry Waste Rut Profiles for Second Test

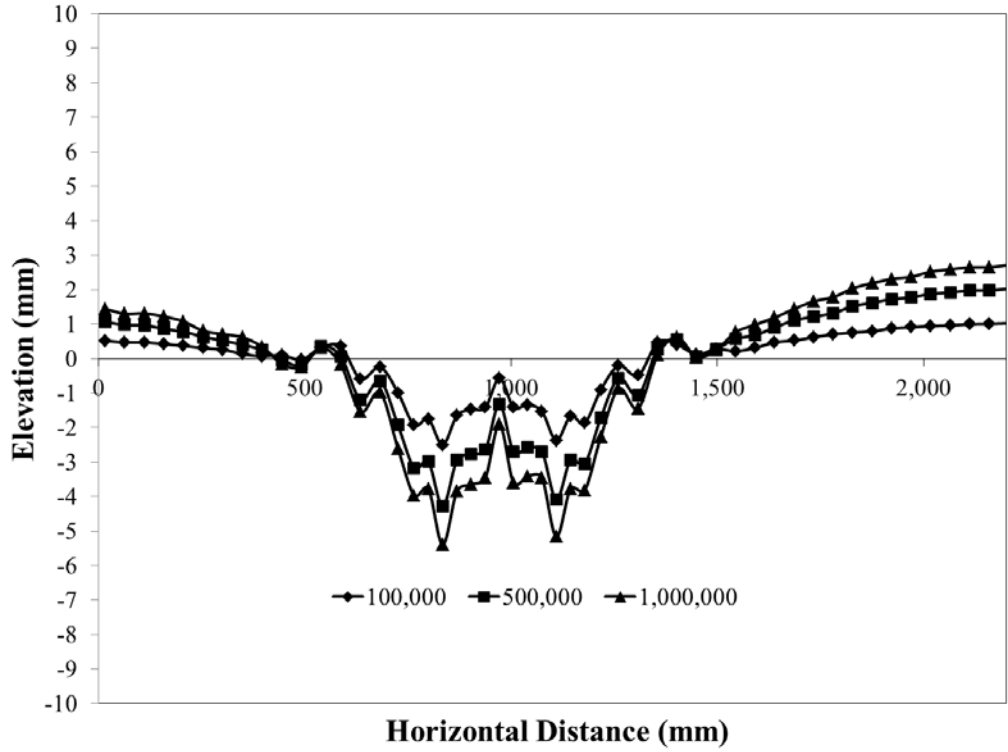


Figure A.7: Simulated RAP Rut Profiles for First Test

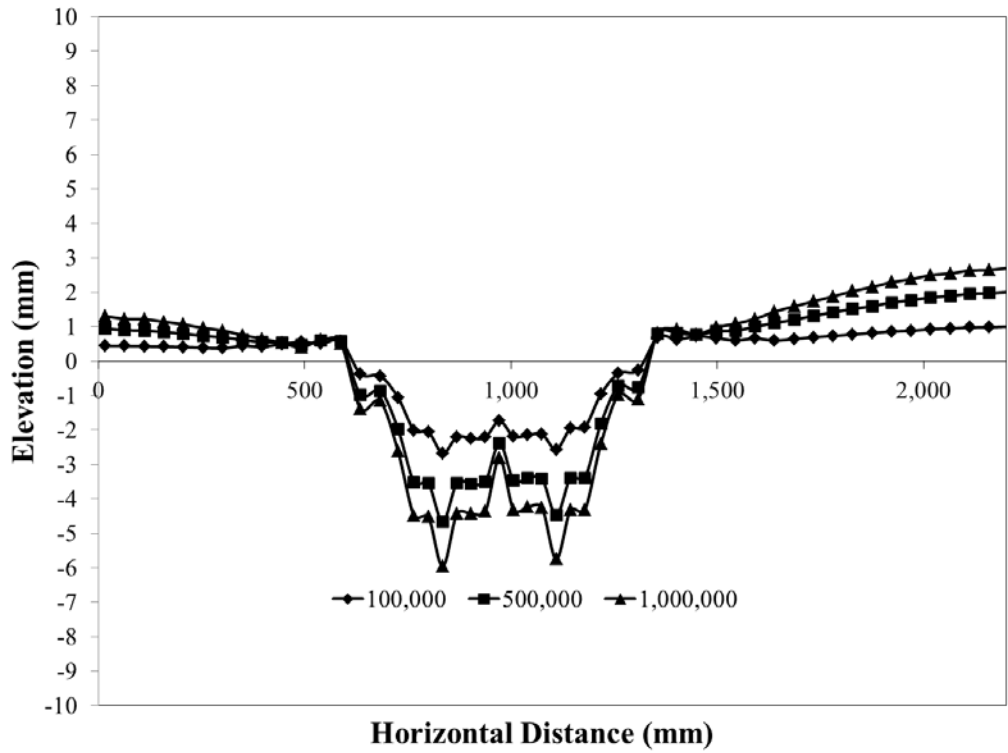


Figure A.8: Simulated RAP Rut Profiles for Overlay Test

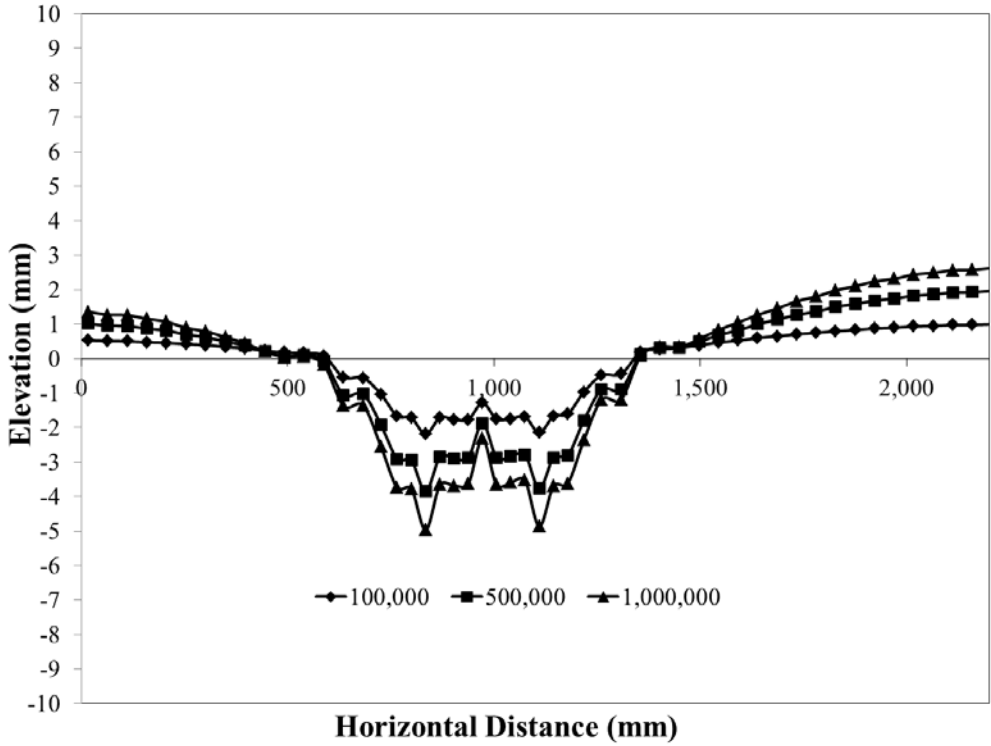


Figure A.9: Simulated RAP Rut Profiles for Second Test

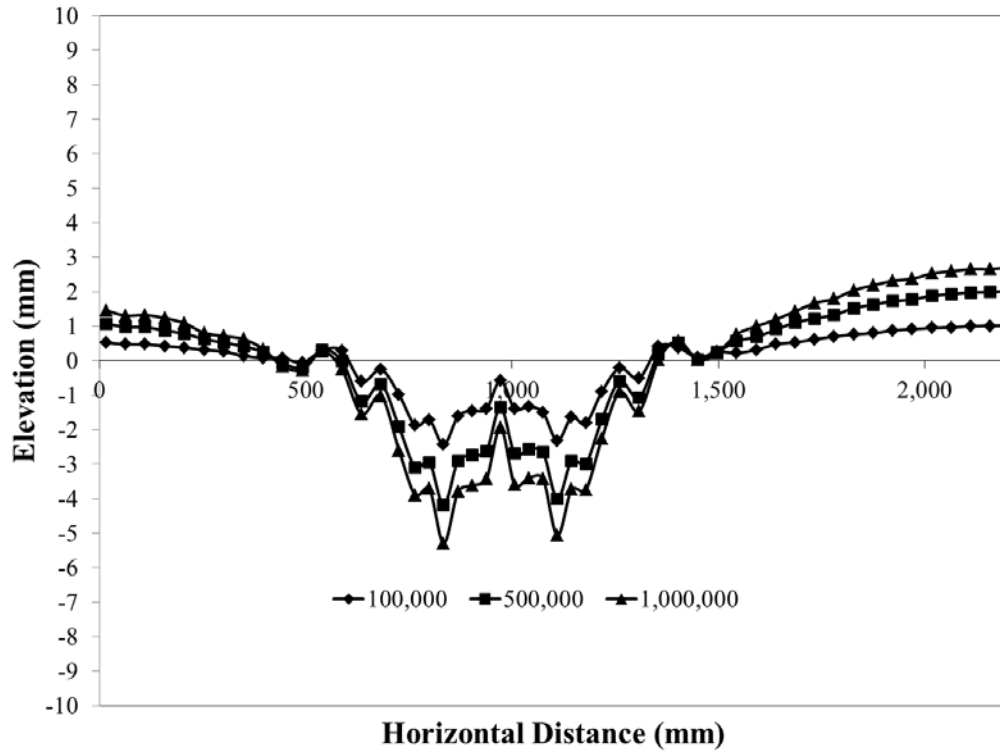


Figure A.10: Simulated AB3 Rut Profiles for First Test

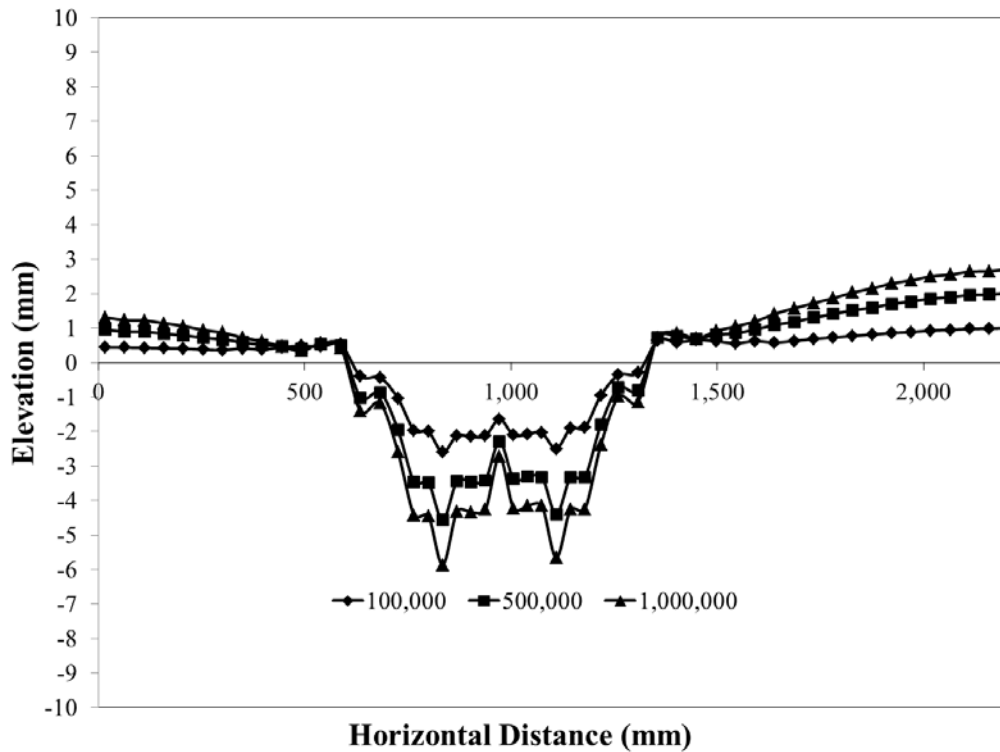


Figure A.11: Simulated AB3 Rut Profiles for Overlay Test

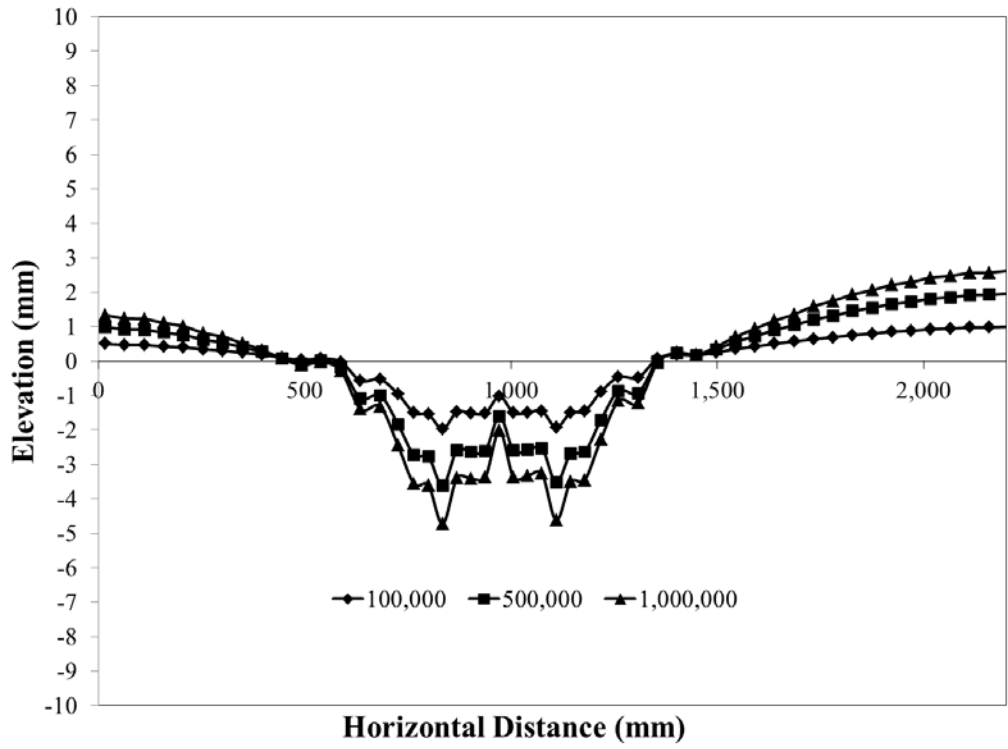


Figure A.12: Simulated AB3 Rut Profiles for Second Test

